

Computational Methods for Gravitational Wave Physics: Spectral Cauchy-Characteristic Extraction and Tidal Splicing

Thesis by
Kevin Barkett

In Partial Fulfillment of the Requirements for the
Degree of
Doctor of Philosophy

The logo for the California Institute of Technology (Caltech), featuring the word "Caltech" in a bold, orange, sans-serif font.

CALIFORNIA INSTITUTE OF TECHNOLOGY
Pasadena, California

2019
Defended December 6, 2018

© 2019

Kevin Barkett

ORCID: 0000-0001-8230-4363

All rights reserved

ACKNOWLEDGEMENTS

An undertaking of this size is not possible without the support and assistance provided by the many wonderful and fantastic people in my life:

To my loving parents, for having my back through all of these long years since I was a wee little lad. After nearly years, I'm finally getting out of school and moving into the real world!

To Mark Scheel and Yanbei Chen for advising me over these many years, putting up with the slow plod through these projects, and for all of the useful tools and skills I have learned.

To Jonathan, Vijay, Masha, and Matt G., and all of the other NR peers I've chatted with, for all of the nerdy, science discussions

To the Friday Night Dinner group, for the years of constant fun and turmoil as we horribly botched our way through a couple of campaigns

To Carla Corbit and Margo Miller, for all of the great times I have had working together with you during the practices, and especially during the fencing tournaments.

To all the crazy kids on the Caltech fencing team, for making practices and tournaments such fun to be a part of.

To JoAnn Boyd, for all the goofy faces, terrible (amazing) puns, and timely procrasti-chats.

To Sherwood, Jonas, Mike, Matt O., Denise, and all of the other cool cats on 3rd floor Cahill, for all of the fun moments between working hours.

To Sarah Gossan, for always bringing glam, glitter and cheer to the office, as well as a touch of that quintessentially British flair.

To John, Yeou, Mary, Steven, Andrew, Cameron, and all my buddies from before Caltech who have put up with my weirdness longer than most.

To Nicole Crione and all of the wonderful people I've met at her creative writing workshops over the past couple years.

To all of my other peers, collaborators, friends and relatives who've helped me on my journey.

And last (and least?) to that small bunch of obnoxious people I am legally obligated to recognize as my younger siblings: Guinevere, Patrick, Nicholas, Jacob, Eric, and Zachary (that's right, I went in reverse order for once). Thanks for putting up with your older brother; love y'all!

ABSTRACT

As the aLIGO and Virgo detectors continue to improve their sensitivity for observing gravitational waves from merging compact binaries, they will require ever more precise theoretical predictions to extract a detailed understanding of the physics governing these merging systems. This thesis discusses advancements within computing the gravitational waveforms along two avenues of research: the continued development of a spectral Cauchy-Characteristic Extraction (CCE) code and the presentation of a novel method called ‘Tidal Splicing’ for generating waveforms for binary neutron star (BNS), black hole-neutron star (BHNS), and even Beyond GR systems.

Due to the finite extents of typical 3+1 simulations of merging binaries, the waveforms they generate can suffer from near-zone effects and lingering gauge ambiguities. CCE was developed in order to evolve radiating gravitational waves as they propagate outward to future null infinity, allowing studies connecting the dynamical spacetime of binary evolutions to effects seen by distant observers, such as superkicks, and angular and linear momentum fluxes. A recent spectral version of CCE showed promising improvements in accuracy and efficiency over the older finite-differencing code, PittNull. However, lingering issues with the numerics and implementation of the theory prevented it from wide spread use. We detail the developments updated its initial release and demonstrate the enhancement in accuracy they yield beyond the capabilities of PittNull.

The method of Tidal Splicing enhances the inexpensive Post-Newtonian (PN) tidal corrections with BBH waveforms from numerical simulations to generate waveforms corresponding to inspiraling BNS or BHNS systems. This leverages the accuracy of numerical BBH waveforms to effectively replace the corresponding unknown PN terms. In addition, by picking individual terms in the PN tidal expansions to include, then comparing with existing numerical simulations, we are able to probe the significance of each contribution to the total difference in evolution between BBH and BNS or BHNS inspirals. We also demonstrate how the splicing concepts used for tidal effects can be extended in order to model waveforms with corrections according to theories beyond GR using an example case of a resonating ultra-compact object.

PUBLISHED CONTENT AND CONTRIBUTIONS

Barkett, K. and Scheel, M. A. and Szilágyi B. (2019). “Spectral Cauchy-Characteristic Extraction of gravitational wave news”. In Preparation.

K.B. participated in the conception of the project, improving the numerical methods, performing the tests of the code, and writing the manuscript

Barkett, K. and Scheel, M. A., et al. (2016). “Gravitational waveforms for neutron star binaries from binary black hole simulations”. In: *Phys. Rev. D.* 93(4):044064, Feb 2016. doi: 10.1103/PhysRevD.93.044064

K.B. participated in the conception of the project, deriving the underlying theory, performing the comparisons and analysis, and writing the manuscript.

Barkett, K. and Chen Y. and Scheel, M. A. and Varma V. (2019). “Generating gravitational waveforms for binaries with neutron stars using Tidal Splicing”. In Preparation.

K.B. participated in the conception of the project, expanding the analytic expressions, extending the model, performing the comparisons and analysis of the waveforms, and writing the manuscript

Barkett, K. and Chen Y. (2019). “Computing gravitational waves beyond GR with splicing methods”. In Preparation.

K.B. participated in the conception of the project, deriving the analytic expressions, comparing the computed waveforms, and writing the manuscript

TABLE OF CONTENTS

Acknowledgements	iii
Abstract	iv
Published Content and Contributions	v
Table of Contents	vi
List of Illustrations	vii
List of Tables	viii
Chapter I: Introduction	1
Chapter II: Spectral Cauchy-Characteristic Extraction	4
2.1 Introduction	4
2.2 Summary of characteristic formulation	7
2.3 Inner Boundary Formalism	9
2.4 Volume Evolution	16
2.5 Scri Extraction	21
2.6 Code Tests	26
2.7 Appendices	37
Chapter III: Introduction to Tidal Splicing	43
3.1 Preface	43
3.2 Introduction	43
3.3 Methods	45
3.4 Discussion	50
3.5 Acknowledgments	50
Chapter IV: Tidal Splicing for BHNS and BNS Systems	52
4.1 Introduction	52
4.2 Post-Newtonian Theory	53
4.3 Expanding PN Tidal Corrections	60
4.4 Tidal Splicing	64
4.5 Results	68
4.6 Appendices	75
Chapter V: Resonating Ultra-Compact Object Splicing Model	88
5.1 Preface	88
5.2 Theoretical Framework	88
5.3 Splicing Details	90
5.4 Test Results	91
Bibliography	94

LIST OF ILLUSTRATIONS

<i>Number</i>	<i>Page</i>
2.1 Penrose diagram showing a typical CCE setup	6
2.2 The difference between the numerically evolved News function and the analytic solution for the linearized analytic test	29
2.3 The difference between the numerically evolved News function and the analytic solution for the Teukolsky wave test	31
2.4 The absolute values of the News modes for the (2,2) and (2,0) for both the SpEC and PittNull CCE codes in the Bouncing BH test	32
2.5 The absolute values of the News modes for the (3,3) and (4,4) for both the SpEC and PittNull CCE codes in the Bouncing BH test	33
2.6 The absolute values of the (2,2) News modes from our SpEC code for different coordinate world tube radii \check{r} in the Bouncing BH test	36
2.7 The absolute values of the News modes for the (2,0) and (3,0) for both the SpEC and PittNull CCE codes in the gauge wave test	38
3.1 Phase difference between 1PN TaylorT4 tidal splicing and numerical waveforms	45
3.2 Phase difference between TaylorF2 tidal splicing and numerical waveforms	48
3.3 Phase accumulation of 1PN Tidal effects	49
4.1 The dynamical tides amplification κ_ℓ as a function of orbital frequency	64
4.2 Distribution of mismatches against the inspiral of the BHNS, $q = 1$, nonspinning simulation across sky locations.	71
4.3 Distribution of mismatches against the inspiral of all numerical simulations	72
4.4 Distribution of mismatches with only (2, \pm 2) mode against the inspiral of all numerical simulations with all modes	74
5.1 Distinguishability of spliced waveform of resonating ultra-compact object	92

LIST OF TABLES

<i>Number</i>	<i>Page</i>
4.1 List of parameters for numerical simulations considered	69
4.2 Universal Relations relating the static dimensionless deformability to various other dimensionless tidal parameters using Eq 4.70	82
4.3 Estimates of PN tidal self-cross terms, $\bar{\omega}_{\text{ISCO}} = 6^{-3/2}$	86
4.4 Estimates of PN tidal self-cross terms, $\bar{\omega}_{\text{test}} = \bar{\omega}_{\text{ISCO}}/5$	86

Chapter 1

INTRODUCTION

One prediction of Einstein's theory of General Relativity (GR) is the existence of gravitational waves, ripples of gravity propagating at the speed of light which very subtly distort the space they pass through. Similar to how accelerating electrons and protons emit electromagnetic radiation, a pair of massive objects orbiting around each other under the influence of gravity will emit gravitational radiation. The more massive the objects and the faster they are moving, the larger these ripples will be.

When two objects are orbiting each other in a binary, the emission of gravitational radiation will cause the orbits to slowly decay and the objects to orbit closer to each other. As the orbit shrinks, they orbit about each other faster, leading to a greater emission of gravitational radiation. If there are no other effects influencing the orbits, this process will continue, slowly accelerating the objects in the binary closer to each other until they collide, merging into a single object. The gravitational waves will be largest when a pair of ultra dense objects are orbiting in close proximity to each other. Thus, the binaries which will generate the strongest gravitational waves will be those comprising of either a Black Holes (BH) or a Neutron Stars (NS) during the last, decaying orbits as they coalesce into a single object.

For most of the past century, gravitational waves even from colliding BHs or NSs were far too weak for observatories on Earth to detect, as the source of those systems typically originate hundreds of millions or billions of light-years away. It has only been in the past few years, with the impressive developments with the aLIGO [2] and Virgo [14] detectors, has the technology improved to the point where these faint signals can be observed, opening a new window to peer at the rest of the universe. The first detection of colliding BHs, GW150914 [7] (named according to the date it was detected), heralded the start of gravitational wave astronomy. This direct detection of gravitational waves led to the 2017 Nobel Prize in Physics. There have since been a number of additional observations of the colliding BHs [6, 10–12], as well as a detection of colliding NSs, GW170817 [13]. As the detectors push to ever more sensitive configurations, the number of expected gravitational wave signals they are expected to observe will only increase.

The configuration of the orbiting binary, the mass of each BH or NS, how much they are rotating about their axis, and so forth, all imprint different signatures on the resulting signal pattern. One of the challenges facing these detectors is how to extract the signal of a passing gravitational wave from the noise inherent within the detector. We may detect such a signal by comparing the observed signal against a template bank of theoretical signals at various possible configurations, and finding which configurations best match the signal. From this, we can estimate the configuration of the binary which generated the gravitational waves. However, these estimates are only as good as the

signals used to generate the template bank.

The primary difficulty of computing the possible gravitational waves to populate the template bank is that there are no closed form solutions to describing the orbits of a binary evolving according to GR. As such, researchers employ other methods to compute the theoretical signals, from numerical simulations to analytic approximants and calibrated models, each with their own advantages and disadvantages.

Numerical simulations are preferable, as they are the full calculation of the binary within GR using computational techniques. Current simulations of these binaries employ a "3+1" decomposition, where they compute the Einstein equations across 3 spatial dimension at a single time slice, then using those results in order to advance the simulations forward to the next discrete time slice. One limitation of this formulation is that such simulations only extend to a compact spatial region around binary and nowhere near the typically millions to billions of light-years of intervening distance between the binary and detectors on Earth. While there are a few methods for estimating the resulting gravitational waves from the outer edge of the simulations, they are not perfect and the particular way in which the simulation chooses its coordinates can affect them.

These limitations led to the development of a method called Cauchy-Characteristic Extraction (CCE) [35, 36, 39], which can simulate how pattern of radiating gravitational waves propagate outward to arbitrarily far distances. It does so by way of a "2+1+1" decomposition of the Einstein equations, which evolves the spacetime along the trajectories of the gravitational waves. While this method does not work for the intense, dynamical gravity near compact orbiting objects, CCE can extract the results from the outer edge of the 3+1 simulation to compute the final signals which would be observable from Earth. This also means that we can use CCE in order to study how the local GR physics connect to measurable quantities by distant observers, such as measuring the ringdown [32], as well as kicks and fluxes of angular and linear momentum from merging binaries.

While an older version of a finite-differencing CCE code has been available for use [21, 135, 136] it was only recently with the development of a spectral version of CCE which promised to be fast enough for large scale use. Chapter 2 includes detailed discussion of the numerous changes and improvements made to this spectral CCE code since its initial implementation in [87–89]. It also includes various tests of the code demonstrating its accuracy and efficiency in computing the radiated gravitational waves.

Unfortunately, full 3+1 simulations are computationally expensive and this expense scales with the difficulty of the object being simulated. While BHs are relatively smooth objects, where the simulations can excise most of the interior space behind the event horizon, NSs are made of extremely dense matter. The matter influences and is influenced by the binary's orbit and thus alters gravitational wave signal. So while numerical developments allow current simulations of orbiting BHs to be run relatively efficiently, the behavior of the matter within the NSs drastically increases the simulation cost. Currently, using numerical simulations for systems with NSs to populate template banks is computationally prohibitive.

An alternative method of generating the signals from these binaries is analytic approximants which are cheap to generate while the orbit is decaying. Within these approximations, the NSs are treated as corrections to binaries comprised of only BHs. However, they are approximations so their accuracy worsens as the objects near collision. Ironically, it is the corrections corresponding to the BH only system which are expected become inaccurate before the additional NS corrections fully manifest in the gravitational wave signal. In this sense, the analytic approximants for NSs in a binary are limited by the relatively poor knowledge of the BHs.

This particular dichotomy of relatively efficient simulations of BHs and cheap analytic corrections for NSs which gives rise to a hybrid method of generating gravitational wave signals for binaries with NSs that I have innovated called ‘Tidal Splicing’. This method works by treating the signal from the numerical simulations as if it had been generated as a corrected analytic approximant. Then the analytic corrections for the NSs are added on top of the numerical results, generating a new signal which approximates the orbital behavior as if the binary had been made of NSs originally. This also allows us to disentangle the contributions of individual effects, such as spinning NSs and dynamical tides, to the overall signal by tuning which effects we include when splicing the waveform. Chapters 3 and 4 give a full description of the concepts behind this model and results when compared with numerical simulations with NSs.

There are also theoretical motivations for considering the case in which black holes are not perfectly ‘black’, but instead are ultra-compact objects with surfaces just outside the event horizon. While such differences would be nearly imperceptible to electromagnetic observations, these objects would exhibit distinct inspiraling evolution from BHs or NSs, thus requiring additional work to model the patterns of gravitational waves they emit. Chapter 5 will demonstrate how splicing methods provides the potential for modeling such additional corrections to exotic objects in orbiting binaries.

Chapter 2

SPECTRAL CAUCHY-CHARACTERISTIC EXTRACTION

2.1 Introduction

The discovery of GW150914 [7] heralded the beginning of gravitational wave astronomy. In the subsequent years that detection has been followed up by a number of other signals observed from binary black hole (BBH) mergers [6, 10–12], as well as from the merger of a binary neutron star (BNS) system [13]. As the aLIGO [2] and Virgo [14] detectors push to ever greater sensitivities, the number of expected observations will continue to grow.

Extracting the signals from the noise involves matching the incoming data against a template bank of theoretically expected waveforms generated across possible binary configurations. The efficacy of extracting the configuration parameters (for instance, masses and spins of the binary components) from a given signal depends on the fidelity of the computed waveforms comprising the template bank; this is because errors in the template bank will bias the estimated parameters. The only *ab initio* method of generating accurate theoretical waveforms for merging BBH systems is via numerical relativity: the numerical solution of the full Einstein equations on a computer. Other methods of generating theoretical BBH waveforms, such as Effective One-Body solutions [53] and phenomenological models [101, 104], are calibrated to numerical relativity.

One limitation of numerical relativity simulations is that they all rely on a Cauchy approach in which the spacetime is decomposed into a foliation of spacelike slices, and the solution marches from one slice to the next. Such an approach can compute the solution to Einstein’s equations only in a region of spacetime with finite spatial and temporal extents bounded around the compact objects, whereas the gravitational radiation is defined at future null infinity \mathcal{I}^+ . Extracting the waveform signal from the simulations with these finite extents requires additional work.

The most common method of extracting the gravitational radiation from a numerical relativity simulation is to compute quantities such as the Newman-Penrose scalar Ψ_4 [119] or the Regge-Wheeler and Zerilli scalars [140] at some large but finite distance from the near zone (perhaps $100\text{--}1000M$, where M is the total mass of the system), typically on coordinate spheres of constant coordinate radius r . Because these quantities or the methods of computing them include finite-radius effects, these quantities are computed on a series of shells at different radii r , fit to a polynomial in $1/r$, and then extrapolated to infinity by reading off the $1/r$ coefficient of the polynomial [57]. As the extraction surfaces are shells of constant coordinate radii, the choice of gauge implemented in the simulation can contaminate the resulting waveforms. Furthermore, if the shells are too close to the orbiting binary, the extrapolation procedure might not remove all of the near-zone effects.

An alternative method for computing gravitational radiation in numerical relativity is to solve the full Einstein equations in a domain that extends all the way to \mathcal{I}^+ , where gravitational waves can

be measured. This can be done by rewriting Einstein’s equations using a characteristic formalism [54, 122, 139], in which the equations are solved on outgoing null surfaces that extend to \mathcal{S}^+ . This formalism chooses coordinates that correspond to distinct outward propagating null rays, so it fails in the dynamical, strong field regime at any location where outgoing null rays intersect (i.e., caustics). Because of this, characteristic evolution is unable to evolve the near-field region of a merging binary system, so it cannot accomplish a BBH simulation on its own. However, it is possible to combine an interior numerical relativity code that solves the equations on Cauchy slices with an exterior characteristic code that solves them on null slices; this approach is known as Cauchy-Characteristic Extraction (CCE). (See Fig. 2.1.)

Specifically, CCE takes metric data known on a world tube Γ (thick red line in Fig. 2.1) that lies on or inside the boundary of a Cauchy evolution (red region), and treats it as inner boundary data for a characteristic evolution outward along null slices (blue curves). Because the combined CCE system uses the full Einstein equations, it produces the correct solution at \mathcal{S}^+ , with the characteristic evolution properly resolving near-zone effects. The gravitational radiation is computed according to a particular inertial observer at \mathcal{S}^+ (green curve). This particular observer is related to any other inertial observer by a single BMS transformation [139] (the group of Lorentz boosts, rotations, and supertranslations [138]), so up to this BMS transformation the waveform is independent of the gauge chosen by the Cauchy evolution.

The first code to implement CCE was the PittNull code [35, 36, 39]. Since its initial implementation there have been a number of improvements made, and the current iteration of that code utilizes stereographic angular coordinate patches, finite-differencing, and a null parallelogram scheme with fixed time steps for integrating in the null and time directions. Overall the code is second-order convergent with resolution [21, 135, 136]. Compared to waveforms computed from a Cauchy code by evaluating Ψ_4 at finite radii and extrapolating to $r \rightarrow \infty$ as described above, waveforms extracted via CCE using PittNull were shown to better remove gauge effects and to better resolve the $m = 0$ memory modes [125, 134, 151].

Currently, PittNull requires thousands of CPU-hours to compute a waveform at \mathcal{S}^+ given worldtube output from a typical Cauchy BBH simulation at multiple resolutions [87]. While that cost is smaller than the computational expense of the Cauchy simulation, it is still unwieldy, and is likely one reason that most Cauchy numerical-relativity codes do not use CCE despite the availability of PittNull. Because the metric in the characteristic region is smooth, the computational cost of characteristic evolution should be greatly reduced by using spectral methods instead of finite differencing. Such a spectral implementation of characteristic evolution has been introduced in the SpEC framework [87–89]. Their tests showed improved speed and accuracy over the finite-difference implementation of PittNull [87, 88].

Our work here describes improvements in accuracy, efficiency, and robustness to the code described in [87–89]. In particular, we discuss an improved handling of the integration along the null slices, we clarify issues related to the particular choice of coordinates along the null slice, and we implement

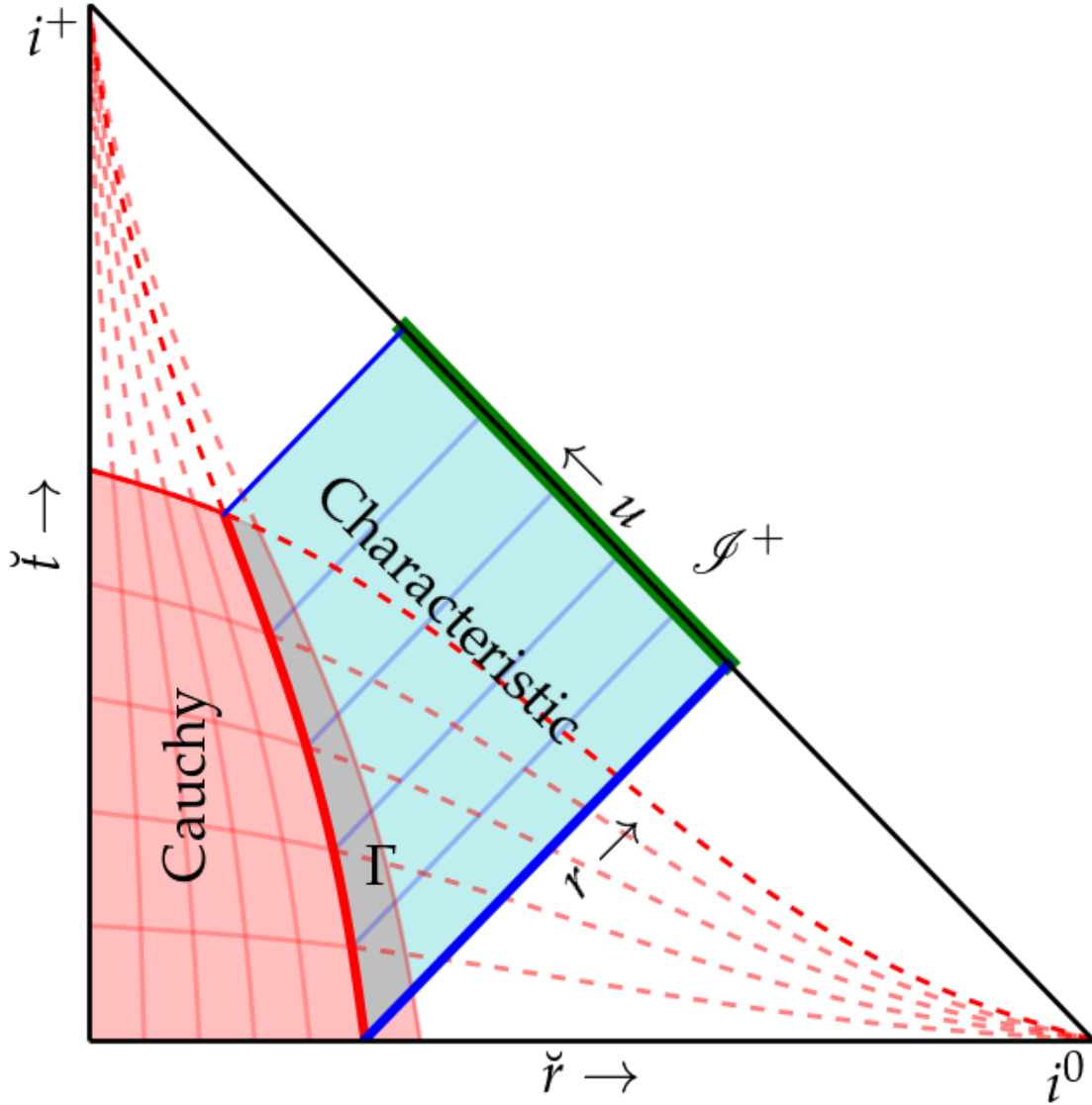


Figure 2.1: Penrose diagram showing a typical CCE setup. The metric is evolved using 3+1 methods in the Cauchy region (shaded red) and with null methods in the characteristic region (shaded blue). The Cauchy and characteristic regions overlap. Curves of constant \check{t} or \check{r} , the Cauchy coordinates, are shown in red, and are shown as dashed curves outside the Cauchy region, where they extend to spatial infinity i^0 or future temporal infinity i^+ . Null curves of constant u are shown in blue. Given data on an worldtube Γ (thick red curve) and on an initial null slice (thick blue curve), the characteristic evolution computes the full metric in the characteristic region. In Section 2.3 we describe the interface from Cauchy to Bondi coordinates on Γ . In Section 2.4 we describe the characteristic evolution. In Section 2.5 we discuss computing the News function at \mathcal{S}^+ (thick green curve) and transforming it to coordinates corresponding to a free-falling observer.

better handling of the inertial coordinates at \mathcal{I}^+ . We demonstrate through a series of analytic tests that our version of CCE can compute waveforms with much lower computational cost than PittNull.

We start with a brief summary of the Bondi metric and the null formulation of the Einstein equations in Sec 2.2. A detailed explanation for how CCE works can be broken up into three distinct parts: the inner boundary formalism, the volume characteristic evolution, and the \mathcal{I}^+ extraction, which we describe in subsequent sections. Sec 2.3 describes the means by which the metric data known on a world tube is converted into Bondi form to serve as the inner boundary values for the characteristic evolution system. Sec 2.4 discusses the process of evolving Einstein's equations from the inner boundary to \mathcal{I}^+ . Sec 2.5 explains how to take the metric data computed on \mathcal{I}^+ and extract the Bondi news function in the frame of an inertial observer at \mathcal{I}^+ . In Sec 2.6, we describe code tests and performance.

Throughout this paper, indices with Greek letters (μ, ν, \dots) correspond to spacetime coordinates, lowercase Roman letters (i, j, \dots) to spatial coordinates, and capitalized Roman letters (A, B, \dots) to angular coordinates, and we choose a system of geometrized units ($c = G = 1$). For convenience, we have included a definitions key in appendix 2.7.

2.2 Summary of characteristic formulation

In the characteristic region (see Fig. 2.1), we adopt a coordinate system $x^\mu = (u, r, x^A)$, where u is the coordinate labeling the outgoing null cones, r is an areal radial coordinate, and x^A are the angular coordinates. Note that a surface of constant (u, x^A) is an outgoing null ray parameterized by r ; for this reason we sometimes call r a ‘‘radinull’’ coordinate. The metric can then be expressed in the Bondi-Sachs form [54, 139],

$$ds^2 = - \left(e^{2\beta} (1 + rW) - r^2 h_{AB} U^A U^B \right) du^2 - 2e^{2\beta} dudr - 2r^2 h_{AB} U^B dudx^A + r^2 h_{AB} dx^A dx^B, \quad (2.1)$$

where W corresponds to the mass aspect, U^A to the shift, β to the lapse, and h_{AB} to the spherical 2-metric. The quantity h_{AB} has the same determinant as the unit sphere metric q_{AB} , $|h_{AB}| = |q_{AB}|$. An additional intermediate quantity, Q_A , is defined to reduce the evolution equations to a series of 1st order PDEs,

$$Q_A = r^2 e^{-2\beta} h_{AB} U_{,r}^B. \quad (2.2)$$

Instead of expressing the metric in terms of tensorial objects, we employ a complex dyad so that the metric components can be computed as spin-weighted scalars, and each of these scalars can be expanded in terms of Spin-Weighted Spherical Harmonics (SWSHes) of the appropriate spin weight; see Appendix 2.7 for details about SWSHes. The dyad q^A has the following properties:

$$q^A q_A = 0, \quad (2.3)$$

$$q^A \bar{q}_A = 2. \quad (2.4)$$

If we define q_{AB} and q^{AB} such that

$$q_{AB} = \frac{1}{2}(q_A \bar{q}_B + \bar{q}_A q_B), \quad (2.5)$$

$$q^{AC} q_{CB} = \delta_B^A, \quad (2.6)$$

then

$$q^A = q^{AB} q_B. \quad (2.7)$$

We express the metric coefficients and the quantity Q_A in terms of spin-weighted scalars J , K , U , and Q , defined by

$$J = \frac{1}{2} h_{AB} q^A q^B, \quad (2.8)$$

$$K = \frac{1}{2} h_{AB} q^A \bar{q}^B, \quad (2.9)$$

$$U = q_A U^A, \quad (2.10)$$

$$Q = Q_A q^A. \quad (2.11)$$

The determinant condition on h_{AB} defines a relationship between J and K as

$$K = \sqrt{1 + J\bar{J}}. \quad (2.12)$$

We introduce one more intermediate variable H , the time derivative of J along slices of constant r ,

$$H = J_{,u}|_{r=\text{const}} \quad (2.13)$$

Evaluating the components of the Einstein equation $G_{\mu\nu} = 0$ provides a system of equations for the quantities β , Q , U , W , and H :

$$\beta_{,r} = \mathcal{N}_\beta, \quad (2.14)$$

$$(r^2 Q)_{,r} = -r^2 (\bar{\delta} J + \delta K)_{,r} + 2r^4 \delta (r^{-2} \beta)_{,r} + \mathcal{N}_Q, \quad (2.15)$$

$$U_{,r} = r^{-2} e^{2\beta} Q + \mathcal{N}_U, \quad (2.16)$$

$$(r^2 W)_{,r} = \frac{1}{2} e^{2\beta} \mathcal{R} - 1 - e^\beta \delta \bar{\delta} e^\beta + \frac{1}{4} r^{-2} (r^4 (\delta \bar{U} + \bar{\delta} U))_{,r} + \mathcal{N}_W, \quad (2.17)$$

$$2(rH)_{,r} = ((1 + rW)(rJ)_{,r})_{,r} - r^{-1} (r^2 \delta U)_{,r} + 2r^{-1} e^\beta \delta^2 e^\beta - (rW)_{,r} J + \mathcal{N}_J, \quad (2.18)$$

where

$$\mathcal{R} = 2K - \delta \bar{\delta} K + \frac{1}{2} (\bar{\delta}^2 J + \delta^2 \bar{J}) + \frac{1}{4K} (\bar{\delta} \bar{J} \delta J - \bar{\delta} J \delta \bar{J}), \quad (2.19)$$

and $\mathcal{N}_\beta, \mathcal{N}_W, \mathcal{N}_Q, \mathcal{N}_U$, and \mathcal{N}_J are the terms nonlinear in J and its derivatives, as according to [39]. Appendix 2.7 provides the full expressions for these equations.

The equations are presented in a useful hierarchical order: the right-hand side of the β equation involves only J and its spatial derivatives, the right-hand side of the Q equation involves only J and β and their spatial derivatives, and so on for the other equations. Therefore, given data for all quantities on the inner boundary as well as J on an initial $u = \text{constant}$ null slice, we can integrate the series of equations in Eqs. (2.14)–(2.18) on that slice from the inner boundary to $r = \infty$ to obtain β, Q, U, W and then H in sequence on that slice. Then, given $H = J_{,u}|_{r=\text{const}}$ on that slice, we can integrate forward in time to obtain J on the next null slice.

2.3 Inner Boundary Formalism

The coordinates used to evolve Einstein's equations in the Cauchy region (red area of Fig. 2.1) are generally different from the Bondi coordinates discussed in Section 2.2. The Cauchy coordinates are chosen to make the interior evolution proceed without encountering coordinate singularities; the procedure for choosing these coordinates is complicated and typically involves coordinates that are evolved along with the solution [26, 60, 112, 128, 141, 147]. Therefore, for CCE we must transform from arbitrary Cauchy coordinates to Bondi coordinates at the worldtube. Here, in the Cauchy region, for simplicity we assume Cartesian coordinates (\check{t}, \check{x}^i) in which the world tube hypersurface Γ (which is chosen by the Cauchy code) is a surface of constant \check{r} , where $\check{r} = \sqrt{\check{x}^2 + \check{y}^2 + \check{z}^2}$. We also define angular coordinates $\check{x}^{\check{A}} = (\check{\theta}, \check{\phi})$ in the usual way from the Cartesian coordinates \check{x}^i .

The world tube serves as the inner boundary of the characteristic domain (see Fig. 2.1). On this boundary, we assume that the interior Cauchy code provides the spatial 3-metric $g_{\check{ij}}$, the shift $\beta^{\check{i}}$, and the lapse $\check{\alpha}$, along with the \check{r} and \check{t} derivatives of each of these quantities. Angular derivatives of these quantities are necessary as well; however, we can compute those numerically within the worldtube itself, so they need not be provided *a priori*.

Ref. [36] describes how to take the data provided by the interior Cauchy code and convert it into Bondi form (Eq. (2.1)) to extract the inner boundary values of the evolution quantities $(J_{|\Gamma}, \beta_{|\Gamma}, \dots)$. This section is primarily a summary of their results; however, we use different notation than Ref. [36].

Intermediate Null Coordinates

Our goal is to transform from the coordinates (\check{t}, \check{x}^i) into Bondi coordinates. It is simplest to proceed in two steps: the first step, described in this subsection, is to construct coordinates foliated by outgoing null geodesics. The second step, described in Section 2.3, will be to transform from these intermediate coordinates to Bondi coordinates.

We begin by constructing the null generator $\ell^{\check{\mu}}$, which involves the unit outward spatial vector normal to the world tube's surface, $s^{\check{\mu}}$, and the unit timelike vector normal to a slice of constant \check{t} , $n^{\check{\mu}}$:

$$s^{\check{\mu}} = \left(0, \frac{g^{\check{ij}} \check{x}_{\check{j}}}{\sqrt{g^{\check{ij}} \check{x}_{\check{i}} \check{x}_{\check{j}}}} \right), \quad (2.20)$$

$$n^{\check{\mu}} = \frac{1}{\check{\alpha}} (1, -\beta^{\check{i}}). \quad (2.21)$$

Eq. (2.20) depends on our simplifying assumption that the world tube is spherical in Cauchy coordinates, and can be generalized. From these, the null generator is

$$\ell^{\check{\mu}} = \frac{n^{\check{\mu}} + s^{\check{\mu}}}{\check{\alpha} - g_{\check{i}\check{j}}\beta^{\check{i}}s^{\check{j}}}. \quad (2.22)$$

The time derivatives of these vectors are

$$s^{\check{\mu}}_{,\check{i}} = \left(0, (-g^{\check{i}\check{j}} + s^{\check{i}}s^{\check{j}}/2)s^{\check{k}}g_{\check{j}\check{k},\check{i}} \right), \quad (2.23)$$

$$n^{\check{\mu}}_{,\check{i}} = \frac{1}{\check{\alpha}^2} \left(-\check{\alpha}_{,\check{i}}, \check{\alpha}_{,\check{i}}\beta^{\check{i}} - \check{\alpha}\beta^{\check{i}}_{,\check{i}} \right), \quad (2.24)$$

$$\ell^{\check{\mu}}_{,\check{i}} = \frac{n^{\check{\mu}}_{,\check{i}} + s^{\check{\mu}}_{,\check{i}} + \ell^{\check{\mu}} \left(-\check{\alpha}_{,\check{i}} + g_{\check{i}\check{j},\check{i}}\beta^{\check{j}}s^{\check{j}} + g_{\check{i}\check{j}}\beta^{\check{j}}_{,\check{i}}s^{\check{j}} + g_{\check{i}\check{j}}\beta^{\check{j}}s^{\check{j}}_{,\check{i}} \right)}{\check{\alpha} - g_{\check{i}\check{j}}\beta^{\check{i}}s^{\check{j}}}. \quad (2.25)$$

We will now construct a null coordinate system based on outgoing null geodesics generated by $\ell^{\check{\mu}}$. Let λ be an affine parameter along these geodesics such that the value of λ on the world tube Γ is $\lambda|_{\Gamma} = 0$. We also define a null coordinate \bar{u} and angular coordinates $\bar{x}^{\bar{A}} = (\bar{\theta}, \bar{\phi})$ that obey $\bar{u} = \check{t}$ and $\bar{x}^{\bar{A}} = \check{x}^{\bar{A}}$ on the world tube, and are constant along the outgoing null geodesic generated by $\ell^{\check{\mu}}$. Thus we have defined a new intermediate coordinate system, $\bar{x}^{\bar{\mu}} = (\bar{u}, \lambda, \bar{\theta}, \bar{\phi})$ and we will express the metric $g_{\bar{\mu}\bar{\nu}}$ in these intermediate coordinates.

To do this, we will need to write down the coordinate transformation from $\check{x}^{\check{\mu}}$ to $\bar{x}^{\bar{\mu}}$ in a neighborhood of the world tube, not just on the world tube itself, because we need derivatives of this transformation. In particular, we will need derivatives with respect to λ . The derivative of the metric components $g_{\check{\mu}\check{\nu}}$ along the null direction simply is

$$g_{\check{\mu}\check{\nu},\lambda} = \ell^{\check{\gamma}} g_{\check{\mu}\check{\nu},\check{\gamma}}. \quad (2.26)$$

The evolution of the coordinates $\check{x}^{\check{\mu}}$ along null geodesics implies that in a neighborhood of the world tube

$$\check{x}^{\check{\mu}}_{,\lambda} = \ell^{\check{\nu}} \partial_{\check{\nu}} \check{x}^{\check{\mu}} = \ell^{\check{\mu}}. \quad (2.27)$$

Given the new coordinates $\bar{x}^{\bar{\mu}}$, the metric components in these coordinates are

$$g_{\bar{\mu}\bar{\nu}} = \frac{\partial \check{x}^{\check{\alpha}}}{\partial \bar{x}^{\bar{\mu}}} \frac{\partial \check{x}^{\check{\beta}}}{\partial \bar{x}^{\bar{\nu}}} g_{\check{\alpha}\check{\beta}}. \quad (2.28)$$

On the world tube,

$$\begin{aligned} \frac{\partial \check{x}^{\check{\alpha}}}{\partial \bar{x}^{\bar{A}}} &= \frac{\partial \check{x}^{\check{i}}}{\partial \bar{x}^{\bar{A}}}, \\ \frac{\partial \check{t}}{\partial \bar{u}} &= 1, \end{aligned}$$

$$\frac{\partial \check{x}^i}{\partial \bar{u}} = 0, \quad (2.29)$$

where the term $\partial \check{x}^i / \partial \bar{x}^{\bar{A}}$ the standard Cartesian to spherical Jacobian. The above values of the Jacobians hold only on the world tube. In addition to the metric itself, we will also need first derivatives of the metric, including the derivative with respect to λ . This requires the λ derivatives of the Jacobians evaluated on the world tube, which we represent here as

$$\begin{aligned} \frac{\partial^2 \check{x}^{\check{\mu}}}{\partial \bar{x}^{\bar{A}} \partial \lambda} &= \frac{\partial \ell^{\check{\mu}}}{\partial \bar{x}^{\bar{A}}} = \ell^{\check{\mu}}_{,\bar{A}}, \\ \frac{\partial^2 \check{x}^{\check{\mu}}}{\partial \bar{u} \partial \lambda} &= \frac{\partial \ell^{\check{\mu}}}{\partial \bar{u}} = \ell^{\check{\mu}}_{,\bar{u}}, \end{aligned} \quad (2.30)$$

where we have made use of Eq. (2.27).

We are now ready to write out the metric in these intermediate coordinates by taking the expression in Eq. (2.28) and taking the appropriate derivatives,

$$\begin{aligned} g_{\bar{u}\lambda} &= -1, \\ g_{\lambda\lambda} &= g_{\lambda\bar{A}} = 0, \\ g_{\bar{u}\bar{u}} &= g_{\check{i}\check{i}}, \\ g_{\bar{u}\bar{A}} &= \frac{\partial \check{x}^{\check{i}}}{\partial \bar{x}^{\bar{A}}} g_{\check{i}\check{i}}, \\ g_{\bar{A}\bar{B}} &= \frac{\partial \check{x}^{\check{i}}}{\partial \bar{x}^{\bar{A}}} \frac{\partial \check{x}^{\check{j}}}{\partial \bar{x}^{\bar{B}}} g_{\check{i}\check{j}}, \\ g_{\bar{A}\bar{B},\lambda} &= \frac{\partial \check{x}^{\check{i}}}{\partial \bar{x}^{\bar{A}}} \frac{\partial \check{x}^{\check{j}}}{\partial \bar{x}^{\bar{B}}} g_{\check{i}\check{j},\lambda} + \left(\ell^{\check{\mu}}_{,\bar{A}} \frac{\partial \check{x}^{\check{i}}}{\partial \bar{x}^{\bar{B}}} + \ell^{\check{\mu}}_{,\bar{B}} \frac{\partial \check{x}^{\check{i}}}{\partial \bar{x}^{\bar{A}}} \right) g_{\check{\mu}\check{i}}, \\ g_{\bar{A}\bar{B},\bar{u}} &= \frac{\partial \check{x}^{\check{i}}}{\partial \bar{x}^{\bar{A}}} \frac{\partial \check{x}^{\check{j}}}{\partial \bar{x}^{\bar{B}}} g_{\check{i}\check{j},\check{i}}, \\ g_{\bar{u}\bar{A},\lambda} &= \ell^{\check{\mu}}_{,\bar{A}} g_{\check{i}\check{\mu}} + \frac{\partial \check{x}^{\check{i}}}{\partial \bar{x}^{\bar{A}}} \left(g_{\check{i}\check{i},\lambda} + \ell^{\check{\mu}}_{,\bar{u}} g_{\check{i}\check{\mu}} \right), \end{aligned} \quad (2.31)$$

and

$$\begin{aligned} g^{\bar{u}\bar{u}} &= g^{\bar{u}\bar{A}} = 0, \\ g^{\bar{u}\lambda} &= -1, \\ g^{\bar{A}\bar{B}} g_{\bar{B}\bar{C}} &= \delta_{\bar{C}}^{\bar{A}}, \\ g^{\lambda\bar{A}} &= g^{\bar{A}\bar{B}} g_{\bar{u}\bar{B}}, \\ g^{\lambda\lambda} &= -g_{\bar{u}\bar{u}} + g^{\lambda\bar{A}} g_{\bar{u}\bar{A}}, \\ g^{\bar{A}\bar{B}}_{,\lambda} &= -g^{\bar{A}\bar{C}} g^{\bar{B}\bar{D}} g_{\bar{C}\bar{D},\lambda}, \\ g^{\lambda\bar{A}}_{,\lambda} &= g^{\bar{A}\bar{B}} \left(g_{\bar{u}\bar{B},\lambda} - g^{\lambda\bar{C}} g_{\bar{B}\bar{C},\lambda} \right). \end{aligned} \quad (2.32)$$

Bondi Form of Metric

Given the intermediate null coordinates and the metric in that coordinate system, we apply one last coordinate transformation to obtain Bondi coordinates. We define Bondi coordinates (u, r, θ, ϕ) ,

where r is a surface area coordinate, $u = \bar{u}$, $\theta = \bar{\theta}$, and $\phi = \bar{\phi}$. The surface area coordinate r is defined by

$$r = \left(\frac{|g_{AB}|}{|q_{AB}|} \right)^{\frac{1}{4}} = \left(\frac{|g_{\bar{A}\bar{B}}|}{|q_{\bar{A}\bar{B}}|} \right)^{\frac{1}{4}}, \quad (2.33)$$

where $q_{\bar{A}\bar{B}}$ is the unit sphere metric.

The components of the metric in Bondi coordinates are then

$$g^{\mu\nu} = \frac{\partial x^\mu}{\partial \bar{x}^{\bar{\alpha}}} \frac{\partial x^\nu}{\partial \bar{x}^{\bar{\beta}}} g^{\bar{\alpha}\bar{\beta}}. \quad (2.34)$$

The Jacobians include the derivatives of the Bondi radius r . We compute

$$\begin{aligned} r_{,\lambda} &= \frac{r}{4} g^{\bar{A}\bar{B}} g_{\bar{A}\bar{B},\lambda}, \\ r_{,u} &= \frac{r}{4} g^{\bar{A}\bar{B}} g_{\bar{A}\bar{B},\bar{u}}. \end{aligned} \quad (2.35)$$

Since the only difference between the Bondi and intermediate coordinates is the choice of radinull coordinates, the Jacobians for the u , θ and ϕ directions are trivial. Eq. (2.32) gives us

$$\begin{aligned} g^{uu} &= g^{\bar{u}\bar{u}} = 0, \\ g^{uA} &= g^{\bar{u}\bar{A}} = 0, \\ g^{AB} &= g^{\bar{A}\bar{B}}. \end{aligned} \quad (2.36)$$

The other metric components are

$$\begin{aligned} g^{ur} &= \frac{\partial r}{\partial \bar{x}^{\bar{\mu}}} g^{\bar{u}\bar{\mu}} = -r_{,\lambda}, \\ g^{rr} &= \frac{\partial r}{\partial \bar{x}^{\bar{\mu}}} \frac{\partial r}{\partial \bar{x}^{\bar{\nu}}} g^{\bar{\mu}\bar{\nu}} = (r_{,\lambda})^2 g^{\lambda\lambda} + 2r_{,\lambda} (r_{,\bar{A}} g^{\lambda\bar{A}} - r_{,\bar{u}}) + r_{,\bar{A}} r_{,\bar{B}} g^{\bar{A}\bar{B}}, \\ g^{rA} &= \frac{\partial r}{\partial \bar{x}^{\bar{\mu}}} g^{\bar{A}\bar{\mu}} = r_{,\lambda} g^{\lambda\bar{A}} + r_{,\bar{B}} g^{\bar{A}\bar{B}}. \end{aligned} \quad (2.37)$$

Because u and x^A are equal to \check{t} and $\check{x}^{\bar{A}}$ on the world tube and are constant along outgoing null geodesics, the time and angular coordinates $(\check{t}, \check{x}^{\bar{A}})$ on the world tube determine the coordinates u and x^A throughout the characteristic region, including on \mathcal{S}^+ . Thus, the coordinates at \mathcal{S}^+ will be gauge-dependent, since \check{t} and $\check{x}^{\bar{A}}$ are dependent upon the gauge choices made in the 3+1 Cauchy evolution. We will later eliminate this gauge dependence by evolving and transforming to the coordinates of free-falling observers on \mathcal{S}^+ , as described below in Sec. 2.5.

Inner Boundary Values of Characteristic Variables

Now that we have the full Bondi metric, we assemble the inner boundary values for the various evolution variables used in the volume, J, β, Q, U, W , and H . We write out the complex dyads as

$$q_A = (-1, -i \sin \theta),$$

$$q^A = \left(-1, -\frac{i}{\sin \theta} \right). \quad (2.38)$$

Now because these complex dyads form the basis of the unit sphere metric q_{AB} , and because q_{AB} is independent of time and radius, along each ray these dyads are constant, thus $q_{A,\lambda} = q^A_{,\lambda} = 0$.

Inverting the metric in Eq. (2.1),

$$g^{\mu\nu} = \begin{bmatrix} 0 & -e^{-2\beta} & 0^A \\ -e^{-2\beta} & (1+rW)e^{-2\beta} & -e^{-2\beta}U^A \\ 0^B & -e^{-2\beta}U^B & r^{-2}h^{AB} \end{bmatrix}, \quad (2.39)$$

where $h_{AB}h^{BC} = \delta_A^C$ and $|h_{AB}| = |q_{AB}|$.

In the PittNull code, the quantities J , β , Q , U , and W and their λ derivatives are computed on the worldtube, and then J , β , Q , U , and W are extrapolated off the worldtube onto a surface of constant Bondi radius r [36]. PittNull then chooses its internal compactified radinull coordinates in the characteristic region to be surfaces of constant r .

However, in Ref. [87] and here, we avoid extrapolation, and we instead choose the worldtube to be at a constant value of our compactified radial coordinate ρ ,

$$\rho = \frac{r}{R+r} \quad (2.40)$$

where $R(u, x^A) = r_{|\Gamma}$ is the Bondi radius (Eq. (2.33)) of the world tube,

$$R = r_{|\Gamma} \quad (2.41)$$

Note that R depends on u and x^A and that ρ runs from $\rho_{|\Gamma} = 1/2$ to $\rho_{|\mathcal{I}^+} = 1$. Because of our choice of compactified radinull coordinate, R and its derivatives evaluated on the world tube (Eq. (2.35)),

$$R_{,\lambda} = r_{,\lambda|\Gamma}, \quad (2.42)$$

$$R_{,u} = r_{,u|\Gamma}, \quad (2.43)$$

will appear in our equations, and we need to carefully distinguish between derivatives with respect to u or x^A at a constant value of r (which appear in Eqs. (2.14)–(2.18)), and derivatives with respect to u or x^A at a constant value of ρ (which appear, e.g., in Eq. (2.43)).

We can now write down the inner boundary values of the characteristic variables in terms of the metric coefficients that we have computed at the inner boundary. Going back to the definition of $J = \frac{1}{2}q^A q^B h_{AB}$, we get the expressions

$$J_{|\Gamma} = \frac{1}{2R^2} q^A q^B g_{AB}, \quad (2.44)$$

$$K_{|\Gamma} = \sqrt{1 + J_{|\Gamma} \bar{J}_{|\Gamma}}, \quad (2.45)$$

$$J_{,\lambda|\Gamma} = \frac{1}{2R^2} q^A q^B g_{AB,\lambda} - \frac{2R_{,\lambda}}{R} J_{|\Gamma}. \quad (2.46)$$

We can read off the value for g^{ur} to compute β ,

$$\beta_{|\Gamma} = -\frac{1}{2} \ln(R, \lambda). \quad (2.47)$$

We will also need $\beta_{,\lambda|\Gamma}$ in order to compute $Q_{|\Gamma}$. Directly differentiating Eq. (2.47) yields

$$\beta_{,\lambda|\Gamma} = -\frac{R_{,\lambda\lambda}}{2R_{,\lambda}}, \quad (2.48)$$

but this involves the quantity $R_{,\lambda\lambda}$, which appears to depend on second derivatives of the metric. So we instead compute $\beta_{,\lambda|\Gamma}$ using β 's evolution equation, Eq. (2.154):

$$\beta_{,\lambda|\Gamma} = \frac{R}{8R_{,\lambda}} \left(J_{,\lambda|\Gamma} \bar{J}_{,\lambda|\Gamma} - (K_{,\lambda|\Gamma})^2 \right), \quad (2.49)$$

which involves only first derivatives.

The quantities U and W can similarly be read off from the metric:

$$U_{|\Gamma} = \frac{g^{rA}}{g^{ur}} q_A, \quad (2.50)$$

$$W_{|\Gamma} = \frac{1}{R} \left(-\frac{g^{rr}}{g^{ur}} - 1 \right). \quad (2.51)$$

To get $Q_{|\Gamma}$, we will also need $U_{,\lambda|\Gamma}$, which we compute by differentiating the expression for $U_{|\Gamma}$ and using Eq. (2.48) to eliminate $R_{,\lambda\lambda}$ in favor of $\beta_{,\lambda|\Gamma}$:

$$U_{,\lambda|\Gamma} = - \left(g^{\lambda\bar{A}}_{,\lambda} + \frac{R_{,\lambda\bar{B}}}{R_{,\lambda}} g^{\bar{A}\bar{B}} + \frac{R_{,\bar{B}}}{R_{,\lambda}} g^{\bar{A}\bar{B}} \right) q_{\bar{A}} + 2\beta_{,\lambda|\Gamma} \left(U_{|\Gamma} + g^{\lambda\bar{A}} q_{\bar{A}} \right), \quad (2.52)$$

where it is understood that $\beta_{,\lambda|\Gamma}$ is to be evaluated using Eq. (2.49). Now that we have an expression for $U_{,\lambda|\Gamma}$, the inner boundary value of Q is given by

$$Q_{|\Gamma} = R^2 \left(J_{|\Gamma} \bar{U}_{,\lambda|\Gamma} + K_{|\Gamma} U_{,\lambda|\Gamma} \right). \quad (2.53)$$

The last quantity that we will need on the inner boundary is $H = J_{,u|_{r=\text{const}}}$. However, since the worldtube Γ is not a surface of constant r , we must take care how we compute our u -derivatives. In particular, differentiating Eq. (2.44) on the world tube gives us

$$J_{,u|\Gamma} = \frac{1}{2R^2} q^A q^B g_{AB,u} - \frac{2R_{,u}}{R} J_{|\Gamma}, \quad (2.54)$$

where all u -derivatives are taken on the worldtube rather than holding r fixed.

Note that the world tube is a surface of constant ρ , our compactified radial coordinate. We introduce one last intermediate variable $\Phi = J_{,u|\rho=\text{const}}$, so we can write Eq. (2.54) as

$$\Phi_{|\Gamma} = \frac{1}{2R^2} q^A q^B g_{AB,u} - \frac{2R_{,u}}{R} J_{|\Gamma}. \quad (2.55)$$

Note that if the world tube is located at a fixed value of \check{r} , as we assume here, the derivatives $g_{AB,u}$ and $R_{,u}$ can be taken at constant \check{r} . Instead, if the world tube is allowed to move freely (within the Cauchy $\check{x}^{\check{\alpha}}$ coordinate system), then an additional correction factor depending on the worldtube's coordinate velocity will be necessary to convert $g_{AB,u}|_{\check{r}=\text{const}}$ and $R_{,u}|_{\check{r}=\text{const}}$ to $g_{AB,u}|_{\Gamma}$ and $R_{,u}|_{\Gamma}$.

To compute H in terms of Φ we use Eq. (2.40):

$$H = \Phi - \rho(1 - \rho) \frac{R_{,u}}{R} J_{,\rho}. \quad (2.56)$$

This formula will appear again in the volume evolution; see Sec 2.4. Since we have already computed $J_{,\lambda}$ in Eq. (2.46), we convert $J_{,\rho}$ to $J_{,\lambda}$,

$$J_{,\rho} = \frac{\partial r}{\partial \rho} \frac{\partial \lambda}{\partial r} J_{,\lambda} = \frac{R}{(1 - \rho)^2} \frac{1}{r_{,\lambda}} J_{,\lambda}. \quad (2.57)$$

After substituting this into Eq. (2.56) and evaluating at the inner boundary ($\rho = 1/2$), the formula for the inner boundary value of H is

$$H|_{\Gamma} = \Phi|_{\Gamma} - \frac{R_{,u}}{R_{,\lambda}} J_{,\lambda}|_{\Gamma}. \quad (2.58)$$

Right now the information flow for the inner boundary formalism is entirely outgoing. That is, information from the interior spacetime feeds into the CCE evolution, yet the CCE evolution does not feed back into the interior spacetime. An extension of CCE, called Cauchy-Characteristic Matching (CCM) [36] involves converting from the Bondi metric back into the world tube metric, coupling the information from the volume evolution back into the interior spacetime, effectively providing solutions to the boundary condition on the interior spacetime which fully satisfies the Einstein equations. While a previous code has successfully performed CCM in the linearized case, they were unable to stably run it for the general case [146]. Future work on our code will attempt to implement CCM in our code so that we can fully couple it to the evolution of the interior spacetime and bypass the need for separate boundary conditions for the Cauchy codes.

Computational Domain

We implement angular basis functions through the use of the external code packages `Spherepack` [15, 55], which can handle standard spherical harmonics, and `Spinsfast` [100], which is capable of handling SWSHes. The world tube metric data and most of the intermediate quantities of the inner boundary formalism are real, tensoral metric quantities (i.e. representable by the typical spherical harmonics), so we use `Spherepack`. Once all of the inner boundary values of the Bondi evolution quantities are computed, they are then projected onto the basis utilized by `Spinsfast` for use during the volume evolution. Because Cauchy codes evaluate the world tube data at discrete time slices, we use cubic interpolation to evaluate each of the metric quantities at arbitrary time values.

2.4 Volume Evolution

Computational Domain

Because the domain of CCE extends all of the way out to \mathcal{S}^+ where the Bondi radius is infinite, to express \mathcal{S}^+ on a finite computational domain, we define a compactified coordinate, ρ , in Eq. (2.40). This choice of compactification is subtly different from that which is used in PittNull [135]. Because they extrapolate quantities on the worldtube onto a hypersurface of constant Bondi radius, their compactification parameter is constant and unchanging during their entire evolution. By tying our compactification parameter to a fixed coordinate radius \check{r} and allowing the Bondi radius to change freely, we must be careful in how we define our derivatives.

One consequence of utilizing ρ is that angular derivatives computed numerically on our grid, $\delta_{|\rho}$, are at a constant value of ρ , so these are not the same as angular derivatives defined on surfaces of constant r , which we denote as $\bar{\delta}$. Since Eqs. (2.14)–(2.18) involve $\bar{\delta}$ and not $\delta_{|\rho}$, we must apply a correction factor to compute $\bar{\delta}$ from $\delta_{|\rho}$:

$$\bar{\delta}F = \delta_{|\rho}F - F_{,\rho}\delta_{|\rho}\rho = \delta_{|\rho}F - F_{,\rho}\frac{\rho(1-\rho)}{R}\delta_{|\rho}R, \quad (2.59)$$

for an arbitrary quantity F . Similar correction factors are needed for second derivatives that appear in the evolution equations:

$$\bar{\delta}F_{,\rho} = \delta_{|\rho}F_{,\rho} - F_{,\rho}\frac{1-2\rho}{R}\delta_{|\rho}R - F_{,\rho\rho}\frac{\rho(1-\rho)}{R}\delta_{|\rho}R, \quad (2.60)$$

$$\begin{aligned} \bar{\delta}\bar{\delta}F &= \bar{\delta}_{|\rho}\delta_{|\rho}F + F_{,\rho}\left(\frac{\rho(1-\rho)}{R^2}\right)\left(2(1-\rho)\bar{\delta}_{|\rho}R\delta_{|\rho}R - R\bar{\delta}_{|\rho}\delta_{|\rho}R\right) - \delta_{|\rho}F_{,\rho}\left(\frac{\rho(1-\rho)}{R}\bar{\delta}_{|\rho}R\right) \\ &\quad - \bar{\delta}_{|\rho}F_{,\rho}\left(\frac{\rho(1-\rho)}{R}\delta_{|\rho}R\right) + F_{,\rho\rho}\left(\frac{\rho(1-\rho)}{R}\right)^2\bar{\delta}_{|\rho}R\delta_{|\rho}R. \end{aligned} \quad (2.61)$$

Correction factors for $\bar{\delta}F$, $\bar{\delta}F_{,\rho}$, $\bar{\delta}\bar{\delta}F$, $\bar{\delta}\bar{\delta}F$, and $\bar{\delta}\bar{\delta}\bar{\delta}F$ are obtained by appropriately interchanging $\bar{\delta}$ and $\bar{\delta}$ in Eqs. (2.59)–(2.61).

Numerical derivatives with respect to t and u are also taken at constant ρ on our grid, but at constant r in the equations, so similar correction factors are required there as well, as discussed below in Sec. 2.4.

We employ computational grid meshes suitable for spectral methods, Chebyshev-Gauss-Lobatto for the radial direction and Spinsfast mesh for the angular directions.

Initial Data Slice

The characteristic evolution equations require boundary data on two boundaries: the worldtube (thick red curve in Fig. 2.1) and an initial slice $u = u_0$ (thick blue curve in Fig. 2.1). Boundary values on the worldtube were treated in Sec. 2.3 above; here we discuss values on the initial slice. Given the hierarchical nature of the evolution equations, the only piece of the metric we need to specify on the initial slice is J , as we can compute all of the other evolution quantities from J using Eqs. (2.14)–(2.18). The main mathematical consideration for choosing J for the initial slice

is ensuring the regularity of J at \mathcal{I}^+ ; the main physical consideration in typical applications is choosing a J that corresponds to no incoming radiation [21, 37].

We choose a piecewise function that takes the inner boundary value $J|_{\Gamma}$ and rolls it to $J|_{\mathcal{I}^+} = 0$ so that J on the initial slice is smooth through second radinull derivatives,

$$J = j_0(\rho)J|_{\Gamma},$$

$$j_0(\rho) = \begin{cases} 1, & \rho \leq \rho_0, \\ 10X_\rho^3 - 15X_\rho^4 + 6X_\rho^5, & \rho_0 \leq \rho \leq \rho_1, \\ 0, & \rho \geq \rho_1, \end{cases}$$

$$X_\rho = \frac{\rho_1}{-\rho_0 + \rho_1} - \frac{1}{-\rho_0 + \rho_1}\rho \quad (2.62)$$

where X_ρ has been chosen so that $X_\rho(\rho_0) = 1$ and $X_\rho(\rho_1) = 0$, and the polynomial $j_0(\rho)$ is determined by matching conditions at the interface of the piecewise function. Thus, J is second order smooth everywhere on the initial slice. We have currently set the bounds of this rolloff function as $(\rho_0, \rho_1) = (.55, .95)$.

Radinull Integration

The characteristic equations Eqs. (2.14)–(2.18) can be solved in sequence by integration in r from the worldtube to \mathcal{I}^+ . We use a numerical radinull grid in the compactified variable ρ , and we re-express the characteristic equations in terms of ρ derivatives; see Eqs. (2.154)–(2.159). The grid points in ρ are chosen at Chebyshev-Gauss-Lobatto quadrature points. The radinull equations for $\beta_{,\rho}$ and $U_{,\rho}$ (Eq. (2.154), (2.156)) both lend themselves to straightforward Chebyshev-Gauss-Lobatto quadrature. Starting at the inner boundary values of $\beta|_{\Gamma}$ (Eq. (2.47)) and $U|_{\Gamma}$ (Eq. (2.51)), these evolution variables are integrated out to \mathcal{I}^+ .

A quick examination of the radinull equations for the evolution quantities $Q_{,\rho}$, $W_{,\rho}$, and $H_{,\rho}$ (Eq. (2.155), (2.158), (2.159)) reveals powers of $(\rho - 1)$ in denominators, so care must be taken to maintain regularity at \mathcal{I}^+ (where $\rho = 1$). A previous version of this same spectral CCE method [87] utilized integration by parts in order to rewrite the equations in a form without poles, allowing them to be integrated directly via Chebyshev-Gauss-Lobatto quadrature. However, integration by parts introduced logarithmic terms like $\log(1 - \rho)$ which canceled analytically in the final expressions but which were not well represented by a Chebyshev-Gauss-Lobatto spectral expansion in ρ . These logarithmic terms spoiled exponential convergence and led to a large noise floor, limiting the accuracy of the method. We choose an alternative approach here.

The evolution equation for Q , Eq. (2.155), can be written in the form

$$(r^2 Q)_{,\rho} = \frac{Q_C}{(1 - \rho)^2} + \frac{Q_D}{(1 - \rho)^3}, \quad (2.63)$$

where Q_C corresponds to the $1/(1 - \rho)^2$ term and Q_D is the $1/(1 - \rho)^3$ term in Eq. (2.155), and all factors of $(1 - \rho)$ in denominators have been written explicitly.

To better characterize the asymptotic behavior of this equation, we rewrite the system in terms of the inverse radinull coordinate $x = R/r = 1/\rho - 1$. Then Eq. (2.63) becomes

$$\left(\frac{Q}{x^2}\right)_{,x} = \frac{C}{x^2} + \frac{D}{x^3}, \quad (2.64)$$

where

$$C = -\frac{Q_C + Q_D}{R^2}, \quad (2.65)$$

$$D = -\frac{Q_D}{R^2}. \quad (2.66)$$

We know the right-hand side quantities C and D are regular at $x = 0$, and we seek a solution Q that is also regular there. So we introduce new variables, motivated by Taylor series expansions of Q , C , and D about \mathcal{I}^+ ($x = 0$),

$$Q = Q - Q|_{\mathcal{I}^+} - xQ_{,x}|_{\mathcal{I}^+}, \quad (2.67)$$

$$C = C - C|_{\mathcal{I}^+} - xC_{,x}|_{\mathcal{I}^+}, \quad (2.68)$$

$$D = D - D|_{\mathcal{I}^+} - xD_{,x}|_{\mathcal{I}^+} - \frac{x^2}{2}D_{,xx}|_{\mathcal{I}^+}. \quad (2.69)$$

Thus, by construction, Q and C are both guaranteed to behave like x^2 near $x = 0$ while D behaves as x^3 . Substituting these variables into Eq. (2.64) and gathering like terms, we find the differential equation

$$\left(\frac{Q}{x^2}\right)_{,x} = \frac{C}{x^2} + \frac{D}{x^3} + \frac{2C_{,x}|_{\mathcal{I}^+} + D_{,xx}|_{\mathcal{I}^+}}{2x} + \frac{Q_{,x}|_{\mathcal{I}^+} + C|_{\mathcal{I}^+} + D_{,x}|_{\mathcal{I}^+}}{x^2} + \frac{2Q|_{\mathcal{I}^+} + D|_{\mathcal{I}^+}}{x^3}. \quad (2.70)$$

Because of how we have defined Q , C and D , any potential singularity issues are confined to the last three terms. To satisfy Eq. (2.70) for all x , the numerators of each of these terms must identically vanish, providing constraints and boundary conditions on the asymptotic values of Q , C , and D ,

$$Q|_{\mathcal{I}^+} = -\frac{D|_{\mathcal{I}^+}}{2}, \quad (2.71)$$

$$Q_{,x}|_{\mathcal{I}^+} = -C|_{\mathcal{I}^+} - D_{,x}|_{\mathcal{I}^+}, \quad (2.72)$$

$$0 = -C_{,x}|_{\mathcal{I}^+} - \frac{1}{2}D_{,xx}|_{\mathcal{I}^+}. \quad (2.73)$$

The last equation, Eq. (2.73) is a regularity condition on C and D . It turns out that this condition is guaranteed to be satisfied if $J = 0$ and $J_{,xx} = 0$ at \mathcal{I}^+ .

We now integrate the equation

$$\left(\frac{Q}{x^2}\right)_{,x} = \frac{C}{x^2} + \frac{D}{x^3} \quad (2.74)$$

with inner boundary value

$$Q|_{\Gamma} = Q|_{\Gamma} + \frac{D|_{\mathcal{I}^+}}{2} + (C|_{\mathcal{I}^+} + D_{,x}|_{\mathcal{I}^+}) \quad (2.75)$$

to obtain Q at all radinull points. Then we reconstruct Q by adding back in its asymptotic values,

$$Q = \mathcal{Q} - \frac{D_{|\mathcal{I}^+}}{2} - x (C_{|\mathcal{I}^+} + D_{x|\mathcal{I}^+}). \quad (2.76)$$

Because the equation for Q does not mix the real and imaginary parts of Q , we follow [87] and solve for real and imaginary parts of Q separately.

Examining the evolution equation for W , Eq. (2.158), we recognize that it has the same form as the equation for Q , Eq. (2.155). Therefore, in order to solve for W , we use the same procedure as we do for Q , following from Eq. (2.63) through Eq. (2.76) but replacing all of quantities specific to Q with their W equivalents.

The radinull equation for H , Eq. (2.159) can be written as

$$(rH)_{,\rho} - rJ(H\bar{T} - \bar{H}T) = H_A + \frac{H_B}{1-\rho} + \frac{H_C}{(1-\rho)^2}, \quad (2.77)$$

where $H_B = \Sigma_i H_{Bi}$. The form of this equation is very similar to that of Eq. (2.63) that governs the Q (and W) radinull evolution. However, there is now the additional complication of whereby $H_{,\rho}$ has a term proportional to not only H , but also to \bar{H} . This couples the real and imaginary parts of the equation.

The previous version of this code employed the Magnus expansion in order to handle this difficulty [87]. While the Magnus expansion might be useful for systems where the terms in its expansion are rapidly shrinking, there is no guarantee that will hold in general. Instead, we will write the system as a matrix differential equation, expressing H (and H_A, H_B , and H_C) as column vectors like

$$H = \begin{pmatrix} \Re(H) \\ \Im(H) \end{pmatrix}, \quad (2.78)$$

and defining the quantity M as

$$M \equiv \begin{pmatrix} \Re(J)\Re(T) & \Re(J)\Im(T) \\ \Im(J)\Re(T) & \Im(J)\Im(T) \end{pmatrix}, \quad (2.79)$$

so that MH here represents matrix multiplication. Then Eq.(2.77) becomes the matrix equation,

$$(rH)_{,\rho} - rMH = H_A + \frac{H_B}{1-\rho} + \frac{H_C}{(1-\rho)^2}, \quad (2.80)$$

As before, we convert from ρ into the inverse radinull coordinate $x = R/r = 1/\rho - 1$ to better characterize its behavior near \mathcal{I}^+ ,

$$\left(\frac{H}{x}\right)_{,x} + \mathcal{M}\frac{H}{x} = A + \frac{B}{x} + \frac{C}{x^2} \quad (2.81)$$

where

$$\mathcal{M} = \frac{M}{(1+x)^2}, \quad (2.82)$$

$$A = -\frac{H_A}{R(1+x)^2}, \quad (2.83)$$

$$B = -\frac{H_B}{R(1+x)}, \quad (2.84)$$

$$C = -\frac{H_C}{R}. \quad (2.85)$$

As we did with the Q equation, we shall introduce one final set of variables, motivated by Taylor series expansions of H, B , and C about $x = 0$.

$$\mathcal{H} = H - H|_{\mathcal{S}^+}, \quad (2.86)$$

$$\mathcal{B} = B - B|_{\mathcal{S}^+} - \mathcal{M}H|_{\mathcal{S}^+} + \mathcal{M}|_{\mathcal{S}^+}H|_{\mathcal{S}^+}, \quad (2.87)$$

$$C = C - C|_{\mathcal{S}^+} - xC_{,x}|_{\mathcal{S}^+}. \quad (2.88)$$

Once again, these variables are constructed so that \mathcal{H} and \mathcal{B} behave as x and C behaves as x^2 in a neighborhood about $x = 0$. Substituting these into Eq. (2.81), we get

$$\left(\frac{\mathcal{H}}{x}\right)_{,x} + \mathcal{M}\frac{\mathcal{H}}{x} = A + \frac{\mathcal{B}}{x} + \frac{C}{x^2} + \frac{H|_{\mathcal{S}^+} + C|_{\mathcal{S}^+}}{x^2} + \frac{B|_{\mathcal{S}^+} + C_{,x}|_{\mathcal{S}^+} - \mathcal{M}|_{\mathcal{S}^+}H|_{\mathcal{S}^+}}{x} \quad (2.89)$$

As before, the numerators of the last two terms must vanish, which gives us a boundary condition on H at \mathcal{S}^+ ,

$$H|_{\mathcal{S}^+} = -C|_{\mathcal{S}^+}, \quad (2.90)$$

and a boundary constraint on B, C , and \mathcal{M} ,

$$0 = B|_{\mathcal{S}^+} + C_{,x}|_{\mathcal{S}^+} + \mathcal{M}|_{\mathcal{S}^+}C|_{\mathcal{S}^+}. \quad (2.91)$$

The last constraint is a regularity condition that is guaranteed to be satisfied if $J = 0$ and $J_{,xx} = 0$ at \mathcal{S}^+ . We then integrate the equation

$$\left(\frac{\mathcal{H}}{x}\right)_{,x} + \mathcal{M}\frac{\mathcal{H}}{x} = A + \frac{\mathcal{B}}{x} + \frac{C}{x^2} \quad (2.92)$$

from the worldtube to \mathcal{S}^+ , with boundary value $\mathcal{H}|_{\Gamma} = H|_{\Gamma} + C|_{\mathcal{S}^+}$, to obtain \mathcal{H} on the entire null slice. We reconstruct H by computing

$$H = \mathcal{H} - C|_{\mathcal{S}^+}. \quad (2.93)$$

To help ensure the stability of the system, we perform spectral filtering for each of the evolution quantities J, β, Q, U, W , and H after every time we compute them, similar to [87]. For the angular filtering, we set to 0 the highest two ℓ -modes in the spectral decomposition on each shell of constant ρ . Thus, resolving the system up through ℓ_{max} modes requires storing and evolving the evolution quantities in the volume up through $\ell = \ell_{max} + 2$ modes. We filter along the radinull direction by taking the spectral expansion of the evolution quantities along each null ray and scaling the i -th coefficient by

$$e^{-108(i/(n_\rho-1))^{16}}, \quad (2.94)$$

where n_ρ is the number of radinull points.

Time Evolution

To evolve J forward in time, we integrate

$$J_{,u}|_{\rho=\text{const}} = \Phi \quad (2.95)$$

at each radiull point using the method of lines. This is done using an ODE integrator, integrating forward in u , with a supplied right-hand-side Φ . Here Φ is computed using

$$\Phi = H + \rho(1 - \rho) \frac{J_{,\rho}}{R} R_{,u}, \quad (2.96)$$

(see Eq. (2.56)), where H is the result of the radiull integration, Eq. (2.18), accomplished using the method in Section 2.4.

The time integration of J (Eq. (2.95)) uses a 5th order Dormand-Prince ODE solver with adaptive timestepping [126], and a default relative error tolerance of 10^{-8} except where otherwise noted. Because this is a characteristic evolution, where each time step corresponds to a lightlike rather than spacelike slicing, there is no CFL condition on the size of the time steps. Thus, the step sizes are limited entirely by the error measure. The time evolution is also done in tandem with the evolution of the inertial coordinates (Eqs. (2.123)–(2.125)), and of the conformal factor (Eq. (2.107)) from scri extraction, as described below.

2.5 Scri Extraction

Once the characteristic equations have been solved in the volume so that the Bondi metric variables are known on \mathcal{S}^+ , the gravitational waveform can be computed. This involves two steps. The first step is computing the Bondi News function at \mathcal{S}^+ from the metric variables there. The second step involves transforming the News to a freely-falling coordinate system at \mathcal{S}^+ ; this removes all remaining gauge freedom up to a BMS transformation. These steps are described below.

News Function

The Bondi metric given in Eq. (2.1) is divergent at \mathcal{S}^+ where $r \rightarrow \infty$, so we work with a conformally-rescaled Bondi metric, $\hat{g}_{\mu\nu} = \ell^2 g_{\mu\nu}$, where $\ell = 1/r$, that is finite at $r \rightarrow \infty$ and which takes the form [35]

$$\hat{g}_{\mu\nu} = - \left(e^{2\beta} (\ell^2 + \ell W) - h_{AB} U^A U^B \right) du^2 + 2e^{2\beta} dud\ell - 2h_{AB} U^B dudx^A + h_{AB} dx^A dx^B. \quad (2.97)$$

Here h_{AB} , β , W , and U^A are the same quantities that appear in Eq. (2.1).

To facilitate the computation of the News function, we construct an additional conformal metric

$$\tilde{g}_{\mu\nu} = \omega^2 \hat{g}_{\mu\nu}, \quad (2.98)$$

that is inertial and asymptotically Minkowski at \mathcal{S}^+ . The conformal factor ω is chosen so that the angular part of $\tilde{g}_{\mu\nu}$ is a unit sphere metric [149],

$$q_{AB} = \omega^2 h_{AB}|_{\mathcal{S}^+}. \quad (2.99)$$

In terms of the original metric,

$$\tilde{g}_{\mu\nu} = \Omega g_{\mu\nu}, \quad (2.100)$$

$$\Omega = \omega \ell. \quad (2.101)$$

On a given constant u slice, ω can be computed by solving an elliptic equation related to the 2D curvature scalar,

$$\mathcal{R} = 2 \left(\omega^2 + h_{|\mathcal{S}^+}^{AB} D_A D_B \ln \omega \right), \quad (2.102)$$

where D_A is the covariant derivative associated with $h_{|\mathcal{S}^+}^{AB}$. Expanding out the covariant derivatives yields [35],

$$\begin{aligned} h_{|\mathcal{S}^+}^{AB} D_A D_B \ln \omega = & \frac{1}{4} \left(-2\bar{\delta}^2 \ln \omega \bar{J} - 2\bar{\delta}^2 \ln \omega J + 4\bar{\delta}\bar{\delta} \ln \omega K - \bar{\delta} \ln \omega \bar{\delta} J \bar{J}^2 - \bar{\delta} \ln \omega \bar{\delta} \bar{J} J \bar{J} \right. \\ & - 2\bar{\delta} \ln \omega \bar{\delta} \bar{J} + 2\bar{\delta} \ln \omega \bar{\delta} K \bar{J} K + \bar{\delta} \ln \omega \bar{\delta} J \bar{J} K + \bar{\delta} \ln \omega \bar{\delta} \bar{J} J K - 2\bar{\delta} \ln \omega \bar{\delta} K J \bar{J} \\ & + \bar{\delta} J \bar{\delta} \ln \omega \bar{J} K + \bar{\delta} \bar{J} \bar{\delta} \ln \omega J K - 2\bar{\delta} K \bar{\delta} \ln \omega J \bar{J} - \bar{\delta} \ln \omega \bar{\delta} J J \bar{J} \\ & \left. - 2\bar{\delta} \ln \omega \bar{\delta} J - \bar{\delta} \ln \omega \bar{\delta} \bar{J} J^2 + 2\bar{\delta} \ln \omega \bar{\delta} K J K \right), \end{aligned} \quad (2.103)$$

Eq. (2.102) could in principle be used to solve for ω at each slice of constant u . However, we instead solve this equation for ω only on the initial slice, where the equation simplifies significantly (see below), and then we construct an evolution equation for ω and we evolve ω as a function of u . Note that when evolving ω , one could use Eq. (2.102) as a check to monitor the error in ω ; however we do not yet do so.

On the initial slice, Eqs. (2.102) and (2.103) simplify considerably; we have set $J_{|\mathcal{S}^+} = 0$ (see Eq. (2.62)), so Eq. (2.103) implies that $h_{|\mathcal{S}^+}^{AB} D_A D_B \ln \omega = 4\bar{\delta}\bar{\delta} \ln \omega$ and Eq. (2.19) implies that $\mathcal{R} = 2$, reducing Eq. (2.102) to $1 = \omega^2 + \bar{\delta}\bar{\delta} \ln \omega$. This has the trivial solution of $\omega = 1$.

To derive an evolution equation for ω , we instead turn to the generators at \mathcal{S}^+ [35],

$$\tilde{n}^\mu = \tilde{g}^{\mu\nu} \nabla_\nu \Omega_{|\mathcal{S}^+}, \quad (2.104)$$

$$\hat{n}^\mu = \hat{g}^{\mu\nu} \nabla_\nu \ell_{|\mathcal{S}^+} = \hat{g}^{\mu\ell}, \quad (2.105)$$

so that

$$\tilde{n}^\mu = \omega^{-1} \hat{n}^\mu. \quad (2.106)$$

Derivation for evolution of the conformal factor on \mathcal{S}^+ in the frame of the compactified metric, is given in Ref [35], and can be computed by,

$$2\hat{n}^\mu \nabla_\mu \ln \omega = -e^{-2\beta} W_{|\mathcal{S}^+}. \quad (2.107)$$

Ref [35] derived the formula for the News function in the conformal metric with the evolution coordinates, with a sign error corrected in [23] (Ref [35] chose their convention to agree with Bondi's

original expression in the axisymmetric case [54]). Here we've factored the s_i slightly differently then they did,

$$N = \frac{1}{16\omega A(K+1)} \left(4s_1 + 2s_2 + (\delta\bar{U} + \bar{\delta}U) s_3 - \frac{8}{\omega^2} s_4 + \frac{2}{\omega} s_5 \right), \quad (2.108)$$

$$A = \omega e^{2\beta}, \quad (2.109)$$

$$s_1 = J^2 \bar{H}_{,\ell} + J\bar{J}H_{,\ell} + 2(K+1)(H_{,\ell} - JK_{,u\ell}), \quad (2.110)$$

$$\begin{aligned} s_2 = & \delta J_{,\ell} J\bar{J}\bar{U} + \bar{\delta}\bar{J}_{,\ell} J^2\bar{U} + 2\delta U J\bar{J}K_{,\ell} + 2\delta\bar{U} J\bar{J}J_{,\ell} + \bar{\delta}J_{,\ell} J\bar{J}U + \bar{\delta}\bar{J}_{,\ell} J^2U + 2\bar{\delta}U J^2\bar{J}_{,\ell} + 2\bar{\delta}\bar{U} J^2K_{,\ell} \\ & + (K+1)(2\delta J_{,\ell}\bar{U} - 2\delta K_{,\ell}J\bar{U} - 2\delta U J\bar{J}_{,\ell} + 4\delta U K_{,\ell} - 2\delta\bar{U} JK_{,\ell} + 4\delta\bar{U} J_{,\ell} + 2\bar{\delta}J_{,\ell}U - 2\bar{\delta}K_{,\ell}JU \\ & - 2\bar{\delta}U JK_{,\ell} - 2\bar{\delta}\bar{U} J\bar{J}_{,\ell}), \end{aligned} \quad (2.111)$$

$$s_3 = J^2\bar{J}_{,\ell} + J\bar{J}J_{,\ell} + 2(K+1)(J_{,\ell} - JK_{,\ell}), \quad (2.112)$$

$$s_4 = \delta A\delta\omega J\bar{J} + \bar{\delta}A\bar{\delta}\omega J^2 + (K+1)(2\delta A\delta\omega - \delta A\bar{\delta}\omega J - \bar{\delta}A\delta\omega J), \quad (2.113)$$

$$\begin{aligned} s_5 = & 2\delta^2 AJ\bar{J} + 2\bar{\delta}^2 AJ^2 + \delta A\delta J\bar{J}J^2 + \delta A\bar{\delta}J^2\bar{J} - \delta A\bar{\delta}J\bar{J}K - \delta A\bar{\delta}J^2K + 2\bar{\delta}A\bar{\delta}K J^2\bar{J} \\ & + 2\bar{\delta}A\delta K J^2\bar{J} + \bar{\delta}A\bar{\delta}J^2\bar{J} + \bar{\delta}A\bar{\delta}J^3 - 2\bar{\delta}A\bar{\delta}K J^2K \\ & + (K+1)(4\delta^2 A - 4\bar{\delta}\delta AJ + 2\delta A\delta J\bar{J} + 2\delta A\bar{\delta}J\bar{J} - 4\delta A\delta K + 2\delta A\bar{\delta}J - 2\bar{\delta}A\delta J + 4\bar{\delta}A\delta K J) \\ & + (K+2)(-2\bar{\delta}A\delta K J\bar{J} - \bar{\delta}A\bar{\delta}J\bar{J}\bar{J} - \bar{\delta}A\bar{\delta}J^2). \end{aligned} \quad (2.114)$$

The news as defined in Eq. (2.108) has spin-weight +2. However, the usual convention for gravitational radiation is to work with quantities with spin-weight -2. Furthermore, the news N has the opposite sign as the usual convention. By relating the News function computed here to the News function from the more typical Newman-Penrose formalism [119] (see Ref [23], in particular the discussion of computing Ψ), we note that

$$N_{\text{N-P}} = -2\bar{N}_{\text{CCE}}, \quad (2.115)$$

where the quantity on the left is the usual definition and the quantity on the right is the one in Eq. (2.108).

Inertial Coordinates

Once the News function is computed according to Section 2.5, it is known as a function of coordinates (u, x^A) on \mathcal{I}^+ . Recall that these coordinates are chosen so that $u = \check{t}$ and $x^A = \check{x}^{\check{A}}$ on the world tube, where $(\check{t}, \check{x}^{\check{A}})$ are the time and angular coordinates of the interior Cauchy evolution. Therefore, the News as computed above depends on the choice of Cauchy coordinates.

In this section, we transform the News to a new inertial coordinate system $(\check{u}, \check{x}^{\check{A}})$ on \mathcal{I}^+ , where curves of constant $\check{x}^{\check{A}}$ correspond to worldlines of free-falling observers (because we are working on \mathcal{I}^+ , we can suppress the radinull coordinate). This removes the remaining gauge freedom in the News, up to a choice of free-falling observers (or in other words up to a BMS transformation).

On the initial slice, we choose $\tilde{u} = u$ and $\tilde{x}^{\tilde{A}} = x^A$. These inertial coordinates then evolve along the \mathcal{S}^+ generators [35],

$$\hat{n}^\mu \partial_\mu \tilde{u} = \omega, \quad (2.116)$$

$$\hat{n}^\mu \partial_\mu \tilde{x}^{\tilde{A}} = 0, \quad (2.117)$$

where the \hat{n}^μ are given by elements of the compactified metric according to Eq. (2.105).

Since $\tilde{x}^{\tilde{A}} = (\tilde{\theta}, \tilde{\phi})$ are not representable via a spectral expansion in spherical harmonics, thus making them poor choices for our numerics, we represent the inertial coordinates using a Cartesian basis $\tilde{x}^{\tilde{i}} = (\tilde{x}, \tilde{y}, \tilde{z})$. We reexpand Eq. (2.117), using the transformations,

$$\frac{\partial \tilde{\theta}}{\partial x^\mu} = \frac{1}{\tilde{x}^2 + \tilde{y}^2} \left(-\tilde{y} \frac{\partial \tilde{x}}{\partial x^\mu} + \tilde{x} \frac{\partial \tilde{y}}{\partial x^\mu} \right), \quad (2.118)$$

$$\frac{\partial \tilde{\phi}}{\partial x^\mu} = \frac{1}{\tilde{r}^2 \sqrt{\tilde{x}^2 + \tilde{y}^2}} \left(\tilde{x} \tilde{z} \frac{\partial \tilde{x}}{\partial x^\mu} + \tilde{y} \tilde{z} \frac{\partial \tilde{y}}{\partial x^\mu} - (\tilde{x}^2 + \tilde{y}^2) \frac{\partial \tilde{z}}{\partial x^\mu} \right). \quad (2.119)$$

Plugging those into Eq. (2.117) yields the coupled equations

$$-\tilde{y} \frac{\partial \tilde{x}}{\partial u} + \tilde{x} \frac{\partial \tilde{y}}{\partial u} = \frac{\hat{n}^\theta}{\hat{n}^u} \left(-\tilde{y} \frac{\partial \tilde{x}}{\partial \theta} + \tilde{x} \frac{\partial \tilde{y}}{\partial \theta} \right) + \frac{\hat{n}^\phi}{\hat{n}^u} \left(\frac{\partial}{\partial \theta} \rightarrow \frac{\partial}{\partial \phi} \right), \quad (2.120)$$

$$\tilde{x} \tilde{z} \frac{\partial \tilde{x}}{\partial u} + \tilde{y} \tilde{z} \frac{\partial \tilde{y}}{\partial u} - (\tilde{x}^2 + \tilde{y}^2) \frac{\partial \tilde{z}}{\partial u} = \frac{\hat{n}^\theta}{\hat{n}^u} \left(\tilde{x} \tilde{z} \frac{\partial \tilde{x}}{\partial \theta} + \tilde{y} \tilde{z} \frac{\partial \tilde{y}}{\partial \theta} - (\tilde{x}^2 + \tilde{y}^2) \frac{\partial \tilde{z}}{\partial \theta} \right) + \frac{\hat{n}^\phi}{\hat{n}^u} \left(\frac{\partial}{\partial \theta} \rightarrow \frac{\partial}{\partial \phi} \right). \quad (2.121)$$

By expanding the basis from 2 coordinates to 3, we also need to introduce a constraint which will force the $\tilde{x}^{\tilde{i}}$ to remain on the unit sphere and eliminate the extra degree of freedom, $\tilde{r} = \sqrt{\tilde{x}^2 + \tilde{y}^2 + \tilde{z}^2} = 1$. While this holds analytically, numerically \tilde{r} will shift away from 1 during the evolution, which makes it necessary to introduce a constraint equation to the system of equations,

$$\frac{\partial \tilde{r}}{\partial u} = \tilde{x} \frac{\partial \tilde{x}}{\partial u} + \tilde{y} \frac{\partial \tilde{y}}{\partial u} + \tilde{z} \frac{\partial \tilde{z}}{\partial u} = \tilde{r} C(\tilde{r}), \quad (2.122)$$

where $C(\tilde{r})$ is a constraint term where $C(\tilde{r} = 1) = 0$. In our code, $C(\tilde{r}) = -\kappa(\tilde{r} - 1)$ for some positive parameter κ .

With these three equations, Eqs. (2.120)–(2.122), we solve for the three $\frac{\partial \tilde{x}^{\tilde{i}}}{\partial u}$. After some manipulations and massaging, we obtain the evolution equations for the Cartesian inertial coordinates with respect to the characteristic coordinates,

$$\frac{\partial \tilde{x}}{\partial u} = \frac{\tilde{x}}{\tilde{r}} C(\tilde{r}) + \frac{1}{\tilde{r}^2} \left[\frac{\hat{n}^\theta}{\hat{n}^u} \left((\tilde{r}^2 - \tilde{x}^2) \frac{\partial \tilde{x}}{\partial \theta} - \tilde{x} \tilde{y} \frac{\partial \tilde{y}}{\partial \theta} - \tilde{x} \tilde{z} \frac{\partial \tilde{z}}{\partial \theta} \right) + \frac{\hat{n}^\phi}{\hat{n}^u} \left(\frac{\partial}{\partial \theta} \rightarrow \frac{\partial}{\partial \phi} \right) \right], \quad (2.123)$$

$$\frac{\partial \tilde{y}}{\partial u} = \frac{\tilde{y}}{\tilde{r}} C(\tilde{r}) + \frac{1}{\tilde{r}^2} \left[\frac{\hat{n}^\theta}{\hat{n}^u} \left(-\tilde{x} \tilde{y} \frac{\partial \tilde{x}}{\partial \theta} + (\tilde{r}^2 - \tilde{y}^2) \frac{\partial \tilde{y}}{\partial \theta} - \tilde{y} \tilde{z} \frac{\partial \tilde{z}}{\partial \theta} \right) + \frac{\hat{n}^\phi}{\hat{n}^u} \left(\frac{\partial}{\partial \theta} \rightarrow \frac{\partial}{\partial \phi} \right) \right], \quad (2.124)$$

$$\frac{\partial \tilde{z}}{\partial u} = \frac{\tilde{z}}{\tilde{r}} C(\tilde{r}) + \frac{1}{\tilde{r}^2} \left[\frac{\hat{n}^\theta}{\hat{n}^u} \left(-\tilde{x} \tilde{z} \frac{\partial \tilde{x}}{\partial \theta} - \tilde{y} \tilde{z} \frac{\partial \tilde{y}}{\partial \theta} + (\tilde{r}^2 - \tilde{z}^2) \frac{\partial \tilde{z}}{\partial \theta} \right) + \frac{\hat{n}^\phi}{\hat{n}^u} \left(\frac{\partial}{\partial \theta} \rightarrow \frac{\partial}{\partial \phi} \right) \right]. \quad (2.125)$$

Once we know $\tilde{u}(u, x^A)$, $\tilde{x}^{\tilde{i}}(u, x^A)$, then obtaining the News on this grid is a matter of interpolation. Our code does so in two steps. First, each of the spatial coordinates, as well as the News function

is interpolated in time onto slices of constant \tilde{u} , so that we then have both $\tilde{x}^{\tilde{i}}(\tilde{u}, x^A)$ and $N(\tilde{u}, x^A) = N(\tilde{u}, \tilde{x}^{\tilde{i}})$, using a cubic spline along each grid point on \mathcal{S}^+ .

Then on each constant \tilde{u} slice, we perform the spatial interpolation by projecting the News function onto its spectral coefficients $c^{\ell m}$, using the orthonormality of SWSHes from Eq. (2.153),

$$c^{\ell m}(\tilde{u}) = \int_{S^2} N(\tilde{u}, \tilde{x}^{\tilde{i}}) \overline{Y^{\ell m}}(\tilde{\theta}, \tilde{\phi}) \sin \tilde{\theta} d\tilde{\theta} d\tilde{\phi}. \quad (2.126)$$

However, since we numerically evaluate News function on the computational grid corresponding to the characteristic coordinates, we must instead do the integration over its area elements, $\sin \theta d\theta d\phi$, so we convert the coordinates of this expression, which introduces the determinant of a Jacobian,

$$d\tilde{\theta} d\tilde{\phi} = d\theta d\phi \left| \frac{\partial \tilde{x}^{\tilde{A}}}{\partial x^A} \right|. \quad (2.127)$$

Once again, because of the difficulties of representing angular coordinates spectrally, we convert this expression from $\tilde{\theta}$ and $\tilde{\phi}$ to $\tilde{x}^{\tilde{i}}$. To facilitate our expansion to Cartesian coordinates, we introduce a temporary radial coordinates \tilde{r} and r on the unit sphere with $\tilde{x}^{\tilde{A}} = (\tilde{r}, \tilde{\theta}, \tilde{\phi})$ and $x^A = (r, \theta, \phi)$ so that we can properly define the determinants (keeping in mind \tilde{r} and r are analytically identical to 1 so will disappear from the final expressions),

$$\left| \frac{\partial \tilde{x}^{\tilde{A}}}{\partial x^A} \right| = \left| \frac{\partial \tilde{x}^{\tilde{A}}}{\partial \tilde{x}^{\tilde{i}}} \right| \left| \frac{\partial \tilde{x}^{\tilde{i}}}{\partial x^A} \right| = \left(\frac{1}{\tilde{r}^2 \sin \tilde{\theta}} \right) \left| \frac{\partial \tilde{x}^{\tilde{i}}}{\partial x^A} \right|. \quad (2.128)$$

Plugging everything in yields the full expression,

$$c^{\ell m}(\tilde{u}) = \int_{S^2} N(\tilde{u}, \tilde{x}^{\tilde{i}}) \overline{Y^{\ell m}}(\tilde{\theta}, \tilde{\phi}) \frac{1}{\sin \theta} \left| \frac{\partial \tilde{x}^{\tilde{i}}}{\partial x^A} \right| \sin \theta d\theta d\phi. \quad (2.129)$$

Note that we have included a factor of $\sin \theta / \sin \theta$ which, while analytically trivial, aids with the numerics of our code. Incorporating the $\sin \theta$ in the numerator generates the proper spherical area element for the integration, while we factor the $1 / \sin \theta$ into the $\frac{\partial}{\partial \phi}$ terms in the Jacobian, as numerically computed spherical gradients return factors of $\frac{1}{\sin \theta} \frac{\partial}{\partial \phi}$.

If we want to convert these coefficients to the convention consistent with the Newman-Penrose notation, we must apply one last change according to Eq. (2.115),

$$c_{\text{N-P}}^{\ell m} = 2(-1)^{1-m} \overline{c_{\text{CCE}}^{\ell-m}}. \quad (2.130)$$

One potential issue with Eq. (2.129) is the possibility that there is a significant drift in the inertial coordinates relative to the code coordinates. If there is a large systematic shift in the coordinates (for example, if they all drift towards a single sky location), then there could be regions on the unit sphere which are sparsely represented. Because spectral methods of computing integrals often assume an optimal distribution of grid points across the surface, this drift means there is a risk of underresolving the computation Eq. (2.129), especially for high ℓ modes. To forestall this issue,

we have taken to representing the scri extraction portion at a significantly higher angular resolution from the rest of our code. In particular, when we properly resolve the volume evolution up to ℓ_{max} angular modes, the use maintain a basis consisting of $2\ell_{max}$ angular modes for our scri extraction code. Our properly resolved information content is still no better than what is resolved in the volume evolution (i.e. ℓ_{max}), but this allows us to accurately project onto the inertial coordinates with Eq. (2.129). Because the scri extraction portion of the code is only a 2D surface, this choice is an insignificant contribution to the overall computational cost of our code.

While this coordinate evolution projects the News function on an inertial frame, it is not a unique inertial frame. The class of inertial observers at \mathcal{I}^+ are all related to each other by the group of BMS transformations. Because our CCE inertial coordinates at \mathcal{I}^+ correspond to free falling observers, the BMS frame remains constant throughout the entire characteristic evolution. Thus, the BMS frame we use in our evolution is frozen in entirely by our choice to identify our inertial coordinates with the characteristic coordinates on our initial slice (i.e. $\tilde{u} = u$ and $\tilde{x}^{\tilde{A}} = x^A$). This choice is in some sense arbitrary, as it is ultimately related to the coordinates provided on the world tube by the Cauchy evolution on that initial slice, and there no guarentee of consistency between CCE evolutions on different world tubes even from the same Cauchy evolution. However, development of a consistent treatment of handing the choice of BMS frame is beyond the scope of this paper.

Computational Grid

We use `Spherepack` for most of the Scri Extraction, with the final projection onto the inertial coordinates done using `Spinsfast`. The time evolution of the inertial coordinates, Eqs. (2.123)–(2.125), and of the conformal factor, Eq. (2.107), is done in tandem with the evolution of J , Eq. (2.96), in the Volume Extraction, using the same routine (5th order Dormand-Prince) and error tolerance as specified for that evolution.

2.6 Code Tests

In order to showcase the accuracy, speed, and robustness of this spectral CCE code, we perform a number of tests on the code. We have two linearized solutions, a trival analytic solution, and two fully nonlinear tests which outline how well the code can remove purely coordinate effects from the News output.

Linearized Analytic Solution

The linearized form for the Bondi-Sachs metric for a shell of outgoing perturbations on a Minkowski background was given in [38], though our choice of notation follows more closely with that used in [136]. We can express the solutions in terms of the metric quantities

$$\begin{aligned} J_{lin} &= \sqrt{(\ell+2)!/(\ell-2)!} {}^2 Z^{\ell m} \mathfrak{R} \left(J_{\ell}(r) e^{i\nu u} \right), \\ U_{lin} &= \sqrt{\ell(\ell+1)} {}^1 Z^{\ell m} \mathfrak{R} \left(U_{\ell}(r) e^{i\nu u} \right), \\ \beta_{lin} &= {}^0 Z^{\ell m} \mathfrak{R} \left(\beta_{\ell}(r) e^{i\nu u} \right), \end{aligned}$$

$$W_{lin} = {}^0Z^{\ell m} \Re \left(W_{\ell}(r) e^{iv u} \right), \quad (2.131)$$

where ν is a real constant setting the frequency of the perturbations and $J_{\ell}(r), U_{\ell}(r), \beta_{\ell}(r)$ and $W_{\ell}(r)$ are all analytic complex functions of just the radius and ℓ -mode of the perturbation, given below. The angular content is expressed through the various ${}^sZ^{\ell m}$, which are just linear combinations of the typical SWSHes defined as in [38]

$$\begin{aligned} {}^sZ^{\ell m} &= \frac{1}{\sqrt{2}} \left({}^sY^{\ell m} + (-1)^m {}^sY^{\ell - m} \right) && \text{for } m > 0, \\ {}^sZ^{\ell m} &= \frac{i}{\sqrt{2}} \left((-1)^m {}^sY^{\ell m} - {}^sY^{\ell - m} \right) && \text{for } m < 0, \\ {}^sZ^{\ell 0} &= {}^sY^{\ell 0}. \end{aligned} \quad (2.132)$$

To get the linearized expression for H_{lin} , we can simply take a direct u derivative of J_{lin} . Since these expressions are defined according to the Bondi metric, with the Bondi radial coordinate r (rather than ρ), u derivatives are taken along curves of constant r . Thus $H_{lin} = J_{lin,u}$.

From this, the linearized News function can be expressed as

$$\mathcal{N}_{lin} = \Re \left(e^{iv u} \lim_{r \rightarrow \infty} \left(\frac{\ell(\ell+1)}{4} J_{\ell} - \frac{iv r^2}{2} J_{\ell,r} \right) + e^{iv u} \beta_{\ell} \right) \sqrt{\frac{(\ell+2)!}{(\ell-2)!}} {}^2Z^{\ell m}. \quad (2.133)$$

Ref [136] explicitly wrote out the solutions to the linearized evolution quantities and News function for the $\ell = 2$ and $\ell = 3$ modes, which we reproduce here. For $\ell = 2$,

$$\begin{aligned} \beta_2 &= B_2, \\ J_2(r) &= \frac{24B_2 + 3ivC_{2a} - iv^3C_{2b}}{36} + \frac{C_{2a}}{4r} - \frac{C_{2b}}{12r^3}, \\ U_2(r) &= \frac{-24ivB_2 + 3v^2C_{2a} - v^4C_{2b}}{36} + \frac{2B_2}{r} + \frac{C_{2a}}{2r^2} + \frac{ivC_{2b}}{3r^3} + \frac{C_{2b}}{4r^4}, \\ W_2(r) &= \frac{24ivB_2 - 3v^2C_{2a} + v^4C_{2b}}{6} + \frac{3ivC_{2a} - 6B_2 - iv^3C_{2b}}{3r} - \frac{v^2C_{2b}}{r^2} + \frac{ivC_{2b}}{r^3} + \frac{C_{2b}}{2r^4}, \\ \mathcal{N}^{2m} &= \Re \left(\frac{iv^3C_{2b}}{\sqrt{24}} e^{iv u} \right) {}^2Z^{2m}, \end{aligned} \quad (2.134)$$

and for $\ell = 3$,

$$\begin{aligned} \beta_3 &= B_3, \\ J_3(r) &= \frac{60B_3 + 3ivC_{3a} + v^4C_{3b}}{180} + \frac{C_{3a}}{10r} - \frac{ivC_{3b}}{6r^3} - \frac{C_{3b}}{4r^4}, \\ U_3(r) &= \frac{-60ivB_3 + 3v^2C_{3a} - iv^5C_{3b}}{180} + \frac{2B_3}{r} + \frac{C_{3a}}{2r^2} - \frac{2v^2C_{3b}}{3r^3} + \frac{5ivC_{3b}}{4r^4} + \frac{C_{3b}}{r^5}, \\ W_3(r) &= \frac{60ivB_3 - 3v^2C_{3a} + iv^5C_{3b}}{15} + \frac{ivC_{3a} - 2B_3 + v^4C_{3b}}{3r} \\ &\quad - \frac{2iv^3C_{3b}}{r^2} - \frac{4iv^2C_{3b}}{r^3} + \frac{5vC_{3b}}{2r^4} + \frac{3C_{3b}}{r^5}, \end{aligned}$$

$$\mathcal{N}^{3m} = \Re \left(\frac{-v^4 C_{3b}}{\sqrt{30}} e^{iv_u} \right)^2 Z^{3m}, \quad (2.135)$$

where $B_\ell, C_{\ell a}$ and $C_{\ell b}$ are all freely chosen complex constants. Note that only the values of $C_{\ell b}$ show up in the expression for the News.

For the tests we performed here, we follow a similar setup as in [135, 136], where we evolve a system which is a simple linear combination of the (2,2) and (3,3) modes. Specifically, the parameter values are $v = 1$, $B_\ell = .5i\alpha$, $C_{\ell a} = 1.5\alpha$, and $C_{2b} = -iC_{3b} = .5\alpha$, where the constant α sets the amplitude of the resulting News as well as the scale of the linearity of the system. Because we evolve the entire nonlinear solution, and not just a linearized version, we expect our results to differ from the analytic solution with differences that scale as the square of the amplitude, α^2 .

We place these linearized values of the evolution quantities (J, W, U, β) on a chosen world tube to serve as the inner boundary values for the volume evolution. By starting with the world tube in the Bondi metric, we bypass the entire inner boundary formalism since we are already starting with the Bondi metric quantities. To make this test even more demanding, we chose our world tube such that its Bondi radius varies both in time and across the surface, given by the formula

$$R = 5 \left(1 + \frac{(-.42x + .29y + .09z)(.2x + .1y - .12z)(.7x + .1y - .3z)(.12x - .31y - .5z)}{(x^2 + y^2 + z^2)^2} \sin \pi u \right). \quad (2.136)$$

We chose this distortion of the Bondi radius somewhat arbitrarily, ensuring that it had distortions with modes up through $\ell = 4$ as well as a time varying component with a frequency distinct from that of the linearized perturbation. This tests the code's ability to distinguish between H and Φ with a correct handling of the moving world tube Bondi radius, R , at least to linear order. Since this test bypasses the inner boundary formalism, we can not make any claim about whether the coordinate radius \tilde{r} of the world tube is moving as there is no defined coordinate radius.

The data for J on the initial slice we also read off from Eq. (2.131). With the world tube metric values and initial slice established, we evolve the full characteristic system. We resolve SWSH modes through $\ell = 8$ with a radinull resolution of 20 grid points and relative time integration error tolerance of 10^{-8} . We test the characteristic evolution against perturbation amplitudes of $\alpha = (10^{-2}, 10^{-3}, 10^{-4}, 10^{-5}, 10^{-6}, 10^{-7}, 10^{-8})$ from $u = 0$ to $u = 10$. We compute the difference between the computed News and the analytic results from Eq. (2.133), $|\Delta N^{\ell m}| = |N_{\text{Char}}^{\ell m} - N_{\text{lin}}^{\ell m}|$ in Fig 2.2. Note, we are examining the News function evaluated at the \mathcal{S}^+ coordinates (u, θ, ϕ) , rather than the inertial coordinates, $(\tilde{u}, \tilde{\theta}, \tilde{\phi})$ because we expect the difference between the two systems to be a small correction to the linearized values.

From Fig 2.2 we clearly see that when $\alpha \gtrsim 10^{-6}$, $|\Delta N^{\ell m}|$ scales as α^2 . When $\alpha \lesssim 10^{-6}$, the difference in News rapidly reaches a floor below 10^{-14} for the smallest amplitude perturbations. Modes other than $(2, \pm 2)$ and $(3, \pm 3)$ all converge towards 0 with scaling behavior no worse than $|\Delta N^{\ell m}| \lesssim O(\alpha^2)$ until reaching machine roundoff. The observed scaling with α matches the ex-

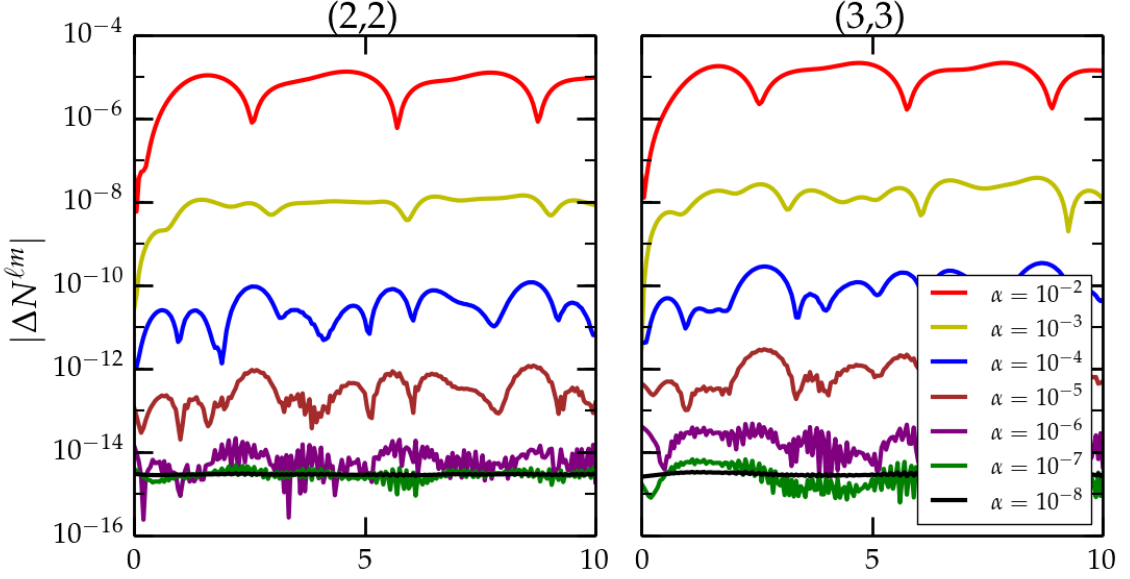


Figure 2.2: The difference between the numerically evolved News function and the analytic solution for the linearized analytic test of Section 2.6, for various amplitudes of the linear perturbation α . The (2,2) mode is on the left and the (3,3) mode on the right. We expect differences of order α^2 because we evolve the nonlinear terms that the linearized analytic solution neglects. For both modes, the magnitude of the differences scales as at least α^2 until they approach numerical roundoff.

pected scaling: we are evolving the full nonlinear equations but are comparing to an analytic solution of the linearized equations.

Previous iterations of CCE codes have performed a similar linearized analytic test [23, 134]. While their choice of parameters differs slightly from ours, they are both most similar to our $\alpha = 10^{-6}$, with inner boundaries at fixed, uniform R world tube surfaces. The error in their News at the resolutions they tested was worse than 10^{-10} , whereas the error in our News for the $\alpha = 10^{-6}$ case is at the order of 10^{-14} , hovering just about the error of our numerical roundoff. While comparing our results to theirs is not exactly a 1-1 comparison, we believe this is evidence for how effective our code is at resolving the linear case.

Teukolsky Wave

A Teukolsky wave is a solution of a propagating gravitational wave in the perturbative limit of Einstein's equations. For outgoing waves the metric has the form [152]

$$\begin{aligned}
 ds^2 = & -d\check{t}^2 + (1 + \check{f}_{rr})d\check{r}^2 + 2B\check{f}_{r\theta}\check{r}d\check{r}d\check{\theta} + 2B\check{f}_{r\phi}\check{r}\sin\check{\theta}d\check{r}d\check{\phi} + (1 + C\check{f}_{\theta\theta}^{(1)} + A\check{f}_{\theta\theta}^{(2)})\check{r}^2d\check{\theta}^2 \\
 & + 2(A - 2C)\check{f}_{\theta\phi}\check{r}^2\sin\check{\theta}d\check{\theta}d\check{\phi} + (1 + C\check{f}_{\phi\phi}^{(1)} + A\check{f}_{\phi\phi}^{(2)})\check{r}^2\sin^2\check{\theta}d\check{\phi}^2,
 \end{aligned} \tag{2.137}$$

where the functions \check{f}_{ij} are known functions of angles listed below, and the functions $A, B,$ and C are computed from the freely specifiable function $F(\check{u}) = F(\check{t} - \check{r}),$

$$\begin{aligned} A &= 3 \left(\frac{d_{\check{u}}^2 F}{\check{r}^3} + \frac{3d_{\check{u}} F}{\check{r}^4} + \frac{3F}{\check{r}^5} \right), \\ B &= - \left(\frac{d_{\check{u}}^3 F}{\check{r}^2} + \frac{3d_{\check{u}}^2 F}{\check{r}^3} + \frac{6d_{\check{u}} F}{\check{r}^4} + \frac{6F}{\check{r}^5} \right), \\ C &= \frac{1}{4} \left(\frac{d_{\check{u}}^4 F}{\check{r}} + \frac{2d_{\check{u}}^3 F}{\check{r}^2} + \frac{9d_{\check{u}}^2 F}{\check{r}^3} + \frac{21d_{\check{u}} F}{\check{r}^4} + \frac{21F}{\check{r}^5} \right), \end{aligned} \quad (2.138)$$

where $d_{\check{u}}$ is the total derivative with respect to \check{u} . The choice of $F(\check{t} - \check{r})$ specifies outward propagating waves, as opposed to $F(\check{t} + \check{r})$ which would generate ingoing waves.

Following [22, 79], we choose the outgoing solution corresponding to the SWSH ${}^2Y^{20}$ mode, defining the \check{f}_{ij} from above as

$$\begin{aligned} \check{f}_{rr} &= 2 - 3 \sin^2 \check{\theta}, \quad \check{f}_{r\theta} = -3 \sin \check{\theta} \cos \check{\theta}, \quad \check{f}_{r\phi} = 0, \\ \check{f}_{\theta\theta}^{(1)} &= 3 \sin^2 \check{\theta}, \quad \check{f}_{\theta\theta}^{(2)} = -1, \quad \check{f}_{\theta\phi} = 0, \\ \check{f}_{\phi\phi}^{(1)} &= -\check{f}_{\theta\theta}^{(1)}, \quad \check{f}_{\phi\phi}^{(2)} = 3 \sin^2 \check{\theta} - 1, \end{aligned} \quad (2.139)$$

and defining the profile of the waves with $F(\check{u}) = \alpha e^{-\check{u}^2/\tau^2}$, where α and τ are the amplitude and width of the wave, respectively. This is slightly different than the choice of $F(\check{u})$ used in either [79] or [22].

Because this solution starts with a metric that is not in Bondi-Sachs form, this test utilizes the full inner boundary formalism, in contrast to the linearized analytic test in section 2.6, which tests only the characteristic evolution. We evaluate the components of the metric (see Eq. (2.137)) at a world tube of constant radius, $\check{r}|_{\Gamma}$. The spatial 3-metric \check{g}_{ij} is computed from the various \check{f}_{ij} transformed into a Cartesian basis, the shift is $\check{\beta}^i = 0$, and the lapse is $\check{\alpha} = 0$.

Given the metric and its derivatives evaluated on a world tube, the inner boundary formalism creates a correspondence between time and angular coordinates on the world tube and at \mathcal{S}^+ , i.e. $(u = \check{t}, \theta = \check{\theta}, \phi = \check{\phi})$. With that in mind, the News function of this waveform at \mathcal{S}^+ is given by the formula [22]

$$\mathcal{N} = -\frac{3 \sin^2 \check{\theta}}{4} \partial_{\check{u}}^5 F(\check{u}), \quad (2.140)$$

where here $\check{u} = u - \check{r}|_{\Gamma}$. For our choice of $F(\check{u})$,

$$\mathcal{N}^{20} = \alpha \sqrt{\frac{6\pi}{5}} e^{-\check{u}^2} (120\check{u} - 160\check{u}^3 + 32\check{u}^5) \quad (2.141)$$

with all other News modes $\mathcal{N}^{\ell m \neq 20} = 0$. When we compare our computed News with this analytic News, we do so using the News evaluated on the coordinates (u, θ, ϕ) , rather than the inertial ones $(\check{u}, \check{\theta}, \check{\phi})$.

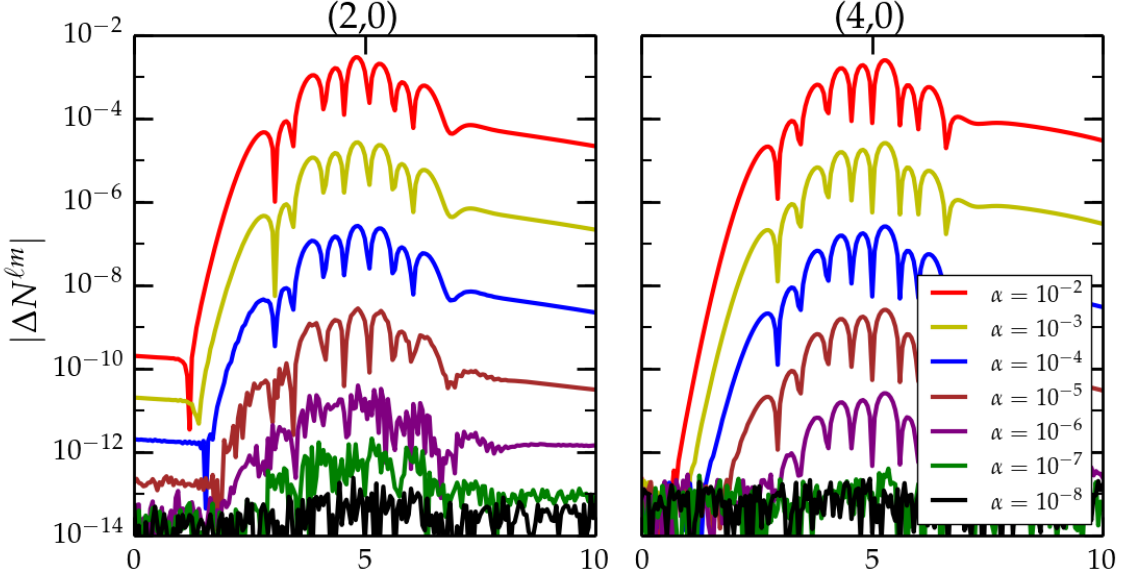


Figure 2.3: The difference between the numerically evolved News function and the analytic solution for the Teukolsky wave test of Section 2.6, for various amplitudes of the linear perturbation α . The (2,0) mode is on the left and the (4,0) mode on the right. We expect differences of order α^2 because we evolve the nonlinear terms that the Teukolsky wave solution neglects. For both modes, the magnitude of the differences scales as at least α^2 until it approaches numerical roundoff.

Because this is a solution of the linearized Einstein equations, comparing with our numerical solution of the full nonlinear equations should yield differences that scale like α^2 . Note that even though we represent the magnitude of the linear perturbation with α in both this test and the linearized analytic test above, the absolute amplitude for a given α is not the same for the two tests. The Teukolsky wave News function here is over two orders of magnitude larger than the linearized analytic solution for the same value of α .

For our test, the worldtube is at coordinate radius of $\check{r}_{|\Gamma} = 5$, and we start the wave at the origin with a width of $\tau = 1$ with amplitudes $\alpha = (10^{-2}, 10^{-3}, 10^{-4}, 10^{-5}, 10^{-6}, 10^{-7}, 10^{-8})$. The CCE code is run to resolve the News up through $\ell = 8$ modes with 20 radinull points and a relative time integration error tolerance of $\approx 4 \times 10^{-6}$. We evolve the system from $u = 0$ through $u = 10$, which starts and ends when the metric is effectively flat.

We show the difference between the numerical evolution and the (2,0) mode of the analytic News from Eq. (2.141), $|\Delta N^{20}| = |N_{CCE}^{20} - N^{20}|$ on the left side of Fig 2.3. We see for larger perturbations ($\alpha \gtrsim 10^{-6}$) the difference in the News scales with α^2 , while for smaller perturbations ($\alpha \lesssim 10^{-6}$) $|\Delta N^{20}|$ reaches a floor below 10^{-12} . For other $\ell = \text{even}$, $m = 0$ modes, such as the (4,0) mode plotted on the right half of Fig 2.3, the behavior is similar. Because we chose a solution with $m = 0$, all $m \neq 0$ modes of the numerical solution vanish to numerical roundoff error for all α .

This behavior is very similar to what we see for the linearized analytic test. This confirms that our

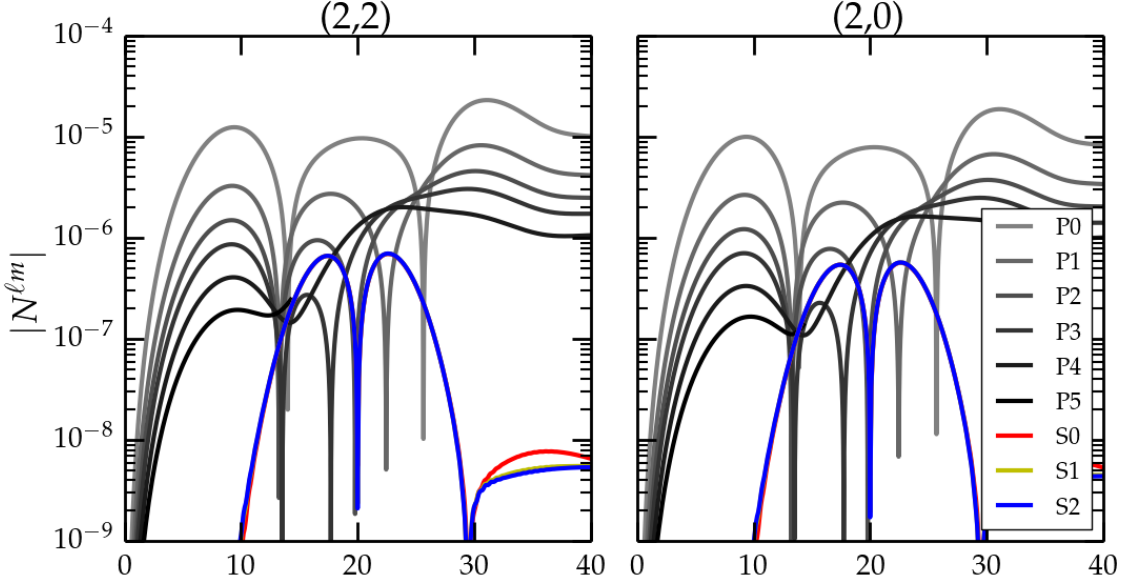


Figure 2.4: The absolute values of the News modes for the (2,2) and (2,0) for both the SpEC (color) and PittNull (grayscale) CCE codes. Because the SpEC results lie on top of each other (so that only S2 is clearly visible here), we infer that the SpEC code has converged to a slightly nonzero answer. This nonzeroness is nonetheless below what the PittNull code achieves, even at extremely high resolutions. While the PittNull code is still converging towards 0, it has not reached the level of accuracy of the SpEC code, especially near the beginning and end of the cycle as the offcenter translation vanishes.

CCE code solves the linear solution. Because this test also incorporates the full inner boundary formalism (as opposed to the linearized analytic test which does not), this also confirms that to linear order, we reproduce the Bondi metric on the world tube.

Rotating Schwarzschild

Following the test used in [35], we generate data corresponding to the Schwarzschild metric in Eddington-Finkelstein coordinates with a rotated coordinate transformation, $\check{\phi} \rightarrow \check{\phi} + \omega \check{u}$, so the metric is

$$d\check{s}^2 = - \left(1 - \frac{2M}{\check{r}} - \omega^2 \check{r}^2 \sin^2 \check{\theta} \right) d\check{u}^2 - 2d\check{u}d\check{r} + 2\omega \check{r}^2 \sin^2 \check{\theta} d\check{u}d\check{\phi} + \check{r}^2 \sin^2 \check{\theta} d\check{\Omega}^2, \quad (2.142)$$

where M is the mass, ω is the parameter of the transformation, and \check{u} is the coordinate $\check{u} = \check{t} - \check{r}^*$. For our test, we chose $M = 1$ and $\omega = .1$. The world tube has a radius of $R = 3M$ and the solution is evolved from $u = 0M$ to $u = .5M$. We ran our code with an *absolute* time integration error tolerance of 10^{-12} , and inertial coordinate damping parameter of $\kappa = 10$. The resulting numerical values of all the News modes (resolved up through $\ell = 8$) are below absolute values of 10^{-12} .

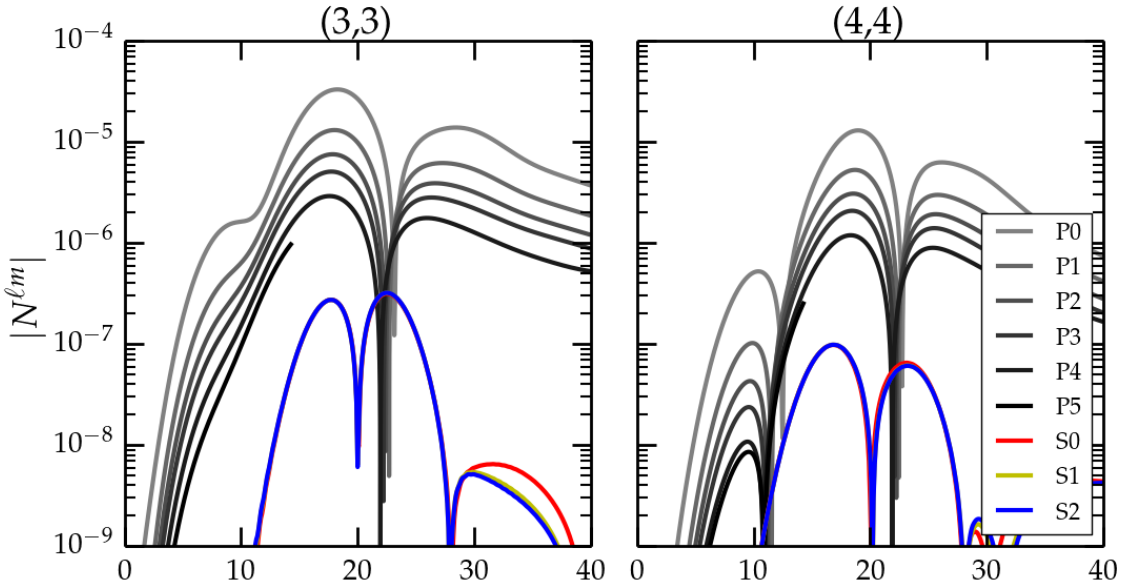


Figure 2.5: The absolute values of the News modes for the (3,3) and (4,4) for both the SpEC (color) and PittNull (grayscale) CCE codes. Similar to what we find in Fig 2.4, the SpEC code has converged to a marginally nonzero answer that is below the PittNull results. For these modes the SpEC code is significantly better than PittNull even near the peak amplitude of SpEC. While PittNull is still converging towards zero, even the highest resolution is nearly an order of magnitude larger than the SpEC result.

Bouncing Black Hole

One expected key feature of CCE is its ability to remove gauge effects from the resulting waveform regardless of the coordinates of the Cauchy metric. We construct a test similar to those in [22, 134]. We start with a Schwarzschild black hole and apply a simple time-dependent periodic coordinate translation on the spacetime. Doing so produces a time-dependent, periodic metric at the (coordinate-stationary) world tube, but because this black hole is not radiating, the News function of this spacetime should be zero; the goal of this test is to verify that we indeed get zero in this nonlinear, time-dependent situation.

Specifically, the solution is that of a Schwarzschild black hole with mass $M = 1$ in Kerr-Schild coordinates $(\check{t}, \check{x}, \check{y}, \check{z})$, with a simple oscillating coordinate transformation

$$\check{x} \rightarrow \check{x} + a \sin^4\left(\frac{2\pi\check{t}}{b}\right), \quad (2.143)$$

where in our test we chose $a = 2M$ and $b = 40M$. Thus, in the coordinate frame, which is also the frame of the world tube, the black hole will appear to bounce back and forth along the \check{x} -axis, but there is no radiated gravitational wave content. The world tube is placed at $\check{r}_\Gamma = 15M$, which is intentionally very small compared to what would be used for a compact binary simulation (typically hundreds of M); we chose an artificially small world tube to produce an extremely difficult test of

the CCE code. We evolve the system from $u = 0M$ to $u = 40M$, one full period of the coordinate oscillation, starting and ending when the coordinates of the black hole are at the origin.

We performed the characteristic evolution with our spectral code at 3 different resolutions, which we label as S_k , where k is (0,1,2). We set the resolution at each level of refinement as follows: we retain SWSH modes ${}^s Y^{\ell m}$ through $\ell_{\max} = 8 + 2k$, we use $20 + 2k$ collocation points in the radinull direction, and the adaptive timestepper uses a relative error tolerance of $3 \times 10^{-5} \times e^{-k}$ with a maximum step size of $\Delta u = .5$. For each resolution, we ran our code on a single core on the *Wheeler* cluster at Caltech, taking less than (15,30,70) minutes for the (S0, S1, S2) resolutions, respectively.

For simplicity, we examine the News at \mathcal{I}^+ in the coordinates (u, θ, ϕ) rather than in the inertial coordinates $(\tilde{u}, \tilde{\theta}, \tilde{\phi})$. Similarly, we expand the News into spherical harmonic modes ${}^2 Y^{\ell m}(\theta, \phi)$. Since the News function is supposed to be zero uniformly, simple coordinate transformations at \mathcal{I}^+ are not expected to affect the overall results presented here.

As a baseline for comparison, we also ran the PittNull code on the same world tube data. We ran PittNull at multiple resolutions (P0-P5). These correspond to a resolution of $(100^3, 200^2, 300^3, 400^3, 600^3, 900^3)$ spatial points and fixed time steps of $\Delta u = (.05, .025, .01667, .0125, .00833, .00556)M$. Because PittNull takes significant computational resources at high resolution, we intentionally terminated the P5 simulation after less than $15M$. During the time that it ran, that simulation continued trends seen in the lower resolution PittNull simulations. The PittNull resolutions (P0, P1, P2) were run on 24 cores on the *Wheeler* cluster at Caltech, taking approximately (850, 2650, 5350) total CPU-hours, respectively, while resolutions (P3, P4, P5) were run on 512 cores on the BlueWaters cluster, taking approximately (9000, 17000, 24000) total CPU-hours, respectively. In the case of P5, that corresponds to the cost expended on the simulation before we terminated it. This massive discrepancy on computational cost between the two codes demonstrates the impressive speed up achieved by utilizing spectral methods, similar to what was observed with the previous implementation of this spectral code [87, 88].

In Fig 2.4 and Fig 2.5, we plot the amplitude of the (2,2), (2,0), (3,3) and (4,4) modes of the News for both codes for all resolutions for one oscillation period. In both codes, the amplitude of the $\ell + m = \text{odd}$ modes vanishes except for numerical roundoff, likely due to the planar symmetry of the system. For the $\ell + m = \text{even}$ modes the computed numerical News is nonzero for both codes at finite resolution.

We see in Fig 2.4 that for the $\ell = 2$ modes the SpEC code does a better job than the PittNull code does at removing the gauge effects from the News function, at our chosen finite resolution. This is especially true at the beginning and end of the oscillations when the difference between the shifted coordinates and Schwarzschild is minor. The limitation of the finite differencing approach of PittNull in effect sets a noise floor of the simulation, dependent on the spatial resolution. Thus, when the coordinates return to the usual Kerr-Schild coordinates at the end of one period, the noise floor in PittNull limits its ability to generate numerically vanishing News. In contrast, the News

generated by the SpEC code both remains numerically small for longer at the start of the simulation and shrinks to values orders of magnitude smaller than PittNull at the end of the simulation.

During the middle of the period, when the coordinate effects on the world tube metric are the largest, the SpEC News mode is of almost comparable size to PittNull for the (2,2) and (2,0) modes, yet even the highest-resolution PittNull results are generally worse than the SpEC results except near zero crossings. Examining some of the higher order modes, like the (3,3) or (4,4) modes in Fig 2.5, exacerbates this disparity, where the peak error SpEC results are roughly an order better than those of PittNull.

However, when comparing results with different resolutions, we find a signature of some small error in SpEC in the above plots. In both Fig 2.4 and Fig 2.5, we show all three SpEC resolutions, however all three curves lie on top of each other for almost the entire duration of the simulation. We would expect that the three curves would continue to converge toward zero as resolution increases. This lack of convergence implies that there is an unaccounted error in the code. It is unclear whether the source of this error is a coding error, a missing or incorrect term in the complicated evolution equations or unaccounted theoretical concept. It is possible that this could be a numerical limitation of the computational methods we have employed, but we deem that unlikely due to the results of the gauge wave test, as we describe below in Section 2.6. We doubt that this error is a result of the finite world tube data as refining neither the step size $\Delta\check{r}$ nor the angular resolution of the world tube metric affected the resulting News modes. Nor is it an instability as our SpEC evolution is stable after 3 oscillations of the coordinates (not shown here).

This test is a rather extreme test of the code’s ability to distinguish coordinate effects, with the black hole appearing to move an appreciable fraction of the world tube’s radius in its coordinate frame. We also ran our code on this identical system except placing the world tube radius at a series of different coordinate values, $\check{r}_{|\Gamma} \in (10, 12, 15, 20, 25)M$, spread quasi-uniformly in $1/\check{r}$, and measured the resulting News function. In Fig 2.6, we plot the amplitude of our code’s (2,2) mode for each of these world tube radii.

Moving the world tube to smaller radii raises the error as might be expected; eventually if the world tube is close enough to the BH we expect caustics to form (*i.e.* radially outward null rays cross paths) and the characteristic formulation fails. There is a clear convergence of this error to zero as we move the world tube further away and the relative size of the coordinate transformation of the bouncing BH shrinks. Even moderate shifts in the radius have large effects; a factor of 2 in \check{r} from $10M$ to $20M$ decreases the size of the News by nearly 3 orders of magnitude.

Typical simulations of compact binary mergers often place the outer edge of their domain boundaries with coordinate radii $\check{r} \geq 500M$, so CCE in such simulations would employ a world tube of similar size. Given the behavior of our code’s error with world tube radius, we expect that whatever error is causing the nonconvergent behavior seen in Figs. 2.4–2.6, it will be negligible for compact binary simulations.

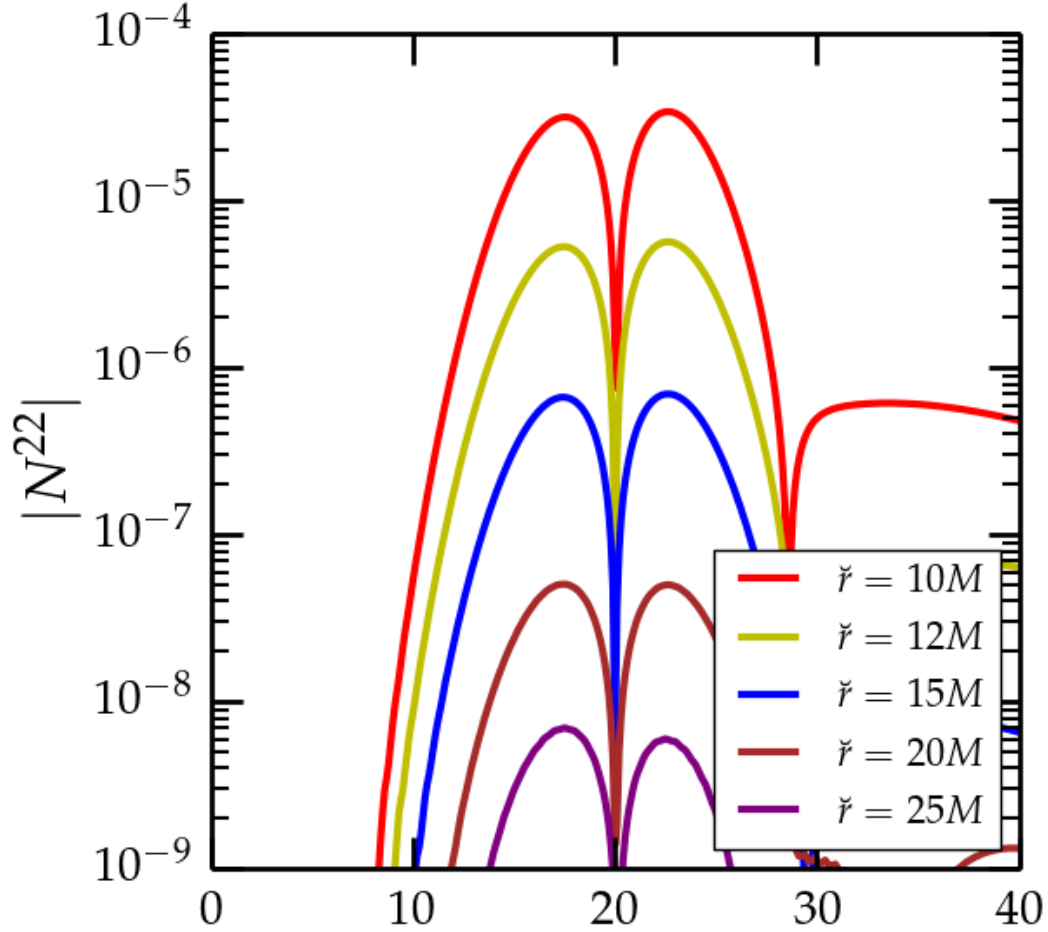


Figure 2.6: The absolute values of the (2,2) News modes from our SpEC code for different coordinate world tube radii \check{r} .

Even with a very small world tube radius that maximizes the size of the nonconvergent error, the error is still small enough that PittNull cannot quite resolve it. This thwarted our attempts to discover the source of the nonconvergent error by comparing with PittNull.

Gauge Wave

The bouncing black hole test is a measure of the code's ability to remove coordinate effects resulting from simple translations; we now introduce a test to examine the code's ability to distinguish between outgoing gravitational waves and gauge waves propagating along null slices. To generate this gauge wave, we again start with a Schwarzschild metric in Eddington-Finkelstein coordinates and apply the transformation of $\check{v} = \check{t} + \check{r} + F(\check{t} - \check{r})/\check{r}$ where $F(\check{u})$ is an arbitrary function,

$$d\check{s}^2 = - \left(1 - \frac{2M}{\check{r}}\right) \left(1 + \frac{d_{\check{u}}F}{\check{r}}\right)^2 d\check{t}^2 + 2 \left(1 + \frac{d_{\check{u}}F}{\check{r}}\right) \left(\frac{2M}{\check{r}} + \left(1 - \frac{2M}{\check{r}}\right) (\check{r} d_{\check{u}}F + F)\right) d\check{t} d\check{r}$$

$$+ \left(1 - \frac{d_{\check{u}}F}{\check{r}} - \frac{F}{\check{r}^2}\right) \left(1 + \frac{2M}{\check{r}} + \left(1 - \frac{2M}{\check{r}}\right) \left(\frac{d_{\check{u}}F}{\check{r}} + \frac{F}{\check{r}^2}\right)\right) d\check{r}^2 + \check{r}^2 d\check{\Omega}^2. \quad (2.144)$$

Here M is the mass of the black hole and $d_{\check{u}}$ is the total derivative with respect to \check{u} . For the test, $M = 1$ and we chose F to be a sine-Gaussian,

$$F(\check{u}) = \alpha \sin(w\check{u} + p_0) e^{-\frac{(\check{u}-\check{u}_0)^2}{k^2}}. \quad (2.145)$$

Here α is the amplitude of the gauge wave, w is the frequency, p_0 is the initial phase offset, \check{u}_0 is time when the peak is at the origin, and k is its characteristic width. For our test, we choose $\alpha = 1M$, $w = .5/M$, $p_0 = .01$, $\check{u}_0 = 40M$, and $k = 10$.

Because this system is spherically symmetric, most of the terms in the evolution are trivially 0. In order to incorporate them as part of the evolution, we also apply an additional translation to displace the center of the black hole from the center of the world tube. The translation used is

$$\check{z} \rightarrow \check{z} + 2 \left(1 - e^{-(\check{t}/40)^4}\right). \quad (2.146)$$

By moving the system entirely along the \check{z} -axis, we expect only $m = 0$ modes to be excited. We choose the worldtube radius to be $\check{r}_\Gamma = 50M$. Our gauge wave is configured so that the peak will propagate outwards and pass through this world tube at $\check{t} = 90M$.

We run our SpEC CCE code at three different resolutions, Sk , for $k = (0, 1, 2)$. This corresponds to angular resolution of $\ell_{\max} = 8 + 2k$, radial resolution of $20 + 2k$ and *absolute* time integration error tolerance of $10^{-12}e^{-k}$. The three resolutions, (S0, S1, S2) were ran on a single core on Caltech's *Wheeler* cluster for approximately (35, 75, 165) minutes.

PittNull CCE was also run at three resolutions, $P0 - P2$ corresponding to a finite differencing grid with $(100^3, 200^3, 300^3)$ spatial points and fixed time steps of size $\Delta u = (.05, .025, 0.01667)M$. Each resolution was run on 256 cores on the Blue Waters cluster, costing approximately (1100, 3200, 6000) CPU-hours.

In Fig 2.7, we plot the amplitude of the (2,0) and (3,0) News modes for both codes and in both modes. We expect the news to be zero because the solution is merely Schwarzschild in moving coordinates. At early and late times, both codes show convergence towards zero, with SpEC several orders of magnitude below PittNull. During the peak of the gauge wave, we see some lack of convergence in SpEC, at a level that is far from being resolved in PittNull. This is probably the same effect that we observed in the bouncing black hole test.

Examining the higher ℓ modes yields a similar picture for both codes just at slightly decreasing amplitudes, as seen in the right panel of Fig. 2.7. Also, as expected by the axisymmetry of the setup for this test, both codes produce numerical noise for all $m \neq 0$ modes.

2.7 Appendices

Spin-Weighted Spherical Harmonics

Spin-Weighted Spherical Harmonics (SWSH) are a generalization of the typical spherical harmonics by introducing spin-weight raising (δ) and lowering operator ($\bar{\delta}$) [84, 118]. These derivative operator

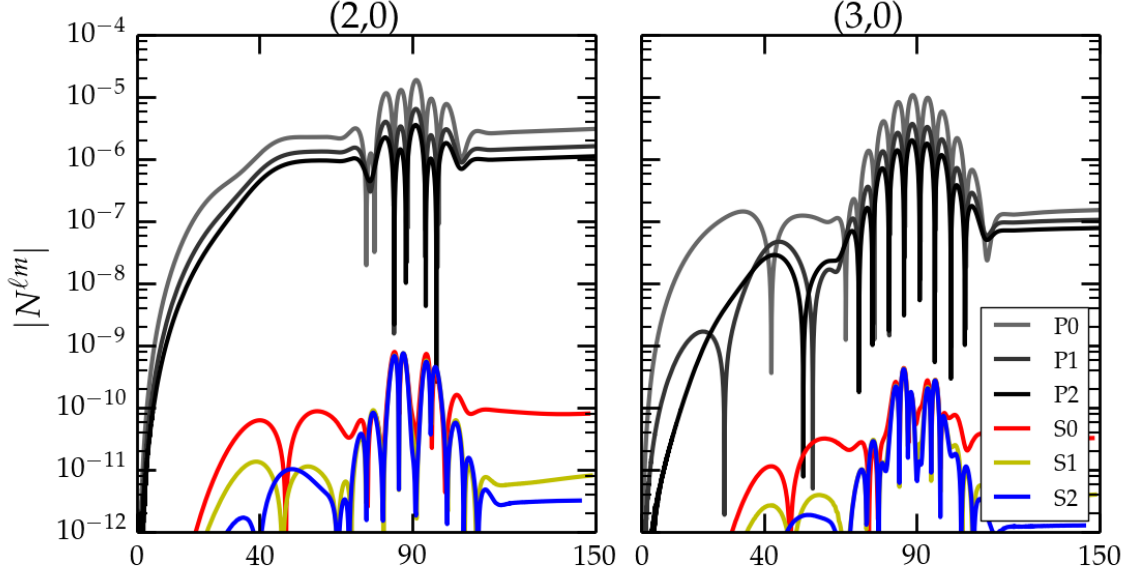


Figure 2.7: The amplitude of the (2,0) and (3,0) mode of the News, on the left and right respectively, for both SpEC (color) and PittNull (grayscale) CCE codes. The center of the coordinate shift offcenter occurs around $u = 40M$ while the peak of the Gauge Wave propagates through to \mathcal{S}^+ at $u = 90M$. At all times, the SpEC code is orders of magnitude better than the PittNull code. While the SpEC code shows convergence with resolution in the News at the times corresponding to the coordinate shift, numerical nonzeroness introduced as a result of the Gauge Wave itself is robust under resolution, implying a small error in the code.

are defined by contracting the dyad with the angular derivative operator,

$$\delta = q^A \partial_A, \quad (2.147)$$

$$\bar{\delta} = \bar{q}^A \partial_A. \quad (2.148)$$

By contracting these dyads with the tensor component gives the spin-weighted version of the quantities, computed above in Eqs. (2.8)–(2.11). The dyads contracted with a given quantity determine its spin-weight, with +1 for each q^A , -1 for each \bar{q}^A . For example, the spin-weight of $\delta \bar{J} = \frac{1}{2} \partial_A h_{BC} q^A \bar{q}^B \bar{q}^C$ is -1. Thus we see that (K, β, W) have spin-weight of 0, (Q, U) have spin-weight 1, and (J, H, Φ) have spin-weight 2.

Now we can also express δ as a complex spherical derivative operator on a given quantity F with a spin-weight of s ,

$$\delta F = -\sin^s \theta \left(\frac{\partial}{\partial \theta} + \frac{i}{\sin \theta} \frac{\partial}{\partial \phi} \right) (\sin^{-s} \theta F), \quad (2.149)$$

$$\bar{\delta} F = -\sin^{-s} \theta \left(\frac{\partial}{\partial \theta} - \frac{i}{\sin \theta} \frac{\partial}{\partial \phi} \right) (\sin^s \theta F). \quad (2.150)$$

While PittNull used a finite difference formulation for computing these derivatives [85], our code

will make use of how δ acts on individual SWSH modes,

$$\delta {}^s Y^{\ell m} = \sqrt{(\ell - s)(\ell + s + 1)} {}^{s+1} Y^{\ell m} \quad (2.151)$$

$$\bar{\delta} {}^s Y^{\ell m} = -\sqrt{(\ell + s)(\ell - s + 1)} {}^{s-1} Y^{\ell m} \quad (2.152)$$

With this, we can start from the regular spherical harmonics ($s = 0$) and build up the SWSH modes for arbitrary spin-weight.

And just like regular spherical harmonics, we can take an arbitrary spin-weighted function of and decompose into spectral coefficients with use of the expression of orthonormality of the SWSHes over the unit sphere,

$$\int_{S^2} {}^s Y^{\ell m} \overline{{}^s Y^{\ell' m'}} d\Omega = \delta_{\ell\ell'} \delta_{mm'}, \quad (2.153)$$

where $d\Omega$ is the area element of the unit sphere S^2 . Thus, given a spin-weighted quantity, we can decompose it as a sum of SWSH modes and take δ and $\bar{\delta}$ derivatives by applying the properties of Eq. (2.151),(2.152) to the spectral coefficients.

Lastly, we list some basic, useful properties of SWSHes:

- It is only possible to add together spin-weighted quantities of identical spin-weight.
- The spin-weight of a product of two SWSHes is the sum of their individual spin-weights.
- Because typical spherical harmonics are more generally SWSHes of spin-weight 0, SWSHes inherit the same mode properties of spherical harmonics (i.e. $\ell \geq 0, |m| \leq \ell$).
- In addition, the spin-weight serves as a lower bound on possible ℓ modes, $\ell \geq |s|$.
- The δ and $\bar{\delta}$ operators do not commute as, given spin-weighted quantity F , $\bar{\delta}\delta F = \delta\bar{\delta}F + 2sF$.

We utilize two external code packages to assist with the numerical implementation for the angular basis function, `Spherepack` [15, 55] for the standard spherical harmonics and `Spinsfast` [100] for the SWSHes. In particular, we use `Spherepack` primarily during the inner boundary formalism and partially during scri extraction, while we use `Spinsfast` during the volume evolution and scri extraction.

Nonlinear Evolution Equations

The full system of nonlinear equations appear below. The equations are the radinull equations on the null hypersurface of for a given time slice. Ref [39] computed these full nonlinear expressions, and first expressed them as SWSH quantities in [35], although we follow [87] by writing them in terms of the compactified coordinate ρ ,

$$\beta_{,\rho} = \frac{\rho(1-\rho)}{8} (J_{,\rho} \bar{J}_{,\rho} - K_{,\rho}^2), \quad (2.154)$$

$$\begin{aligned}
(r^2 Q)_{,\rho} = & \frac{1}{(1-\rho)^2} \left[R^2 \rho^2 \left(2\delta\beta_{,\rho} - K\delta K_{,\rho} - K\bar{\delta}J_{,\rho} + \delta(\bar{J}J_{,\rho}) + \bar{\delta}(JK_{,\rho}) - J_{,\rho}\bar{\delta}K \right. \right. \\
& \left. \left. + \frac{1}{2K^2} \left(\delta\bar{J}(J_{,\rho} - J^2\bar{J}_{,\rho}) + \delta J(\bar{J}_{,\rho} - \bar{J}^2 J_{,\rho}) \right) \right) \right] \\
& + \frac{1}{(1-\rho)^3} (-4R^2 \rho \delta\beta), \tag{2.155}
\end{aligned}$$

$$U_{,\rho} = \frac{e^{2\beta}}{R\rho^2} (KQ - J\bar{Q}), \tag{2.156}$$

$$\mathcal{R} = 2K - \delta\bar{\delta}K + \frac{1}{2} (\bar{\delta}^2 J + \delta^2 \bar{J}) + \frac{1}{4K} (\bar{\delta}\bar{J}\delta J - \bar{\delta}J\delta\bar{J}), \tag{2.157}$$

$$\begin{aligned}
(r^2 W)_{,\rho} = & \frac{1}{(1-\rho)^2} \left(-R + \frac{R^2 \rho^2}{4} (\delta\bar{U}_{,\rho} + \bar{\delta}U_{,\rho}) - e^{-2\beta} \frac{R^3 \rho^4}{8} (2KU_{,\rho}\bar{U}_{,\rho} + J\bar{U}_{,\rho}^2 + \bar{J}U_{,\rho}^2) \right. \\
& \left. + \frac{Re^{2\beta}}{2} \left(\mathcal{R} - 2K(\delta\beta\bar{\delta}\beta + \bar{\delta}\delta\beta) + J\bar{\delta}\beta^2 + \bar{J}\delta\beta^2 - \delta\beta(\bar{\delta}K - \delta\bar{J}) \right. \right. \\
& \left. \left. - \bar{\delta}\beta(\delta K - \bar{\delta}J) + J\bar{\delta}^2\beta + \bar{J}\delta^2\beta \right) \right) \\
& + \frac{1}{(1-\rho)^3} (R^2 \rho (\delta\bar{U} + \bar{\delta}U)), \tag{2.158}
\end{aligned}$$

The evolution equation of J is given by $H = J_{,u}|_{r=\text{const}}$,

$$(rH)_{,\rho} - (rJ)(H\bar{T} - \bar{H}T) = H_A + \frac{H_{B1} + H_{B2} + H_{B3} + H_{B4}}{1-\rho} + \frac{H_C}{(1-\rho)^2}, \tag{2.159}$$

where,

$$T = \left(J_{,\rho} - \frac{JK_{,\rho}}{K} \right), \tag{2.160}$$

$$H_A = (1-\rho)J_{,\rho} + \frac{R}{2}\rho^2 W_{,\rho} J_{,\rho} + \frac{\rho}{2}(1-\rho + R\rho W)J_{,\rho\rho} - 4J\beta_{,\rho}, \tag{2.161}$$

$$\begin{aligned}
H_{B1} = & \frac{R\rho}{4} \left((6-4\rho)WJ_{,\rho} - 16JW\beta_{,\rho} - \delta J\bar{U}_{,\rho} - \bar{\delta}J U_{,\rho} + K\delta U_{,\rho} - J_{,\rho}(\delta\bar{U} + \bar{\delta}U) \right. \\
& \left. - \delta J\bar{U}_{,\rho} + J(\bar{\delta}U_{,\rho} - \delta\bar{U}_{,\rho}) \right), \tag{2.162}
\end{aligned}$$

$$\begin{aligned}
H_{B2} = & \frac{R\rho}{4} \left((\bar{U}\delta J + U\bar{\delta}J)(J\bar{J}_{,\rho} - \bar{J}J_{,\rho}) - 2\bar{U}\delta J_{,\rho} - 2U\bar{\delta}J_{,\rho} \right. \\
& \left. + 2(KJ_{,\rho} - JK_{,\rho})(\bar{U}\delta K + U\bar{\delta}K + K(\delta\bar{U} - \bar{\delta}U) + J\bar{\delta}\bar{U} - \bar{J}\delta U) \right), \tag{2.163}
\end{aligned}$$

$$\begin{aligned}
H_{B3} = & \frac{e^{2\beta}}{2\rho} \left((2+J\bar{J})(\delta^2\beta + \bar{\delta}\beta^2) + J^2(\bar{\delta}^2\beta + \delta\beta^2) - 2JK(\delta\bar{\delta}\beta + \bar{\delta}\beta\delta\beta) \right. \\
& \left. + J(\delta K\bar{\delta}\beta - \bar{\delta}\beta\bar{\delta}K + \delta\bar{J}\delta\beta) + \bar{J}\delta J\delta\beta + K(\bar{\delta}J\delta\beta - \delta J\bar{\delta}\beta - 2\delta K\bar{\delta}\beta) \right), \tag{2.164}
\end{aligned}$$

$$H_{B4} = \frac{e^{-2\beta}R^2\rho^3}{8} \left((2+J\bar{J})U_{,\rho}^2 + 2JKU_{,\rho}\bar{U}_{,\rho} + J^2\bar{U}_{,\rho}^2 \right), \tag{2.165}$$

$$H_C = -\frac{R}{2} (2K\delta U + \delta J\bar{U} + \bar{\delta}J U - J\bar{\delta}U + J\delta\bar{U}). \tag{2.166}$$

The quantities J, β , and Q are all dimensionless while U, W, H , and Φ have units of $1/R$ (identically, units of $1/u$ in the case of H and Φ).

These equations correspond to different components of the Einstein equations, namely, $R_{rr} = 0$ gives $\beta_{,\rho}$, $R_{rA}q^A = 0$ gives $U_{,\rho}$, $R_{AB}h^{AB}=0$ gives $W_{,\rho}$, and $R_{AB}q^Aq^B = 0$ gives $H_{,\rho}$ and these cover all 6 degrees of freedom in the system. There are 4 other equations which can be written from the Einstein equations. As [35] discusses in more detail, of the four remaining components in Einstein equations, one of these is equations is essentially identically 0 ($R^r_r = 0$) while the other three ($R^r_u = 0$ and $R^r_Aq^A = 0$) serve as constraint conditions for the evolution on each of the null slices.

However, computing these constraint conditions involve knowing the u -derivatives of evolution quantities other than $J_{,u}$. Computing these derivatives via finite differencing methods across multiple null slices would significantly lower their accuracy relative to the rest of the code, limiting their ability to monitor our codes exact faithfulness to the Einstein equations during the course of the evolution. Thus, our current implementation does not make use of these constraint equations. One point of future improvement in our code would be their implementation in a manner which is consistant with the precision maintained by the rest of the code.

Paper Definition Key

Here we define the quantities we use in the paper for ease of reference.

$A = \omega e^{2\beta}$: Intermediate Quantity in News, Eq. (2.109)

$\check{\alpha}$: World Tube Metric Lapse

β : Lapse Part of Bondi Metric, Evolution Quantity

$\beta^{\check{i}}$: World Tube Metric Shift

D^A : Covariant Derivative Associated with $h_{|\mathcal{S}^+}^{AB}$

δ : Complex Angular Derivative Operator, Eq. (2.148)

Γ : World Tube Hypersurface

$g_{\mu\nu}$: Bondi Metric, Eq. (2.1)

$\hat{g}_{\mu\nu} = \ell^2 g_{\mu\nu}$: Compactified Bondi Metric, Eq. (2.97)

$\tilde{g}_{\mu\nu} = \omega^2 \hat{g}_{\mu\nu}$: Conformal Bondi Metric, Eq. (2.98)

$H = J_{,u}|_{r=\text{const}}$: Evolution Quantity

h_{AB} : Angular Part of Bondi Metric

\mathcal{S}^+ : Scri+, Future Null Infinity

$J = \frac{1}{2} h_{AB} q^A q^B$: Primary Evolution Quantity

$K = \sqrt{1 + J\bar{J}}$: Evolution Quantity

$\ell = 1/r$: Inverse Surface-Area Coordinate

$\ell^{\check{\mu}}$: World Tube Null Generator, Eq. (2.22)

- λ : World Tube Affine Radinull Parameter
 N : News Function, Eq. (2.108)
 \mathcal{N} : Analytic Value of News Function for Tests
 $n^{\hat{\mu}}$: World Tube Time Unit Vector, Eq. (2.21)
 \hat{n}^{μ} : Compactified Bondi Generator at \mathcal{I}^+ , Eq. (2.105),
 \tilde{n}^{μ} : Conformal Bondi Generator at \mathcal{I}^+ , Eq. (2.104),
 $\Phi = J_{,u}|_{\rho=\text{const}}$: Evolution Quantity
 $Q = Q_A q^A$: Intermediate Evolution Quantity
 Q_A : Intermediate Bondi Metric Term, Eq. (2.2)
 q_A : Complex Dyad, Eq. (2.38)
 q_{AB} : Unit Sphere Metric
 $R = r|_{\Gamma}$: Bondi Radius of world tube, Eq. (2.41)
 \mathcal{R} : 2D Curvature Scalar, Eq. (2.19),
 r : Bondi Radius
 $\rho = \frac{r}{R+r}$: Compactified Bondi Radius
 \check{r} : World Tube Coordinate Radius
 \check{s}^{μ} : World Tube Outward Normal Vector, Eq. (2.20)
 T : Intermediate Quantity in H , Eq. (2.160)
 \check{t} : World Tube Time Coordinate
 u : Bondi Time Coordinate
 \tilde{u} : Conformal Bondi Time Coordinate
 $U = U^A q_A$: Evolution Quantity
 U^A : Shift Part of Bondi Metric
 W : Mass Aspect of Bondi Metric, Evolution Quantity
 Ω : Conformal factor between $\tilde{g}_{\mu\nu}$ and $g_{\mu\nu}$
 $d\Omega$: Unit Sphere Area Element
 ω : Conformal factor between $\tilde{g}_{\mu\nu}$ and $\hat{g}_{\mu\nu}$, Eq. (2.99)
 x^{α} : Bondi Characteristic Coordinate
 $\check{x}^{\check{\alpha}}$: World Tube Coordinate
 $\bar{x}^{\bar{\alpha}}$: Intermediate Null Coordinate
 $\tilde{x}^{\tilde{\alpha}}$: Inertial Coordinate

Chapter 3

INTRODUCTION TO TIDAL SPLICING

Barkett, K. and Scheel, M. A. and Haas, R. and Ott, C. D. and Bernuzzi, S. and Brown, D. A. and Szilágyi, B. and Kaplan, J. D. and Lippuner, J. and Muhlberger, C. D. and Foucart, F. and Duez, M. D. (2016). “Gravitational waveforms for neutron star binaries from binary black hole simulations”. In: *Phys. Rev. D.* 93(4):044064, Feb 2016. DOI: [10.1103/PhysRevD.93.044064](https://doi.org/10.1103/PhysRevD.93.044064)

3.1 Preface

Gravitational waves from binary neutron star (BNS) and black hole/neutron star (BHNS) inspirals are primary sources for detection by the Advanced Laser Interferometer Gravitational-Wave Observatory. The tidal forces acting on the neutron stars induce changes in the phase evolution of the gravitational waveform, and these changes can be used to constrain the nuclear equation of state. Current methods of generating BNS and BHNS waveforms rely on either computationally challenging full 3D hydrodynamical simulations or approximate analytic solutions. We introduce a new method for computing inspiral waveforms for BNS/BHNS systems by adding the post-Newtonian (PN) tidal effects to full numerical simulations of binary black holes (BBHs), effectively replacing the nontidal terms in the PN expansion with BBH results. Comparing a waveform generated with this method against a full hydrodynamical simulation of a BNS inspiral yields a phase difference of < 1 radian over ~ 15 orbits. The numerical phase accuracy required of BNS simulations to measure the accuracy of the method we present here is estimated as a function of the tidal deformability parameter λ .

3.2 Introduction

In September 2015, the Advanced Laser Interferometer Gravitational-Wave Observatory (aLIGO) directly detected, for the first time ever, gravitational waves (GWs) [7] and the network of observatories will be joined shortly by advanced Virgo [14] and KAGRA [19]. The most likely GW sources for these detectors are mergers of binaries consisting of neutron stars (NSs) or black holes (BHs) [3]. If both objects in the binary are NSs (BNS), or if one is a NS and the other is a BH (a BHNS binary), then the tidal deformability of the NS will alter the GW signal in a way that is dependent upon the NS equation of state (EOS), allowing these observatories to constrain the EOS [16, 65, 72, 80, 94, 108, 116, 133, 156]. It is therefore of key importance to understand and model the influence of tidal effects on BNS and BHNS waveforms. We show here that a binary black hole (BBH) waveform can be augmented with PN tidal effects to accurately model a BNS system during the inspiral portion of the binary evolution. In principle, this method should also be applicable to BHNS systems.

BNS waveforms are typically computed using post-Newtonian (PN) methods, which are perturba-

tive expansions in the invariant velocity $v = (Md\phi/dt)^{1/3}$, where M is the total mass of the system and ϕ is the orbital phase (here we assume $c = G = 1$). For binaries consisting of nonspinning point particles, the expansion is known through 3.5PN order [49]. The static NS tidal effects first enter at 5PN order and depend upon the tidal deformability λ_i [155]. The parameter λ_i measures how much each NS i deforms in the presence of a tidal field, and depends on the NS mass and EOS implicitly through its dimensionless Love number $k_{2,i}$ and radius R_i : $\lambda_i = (2/3)k_{2,i}R_i^5$ [80]. As v increases throughout the inspiral, the missing 4PN, 4.5PN, and 5PN point-particle terms can result in the late portion of the PN waveform becoming inaccurate before the static tidal terms are large enough to contribute. For estimating the NS tidal deformability by using PN waveforms, the error introduced by neglecting the higher order PN terms can be as large as the statistical errors due to noise in the measured signals [77, 108, 156, 163].

Effective-one-body (EOB) models that include tidal effects [29, 34, 66] also include the merger, and provide better accuracy than PN by tuning higher-order vacuum terms to numerical relativity (NR) BBH waveforms. Although EOB has accurately reproduced waveforms from NR BNS simulations [29, 99], here we discuss a new and different approach that holds considerable promise for modeling tidal interactions during the inspiral.

The most accurate method of computing waveforms is carrying out full NR simulations for BNS and BHNS binaries; see [24, 25, 28–30, 81, 98, 99, 103, 120, 131, 133] for recent work. However, BNS and BHNS simulations are computationally challenging, since they require solving not only the full Einstein equations but also relativistic hydrodynamics with a realistic EOS. It is unfeasible to use NR hydrodynamic simulations alone to cover the parameter space given the wide range of theoretically possible EOS and NS masses. In contrast, BBH systems are easier to simulate with higher accuracy. Several large catalogs of BBH simulations and resulting waveforms have been compiled [17, 20, 63, 92, 93, 121, 145].

We introduce here a method we call “PN tidal splicing”, which generates BNS inspiral waveforms from NR BBH waveforms by adding tidal interactions derived in the PN formalism, effectively replacing the point-particle PN terms by the numerical BBH evolution.

We compare PN tidal splicing to NR using two simulations generated by SpEC [1], a code developed to evolve Einstein’s equations and general relativistic hydrodynamics [76, 82]. The first is a new equal-mass BNS simulation with 22 orbits before merger [86], and the neutron stars were initialized with gravitational masses $m_i \approx 1.64M_\odot$ and a polytropic EOS with $P = 123.6M_\odot^2\rho^2$, leading to a tidal deformability of $\lambda_i \approx 5.7 \times 10^{36} \text{g cm}^2 \text{s}^2$. The other is an equal-mass, nonspinning BBH simulation [40] tagged SXS:BBH:0180 in the public simulation catalog of the Simulating eXtreme Spacetimes Collaboration [145]. Using tidal splicing, we add tidal terms to the BBH waveform in an attempt to reproduce the BNS waveform. As a test, we also subtract tidal terms from the BNS waveform in an attempt to reproduce the BBH waveform.

Figure 3.1 shows that the GW phase difference, $|\delta\phi_{\text{GW}}|$, between the ‘BBH+tidal’ waveform and the BNS waveform is the same as the difference between the ‘BNS–tidal’ waveform and the BBH

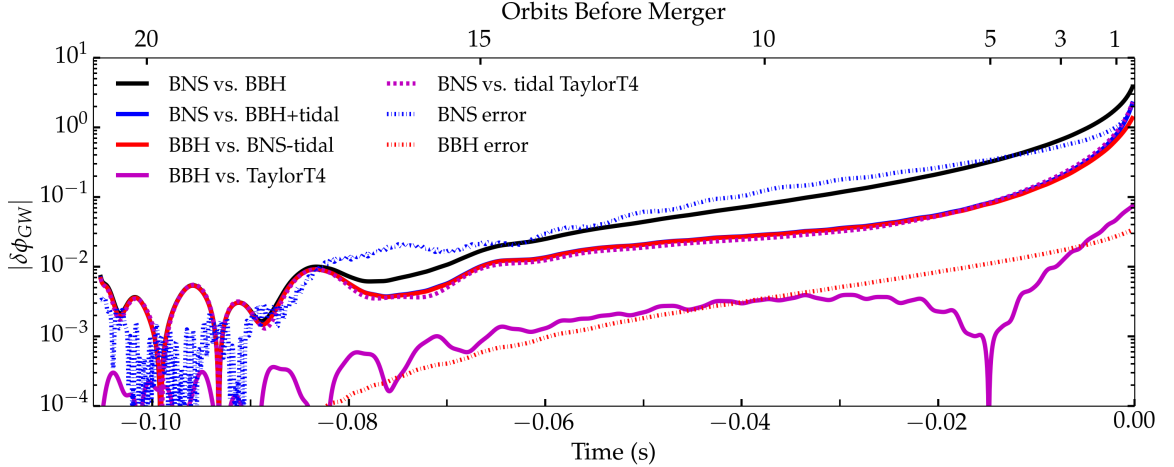


Figure 3.1: Phase difference between gravitational waveforms as a function of time, for an equal-mass binary of nonspinning compact objects. Differences are shown between BNS and BBH waveforms (black), between a BBH waveform with TaylorT4 tidal terms added and a BNS waveform (blue), and between a BNS waveform with TaylorT4 tidal terms subtracted and a BBH waveform (red). The red and blue curves nearly coincide. Also shown are the phase differences between BBH and point-particle TaylorT4 waveforms (solid magenta) and between BNS and tidal TaylorT4 waveforms (dashed magenta). The numerical error in the BBH waveform (dashed red) and an estimate of the error in the BNS waveform (dashed blue) are also shown. All waveforms are aligned with the BNS waveform according to [56]; the alignment time window encompasses a 5% change around a GW frequency of 280 Hz for a total mass of $M = 2 \times 1.64M_{\odot}$. The blue and red curves are smaller than the black curve by a factor of ~ 3 , demonstrating that tidal splicing can generate a BNS waveform from a BBH waveform and vice versa. The large error in the BNS waveform prevents us from fully measuring the accuracy of tidal splicing.

waveform, and both are a factor of ~ 3 smaller than the difference between the BNS and BBH waveforms throughout the inspiral. Thus we can mimic the inspiral of a full BNS simulation to within a few tenths of a radian at a fraction of the cost. For the BBH waveform, the phase error is estimated by the phase difference between the highest two resolutions. The BNS simulation is a combination of spectral and finite-volume methods with complicated convergence properties; it is unclear how to construct an accurate error measure [86]. We choose the simple prescription of plotting the phase difference between the highest two resolutions as a crude error estimate. While the BBH error estimate is small, the error estimate in the BNS simulation is as large as the tidal effects themselves. Therefore, we cannot yet fully verify the accuracy of tidal splicing until more accurate BNS simulations are available. Below (cf. Fig. 3.3) we will estimate the phase accuracy required of future BNS simulations for such verification.

3.3 Methods

For nonprecessing binaries, the PN equations for quasicircular orbits read

$$\frac{dv}{dt} = F(v), \quad (3.1)$$

$$\frac{d\phi}{dt} = v^3/M, \quad (3.2)$$

where $F(v)$ is the ratio of two functions, each known to finite PN order in v , and also depends on the binary's intrinsic parameters [43]. Different ways of evaluating these equations result in different PN approximants that agree to the same PN order in v , but diverge at higher orders. We present methods for tidal splicing using two different approximants.

TaylorT4

If $F(v)$ is expanded as a series in v and then truncated to the appropriate PN order, then the solution is known as the TaylorT4 approximant [58]. For TaylorT4, the tidal effects manifest as additional terms in the power series for $F(v)$. Equation (3.1) can be written

$$\frac{dv}{dt} = F(v) = F_{\text{pp}}(v) + F_{\text{tid}}(v), \quad (3.3)$$

where $F_{\text{pp}}(v)$ are the point-particle terms, and where the additional static tidal terms $F_{\text{tid}}(v)$ are known to 6PN order [155].

For inspiraling PN BBHs, $F(v)$ is governed by the point-particle terms. PN tidal splicing uses $\phi(t)$ from a BBH simulation together with Eqs. (3.3) and (3.2) [with $F_{\text{tid}}(v)$ set to zero] to compute an accurate version of $F_{\text{pp}}(v)$, which we will call $F_{\text{NR}}(v)$. To do this, we set $\phi(t) = \phi_{\text{GW}}/2$, where ϕ_{GW} is the GW phase of the $\ell = m = 2$ spherical-harmonic mode of the NR waveform. Then Eq. (3.2) yields

$$v(t) = \left(\frac{M}{2} \frac{d\phi_{\text{GW}}}{dt} \right)^{1/3}. \quad (3.4)$$

Given $v(t)$, we compute $F_{\text{NR}}(v) = dv/dt$ using finite differencing. Assuming $v(t)$ is monotonic, we can write $F_{\text{NR}}(v)$ as a single-valued function of v .

Using this $F_{\text{NR}}(v)$ in place of $F_{\text{pp}}(v)$ in Eq. (3.3), we then re-solve Eqs. (3.3) and (3.2), including the tidal terms $F_{\text{tid}}(v)$, to generate a waveform for a binary that includes tidal interactions. We express the orbital evolution of the new binary in terms of a new time coordinate \bar{t} . From the analytic expression for $F_{\text{tid}}(v)$ [155] and Eq. (3.3) we write a differential equation for \bar{t} :

$$\frac{d\bar{t}}{dv} = \frac{1}{F_{\text{NR}}(v) + F_{\text{tid}}(v)}. \quad (3.5)$$

Integrating this expression and inverting yields the function $v(\bar{t})$ corresponding to the spliced waveform.

The phase of the spliced waveform, $\bar{\phi}_{\text{GW}}(\bar{t})$, is computed by integrating Eq. (3.2):

$$\bar{\phi}_{\text{GW}}(\bar{t}) = \frac{2}{M} \int_{\bar{t}_{\text{min}}}^{\bar{t}} v(\bar{t})^3 d\bar{t}, \quad (3.6)$$

where \bar{t}_{min} is the start of the numerical waveform.

In TaylorT4, the amplitude of the waveform is a function of ν only, with no explicit time dependence [52]. So here we assume that the amplitude of the original NR waveform $A_{\text{NR}}(t)$ is likewise a function of ν only, so that we can write $A_{\text{NR}}(\nu) = A_{\text{NR}}(t(\nu))$. We then use $\nu(\bar{t})$ to express this amplitude in terms of \bar{t} . In other words, the amplitude of the resulting waveform is $\bar{A}(\bar{t}) = A_{\text{NR}}(t(\nu(\bar{t})))$. We generate a BBH waveform from a BNS waveform by the same method, except we subtract instead of add $F_{\text{tid}}(\nu)$ in the denominator of Eq. (3.5).

We require $\nu(t)$ to be monotonic so that $F(\nu)$ is single valued. To remove high-frequency numerical noise, the derivative in Eq. (3.4) is computed with a third order Savitzky-Golay filter [127] with a window size of $\approx 48.5 \mu\text{s}$. This is sufficient when adding tidal terms to the BBH waveform considered here. However, when testing our method by subtracting tidal terms from a BNS waveform, the phase of the BNS waveform considered here [86] has large enough oscillations in $\nu(t)$ that stronger smoothing is needed. We proceed by first subtracting the phase of the TaylorT4 waveform from that of the BNS waveform, expanding this difference in Chebyshev polynomials, truncating the Chebyshev expansion to $n = 35$, and adding back the phase of the TaylorT4 waveform. We find that the difference between the smoothed and unsmoothed phase of the BNS waveform is less than 3×10^{-3} radians.

As discussed above, Figure 3.1 displays the phase differences between NR and tidally spliced TaylorT4 waveforms. We now examine how well *pure* PN waveforms agree with NR waveforms. The magenta solid and dashed curves in Fig. 3.1 show phase differences between TaylorT4 and BNS or BBH waveforms. The point-particle TaylorT4 waveform does an excellent job of reproducing the phase evolution of the BBH waveform, about at the level of the BBH numerical error. However, while TaylorT4 is surprisingly accurate in the inspiral for equal-mass, nonspinning systems [58, 115], this does not hold true in general [90, 91, 148]. Tidal splicing should be applicable to an arbitrary BNS/BHNS system with spins and/or unequal masses, where there may not be an accurate PN approximant. References [108, 156] showed that uncertainties in the PN waveforms are one of the largest sources of error for tidal parameter estimation, and conclude that more accurate waveforms are needed.

TaylorF2

If Eqs. (3.1) and (3.2) are instead converted to the frequency domain (FD) using the stationary phase approximation before expanding the series, the approximant is called TaylorF2 [68]. TaylorF2 waveforms are expressed in the FD, and can be written

$$\tilde{h}(f) = \tilde{A}(f) \exp\left(i\tilde{\Psi}(f)\right), \quad (3.7)$$

where $\tilde{A}(f)$ is real and $\tilde{\Psi}(f)$ is the Fourier phase as a function of the GW frequency $f = \nu^3/(\pi M)$. For point particles, $\tilde{\Psi}(f) = \tilde{\Psi}_{\text{pp}}(f)$ is known for nonspinning systems to 3.5PN order [68, 69]. For tidally deformable objects, we write $\tilde{\Psi}(f) = \tilde{\Psi}_{\text{pp}}(f) + \tilde{\Psi}_{\text{tid}}(f)$, where $\tilde{\Psi}_{\text{tid}}(f)$ has been calculated up to 7.5PN order, with the exception of a few unknown constants [34, 65]. Here we include both 6PN tidal effects and 7.5PN tidal effects, setting the unknown constants to 0 as was done in [16].

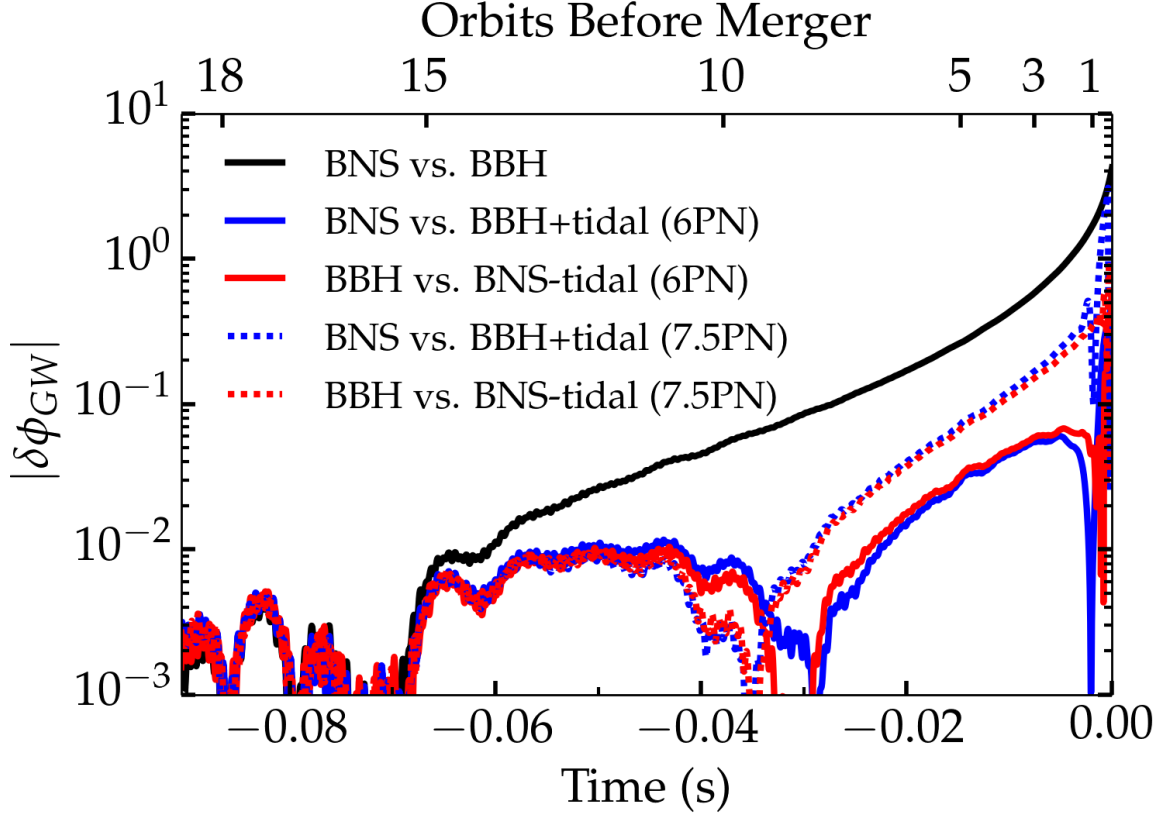


Figure 3.2: The phase difference $|\delta\phi_{\text{GW}}(t)|$ as a function of time for waveforms spliced with TaylorF2. Differences are shown between a BNS and a BBH waveform (black), between a BBH+tidal and a BNS waveform (blue), and between a BNS-tidal waveform and a BBH waveform (red) at the 6PN (solid) and 7.5PN (dot-dashed) orders. Only the time after the windowing function is shown here, resulting in a shorter time axis here than in Fig. 3.1. The late-time noise is an artifact caused by inverse Fourier transforming the unphysical high-frequency behavior of $\tilde{\Psi}_{\text{tid}}(f)$. At both PN orders, tidal splicing can generate a BNS waveform from a BBH waveform and vice versa.

To add the static tidal terms to an existing BBH waveform, first the Fourier transform of the waveform $\tilde{h}_{\text{NR}}(f)$ is computed. The early portion of the waveform is windowed using a Planck taper [117] while the merger and ringdown provide a natural windowing for the late portion. We then compute $\tilde{\Psi}_{\text{NR}}(f)$ and $\tilde{A}_{\text{NR}}(f)$ by decomposing according to Eq. (3.7). The spliced Fourier phase is then $\tilde{\Psi}(f) = \tilde{\Psi}_{\text{NR}}(f) + \tilde{\Psi}_{\text{tid}}(f)$. Because the known tidal terms do not affect the amplitude $\tilde{A}_{\text{NR}}(f)$, the new waveform is then

$$\tilde{h}(f) = \tilde{A}_{\text{NR}}(f) \exp\left(i \left[\tilde{\Psi}_{\text{NR}}(f) + \tilde{\Psi}_{\text{tid}}(f) \right]\right). \quad (3.8)$$

No smoothing of the numerical waveforms is needed for TaylorF2 splicing, unlike the TaylorT4 case.

Since the PN approximation breaks down for high frequencies, we impose a high frequency cutoff which we choose to be $f_{\text{ISCO}} = 1/(6^{3/2}\pi M) = 1338 \text{ Hz}$, the GW frequency corresponding to the

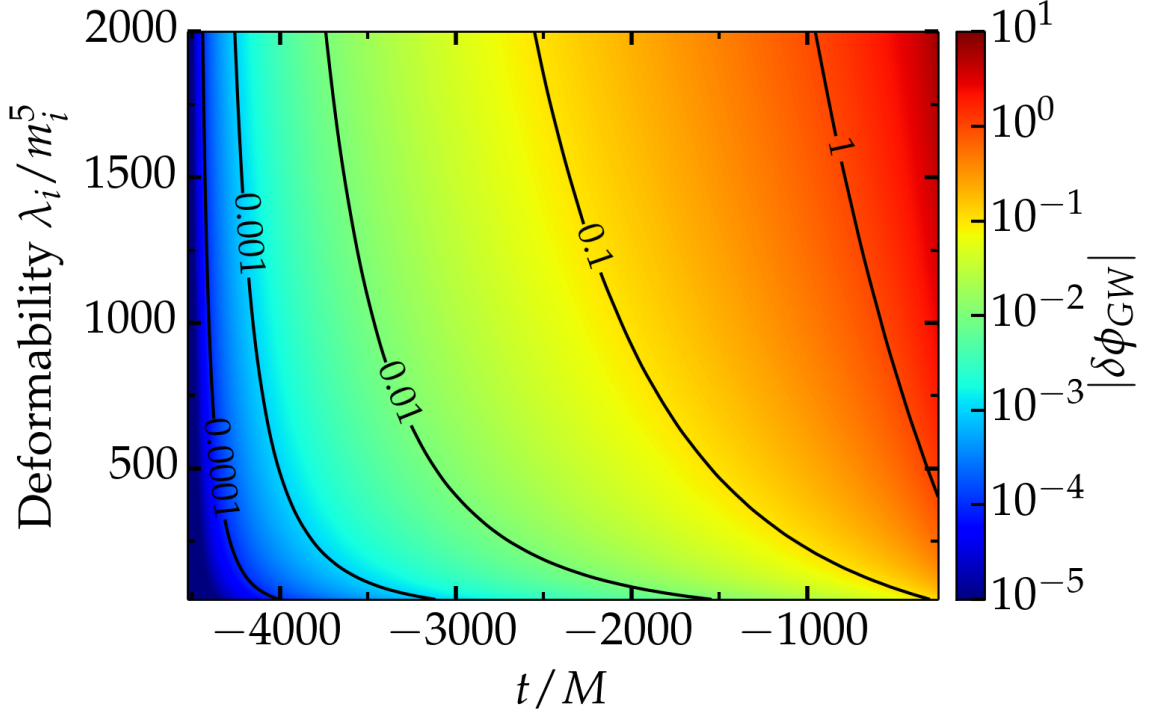


Figure 3.3: Phase difference between equal-mass, nonspinning BBH and ‘BBH+tidal’ waveforms. Each horizontal slice through this plot shows the phase difference as a function of time for a particular dimensionless deformability λ_i/m_i^5 . For our BNS simulation, $\lambda_i/m_i^5 \approx 453$. Contours show selected values of the phase difference. A BNS simulation starting at dimensionless time $t/M \approx -4500$ would need phase errors smaller than the values shown here in order to measure tidal effects. Even more accurate BNS simulations would be needed to measure the accuracy of the tidal splicing method.

innermost stable circular orbit of a Schwarzschild black hole of mass equal to the total mass of the system. It has been shown that for BNS systems, f_{ISCO} is approximately the merger frequency [31]. The starting frequency of the NR BNS waveform after windowing is ~ 285 Hz.

We estimate the error of the spliced waveforms by analyzing the phase differences in the time domain after taking the inverse Fourier transform. To avoid jump discontinuities in the Fourier phase, we roll off the effect of $\tilde{\Psi}_{\text{tid}}(f)$ from f_{ISCO} to $2 \times f_{\text{ISCO}}$ with a cosine window. While this will contaminate the higher frequency content, this should allow the lower frequencies of the inspiral to be mostly unaffected. After the inverse Fourier transform, the time domain waveforms are aligned in a 10% region around 300 Hz. The phase differences are shown in Fig. 3.2 and are similar to Fig. 3.1. With the exception of the last ~ 3 ms of the waveforms, which are affected by the high frequency contamination, all of the spliced waveforms maintain phase differences under 0.1 radians during most of the inspiral, below the difference between the BNS and BBH waveforms. It is not clear why the 6PN terms approximate the tidal effects better than the 7.5PN terms; it may be because we zero the unknown constants in the 7.5PN expression.

3.4 Discussion

We have shown that PN tidal splicing of BBH waveforms can produce inspiral waveforms for non-spinning BNS systems. This method should easily generalize to objects with spins and to BHNS systems. Once a BBH waveform is generated for a particular mass ratio and spin configuration, it should be easy to produce BNS/BHNS waveforms via PN tidal splicing for any EOS simply by adjusting the tidal parameters λ_i , allowing the entire tidal parameter space for inspiral waveforms to be spanned.

The accuracy of this method is limited by that of the PN tidal terms. In particular, additional finite size effects not captured by the current static tidal PN terms can influence waveform amplitude and phase, and dynamical tidal effects can also contribute to the phase evolution [95], especially as the NSs approach merger. This method in principle can be improved with better PN tidal terms. Unfortunately, it is currently difficult to fully measure the accuracy of tidal splicing until higher-accuracy many-orbit BNS simulations are available for multiple masses and EOS.

Figure 3.3 estimates the accuracy needed for equal mass, nonspinning BNS simulations to see the tidal effects on the inspiral phase of the waveform. Even smaller BNS errors would be necessary to constrain the accuracy of tidal splicing. We chose the start time in Fig. 3.3 so that the inspiral spans a large enough frequency range for aLIGO to recover 97% of the information about λ_i , according to the analysis presented in Fig. 3 of [65]. We assume $M = 2.8M_\odot$ (corresponding to a prototypical NS mass of $1.4M_\odot$) and an upper frequency cutoff of f_{ISCO} .

An alternative to computing tidal terms to a higher PN order is to resum them in some way, as is done in [29, 33, 99] in the context of EOB. It is not clear how to do this with tidal splicing.

Additionally, the merger/ringdown cannot be modeled with splicing alone, especially for BNS mergers and BHNS systems that undergo tidal disruption. One possibility is to combine an analytic waveform in the very early inspiral with a spliced BBH waveform in the mid to late inspiral and then with a waveform from a full hydrodynamical simulation for the merger and ringdown, to create a “tribridized” waveform. This might reduce the need for expensive hydrodynamical simulations lasting many orbits. If necessary, surrogate models [40, 78, 130] that cover the parameter space including the EOS can be forged from spliced BBH waveforms.

3.5 Acknowledgments

We thank Harald Pfeiffer and Sanjay Reddy for helpful discussions. This work was supported in part by the Sherman Fairchild Foundation and NSF Grants No. PHY-1404569 and No. AST-1333520 at Caltech, NSF Grant No. AST-1333142 at Syracuse University, the Sherman Fairchild Foundation and NSF Grants No. PHY-1306125 and No. AST-1333129 at Cornell University and by NASA through Einstein Postdoctoral Fellowship Grant No. PF4-150122 awarded by the Chandra X-ray Center, which is operated by the Smithsonian Astrophysical Observatory for NASA under Contract No. NAS8-03060. Computations were performed on the Zwicky cluster at Caltech, which is supported by the Sherman Fairchild Foundation and by NSF Grant No. PHY-0960291; on the

NSF XSEDE network under Grant No. TG-PHY990007N; on the NSF/NCSA Blue Waters at the University of Illinois with allocation jr6 under NSF PRAC Grant No. ACI-1440083; and on the GPC supercomputer at the SciNet HPC Consortium [113]; SciNet is funded by the Canada Foundation for Innovation (CFI) under the auspices of Compute Canada; the Government of Ontario; Ontario Research Fund (ORF)–Research Excellence; and the University of Toronto.

TIDAL SPLICING FOR BHNS AND BNS SYSTEMS

4.1 Introduction

In August 2017, the network of interferometers consisting of aLIGO [2] and VIRGO [14] first observed the gravitational radiation from the merging of Binary Neutron Stars (BNS) [13], opening the door to exploring extremely compact objects other than Binary Black Holes (BBH). Coincident detection with the electromagnetic observational counterpart GRB 170817A [4], show these systems are the progenitors of short gamma-ray bursts, and herald the start of multi-messenger astronomy. Additionally, this detection served as a probe of the neutron star equations-of-state (EOS) [13, 132], and provided constraints on gravitational wave speed [4]. As the detectors' sensitivity improve, observing more such systems will improve future analyses, further constraining the governing physics [72, 107]. However, capturing all of the information within the incoming signals requires detailed, accurate templates which precisely describe waveforms from BNS or Black Hole-Neutron Star (BHNS) systems.

The ideal solution would be to run full numerical simulations to generate the gravitational waveforms. Running simulations which incorporate the relevant matter physics for BHNS/BNS is a field of active development [75, 81, 83, 86, 95, 97, 103, 109, 114]. However, extending the parameter space to include all allowable EOS means an even larger number of simulations will be required to span the range of possible systems. Then there is the computational cost of resolving the behavior of the matter, making these simulations both resolution limited and prohibitively expensive, and thus impractical for parameter estimation purposes.

On the other hand, numerical simulations of BBH systems has made great strides over the recent years, generating waveforms across significant portions of the parameter space, and the rise of surrogate models of the simulations effectively allow interpolation of waveforms across different regions of parameter space [40–42, 78, 129, 154]. Ref [154] showed that surrogate models can robustly generate faithful representations of these binary evolutions for spinning black holes with $\chi_A < .8$.

Another approach to generate BHNS and BNS waveforms is to create analytic and phenomenological models which capture the behavior of BHNS and BNS systems, often in the form of additional corrections to BBH waveform models. Within the Post-Newtonian (PN) formalism, Ref [155] first computed the leading order tidal effects on the orbital evolution, characterized by the static quadrupolar tidal deformability, $\bar{\lambda}_2$. Extensions to the Effective One-Body (EOB) model SEOB-NRv4 [53], including additional static higher order effects [24, 34, 73, 144], led to the time domain model SEOBNRv4T [96, 144].

The LEA+ model [107] is a frequency domain waveform model calibrated to a series of BHNS sim-

ulations with mass ratios of $q > 2$ [109] as an enhancement to the SEOBNRv2 model [150]. While LEA+ is a full waveform model, it is only valid over the limited parameter space the simulations it used to calibrate it, *i.e.* $q > 2$.

The frequency domain models, SEOBNRv4_ROM_NRTidal, PhenomD_NRTidal, and PhenomPv2_NRTidal [74] are the combination of the SEOBNRv4_ROM [53], PhenomD [101, 104], and PhenomPv2 [142, 143], with the NRTidal model [75], which is a phenomenological fit of BNS/BHNS simulation data to PN-like coefficients. While these models cover a wide range of BNS parameter space, they calibrated the fits to a limited number of waveforms and seem to overestimate the tidal effects during the inspiral [74].

We propose a hybrid method called ‘Tidal Splicing’ [27] which bridges the gap between the accurate yet expensive numerical simulations with the cheap yet limited PN approximations in generating inspiral waveforms for BNS/BHNS. The main conceit of Tidal Splicing is to leverage the accuracy of the numerical BBH simulations with the cheap PN terms known for tidally deformable systems to efficiently generate waveforms for BNS systems. This method does so by decomposing the numerical BBH waveform in a manner akin to the PN formalism and using those numerical results to replace their corresponding analytic PN expansion. We combine that expression with the analytic tidal PN terms to build up a full waveform which replicates the inspiral of a BNS/BHNS, limited primarily by the knowledge of the PN tidal analytics fed in.

In this paper, we continue the development of Tidal Splicing by extending the method to spinning systems and spherical harmonic modes beyond the (2,2) mode. Due to newly available EOB models which incorporate higher PN effects, we also extend the known higher order tidal effects from EOB to the time domain PN approximants. Since recent work suggests that the choice of which BBH template we use as the base for tidal waveforms can impact on parameter estimation [61], we will use the hybridized surrogate model ‘NRHybSur3dq8’ [154] as our BBH base.

We organize this paper as follows: in Sec 4.2 we summarized the current existing work on time domain tidal waveforms in the PN framework; in Sec 4.3 we discuss how we partially extend the PN tidal approximants to 2.5PN order and how we correct the dynamical tides effects for spinning NS; in Sec 4.4 we explain our method of tidal splicing; in Sec 4.5 we compare tidal splicing with some recent BHNS and BNS simulations.

Except where otherwise noted, we shall use the subscripts A, B to refer to the individual NS or BH objects, the subscripts $\ell = 2, 3, \dots$ refer usually to the specific polar mode of the tidal effect in consideration (*i.e.* 2=quadrupolar, 3=octopolar, ect.), while the ℓ, m superscripts will typically correspond to the spherical harmonic modes. We chose units of $G = c = 1$. For convenience, we have included a definitions key within Appendix 4.6.

4.2 Post-Newtonian Theory

The PN approximation describes the binary’s orbital behavior as series expansions that are valid in the slow-moving, weak-field regime. The expansion parameter is the characteristic velocity of the

inspiraling objects, v (another common parameter is $x = v^2$). We denote an expansion term of order $\mathcal{O}(v^n)$ by the label $\frac{n}{2}$ PN (e.g. 2.5PN corresponds to v^5 beyond leading order). A more detailed summary of PN theory as it pertains to BBH systems can be found in [44].

We start with a quasi-circular binary system of a pair compact objects with component masses, m_A and m_B , with total mass M , and spins aligned with the orbital angular momentum, χ_A, χ_B , where $\chi_A = S_A/m_A^2$. The mass ratio q we define as the larger mass over the smaller mass, m_A/m_B so that $q \geq 1$. For convenience, we also define the mass fractions, $X_A = m_A/M$, and symmetric mass ratio $\nu = X_A X_B$.

Orbital Evolution

Two equations govern the evolution of the quasi-circular binary system in PN theory. The first relates the orbital phase ϕ to ν by a correspondence with the orbital frequency, ω ,

$$\omega = \frac{d\phi}{dt} = \frac{v^3}{M}. \quad (4.1)$$

The other equation is the energy balance equation as the emission of gravitational radiation drives the adiabatic evolution by bleeding away the orbital energy, $E(v)$. If the energy flux is given by $F(v)$, then this energy balance equation is

$$\frac{dE(v)}{dt} = -F(v). \quad (4.2)$$

When the objects are not simply black holes, but extended objects like neutron stars, the physical matter of the object responds to the changing tidal fields. The leading tidal effects are the result of the deformation of the NS due to the tidal field generated by the other object in the binary. This effect is characterized by the dimensionless ℓ -polar tidal deformability parameter, $\bar{\lambda}_\ell$. Other commonly used parameters are dimensionful tidal parameter λ_ℓ or the tidal love number k_ℓ , and are related to $\bar{\lambda}_\ell$ by the NS radius R_A or compactness $C_A = m_A/R_A$ according to

$$\bar{\lambda}_{\ell A} = \frac{2}{(2\ell - 1)!!} \frac{k_{\ell A}}{C_A^{2\ell+1}} = \frac{\lambda_{\ell A}}{m_A^{2\ell+1}}. \quad (4.3)$$

As each object in the binary can have its own deformability, we add the subscript A, B to specify the particular object.

The quadrupolar tidal deformability $\bar{\lambda}_2$ enters $E(v)$ and $F(v)$ first at 0PN as a $\mathcal{O}(v^{10})$ term and were first computed to 1PN as additive corrections to the energy and flux expressions [80, 155]. While normally such high order effects would be neglected, the relatively large size of $\bar{\lambda}_2 \sim \mathcal{O}(1000)$ suggest the tidal deformations impact the waveform earlier in the inspiral than expected by their formal PN order.

Ref [155] provides the energy and flux expansions to 1PN,

$$E(v) = -\frac{\nu v^2}{2} \left[1 + \left(-\frac{3}{4} - \frac{\nu}{12} \right) v^2 + \mathcal{O}(v^3) \right] + \bar{\lambda}_{2A} v^{10} X_A^4 \left(9(-1 + X_A) \right)$$

$$+ \frac{11}{2} \left(-3 + X_A - X_A^2 + 3X_A^3 \right) v^2 + \mathcal{O}(v^3) \Big] + (A \rightarrow B) \Big], \quad (4.4)$$

$$F(v) = \frac{32v^2v^{10}}{5} \left[1 + \left(-\frac{1247}{336} - \frac{35}{12}v \right) v^2 + \mathcal{O}(v^3) + \bar{\lambda}_{2A} v^{10} X_A^4 \left(6(3 - 2X_A) \right. \right. \\ \left. \left. + \frac{1}{28} \left(-704 - 1803X_A + 4501X_A^2 - 2170X_A^3 \right) v^2 + \mathcal{O}(v^3) \right) + (A \rightarrow B) \right]. \quad (4.5)$$

TaylorT Approximants

We can now insert the energy and flux expressions into the orbital evolution (Eq 4.1) and energy balance (Eq 4.2) equations and evolve them to describe the binary's evolution. There are many choices in how to expand the energy balance and orbital evolution equations giving rise to a family of different PN approximants. All the variants agree to the same formal PN order but have different higher order truncations. The two which we will examine here are usually referred to as TaylorT4 and TaylorT2.

Now in the process of formally expanding the energy and flux, naively treating the tidal informations at their formal PN order means we would truncate those terms out in the expansion when the first unknown BBH terms arise, *i.e.* before the v^{10} terms show up. To ensure they do not disappear, and in light of the fact that $\bar{\lambda}_2$ is large, we handle the leading tidal terms as if they were the same order as the leading PN terms: $\mathcal{O}(1) \sim \mathcal{O}(\bar{\lambda}_2 v^{10})$ [155]. (See in the Appendix 4.6 for further discussion regarding this correspondence in PN orders.) In the expansions below we then keep all terms up through 1PN beyond these leading order effects.

TaylorT4

The TaylorT4 [58] method generates the orbital evolution by rewriting the energy balance equation as

$$\frac{dv}{dt} = -\frac{F(v)}{M \frac{dE(v)}{dv}}, \quad (4.6)$$

then expanding the ratio on the right hand side as a power series in v truncated to the appropriate order, so that,

$$\frac{dv}{dt} = \mathcal{F}_{\text{BBH}}(v) + \mathcal{F}_{\text{Tid}}(v), \quad (4.7)$$

Here, we have broken the series into 2 parts: the terms corresponding to a BBH system in \mathcal{F}_{BBH} (*i.e.* $\bar{\lambda}_2 = 0$) and the terms corresponding to the tidal correction in \mathcal{F}_{Tid} . We don't reproduce \mathcal{F}_{BBH} here (as they aren't needed for our methods), but \mathcal{F}_{Tid} to 1PN order is [155],

$$\mathcal{F}_{\text{Tid}}(v) = \frac{32v^9}{5M} \left[\bar{\lambda}_{2A} X_A^4 v^{10} \left(72 - 66X_A + \left(\frac{4421}{56} - \frac{12263X_A}{56} + \frac{1893X_A^2}{4} - \frac{661X_A^3}{2} \right) v^2 \right) \right. \\ \left. + (A \rightarrow B) \right]. \quad (4.8)$$

The TaylorT4 method computes the quantity $v(t)$ by integrating Eq 4.7, then computes the orbital phase by integrating,

$$\frac{d\phi}{dt} = v^3/M. \quad (4.9)$$

The two constants arising from integrating both equations correspond to the inherent freedom to choose the initial time and phase of the waveform.

TaylorT2

The TaylorT2 [68] expansion begins at the same point as TaylorT4 with the PN energy equation and definition of v , except rearranging to get the pair of integral expressions parametric in v ,

$$t(v) = t_0 + M \int \frac{dE(v)}{F(v)} dv, \quad (4.10)$$

$$\phi(v) = \phi_0 + \int v^3 \frac{dE(v)}{F(v)} dv. \quad (4.11)$$

The integration constants t_0 and ϕ_0 are both freely specifiable, and can be used to set the initial time and phase of the resulting waveform.

The energy/flux ratio are expanded as a power series then integrated to get series expressions for both the time and phase, which we break into a part corresponding to BBH system and a part of comprised of all the additional tidal effects,

$$t(v) = t_0 + \mathcal{T}_{\text{BBH}}(v) + \mathcal{T}_{\text{Tid}}(v), \quad (4.12)$$

$$\phi(v) = \phi_0 + \mathcal{P}_{\text{BBH}}(v) + \mathcal{P}_{\text{Tid}}(v). \quad (4.13)$$

As before, we do not show \mathcal{T}_{BBH} or \mathcal{P}_{BBH} , but the 1PN tidal terms are

$$\begin{aligned} \mathcal{T}_{\text{Tid}}(v) = & -\frac{5M}{256v^8} \left[\bar{\lambda}_{2A} X_A^4 v^{10} \left(288 - 264X_A + \left(\frac{3179}{4} - \frac{919X_A}{4} - \frac{1143X_A^2}{2} + 65X_A^3 \right) v^2 \right) \right. \\ & \left. + (A \rightarrow B) \right], \end{aligned} \quad (4.14)$$

$$\begin{aligned} \mathcal{P}_{\text{Tid}}(v) = & -\frac{1}{32v^5} \left[\bar{\lambda}_{2A} X_A^4 v^{10} \left(72 - 66X_A + \left(\frac{15895}{56} - \frac{4595X_A}{56} - \frac{5715X_A^2}{28} + \frac{325X_A^3}{14} \right) v^2 \right) \right. \\ & \left. + (A \rightarrow B) \right]. \end{aligned} \quad (4.15)$$

BBH Strain Modes

The gravitational radiation emission pattern for distant observers can be represented via a decomposition into spin-weighted spherical harmonics. Following the PN formalism used in [52], we express the strain from a BBH system as,

$$h_{\text{BBH}}^{\ell m}(t) = \frac{2v^2 M}{r} \sqrt{\frac{16\pi}{5}} H^{\ell m}(v) e^{-im\psi(v)}, \quad (4.16)$$

where r is the distance from the source to the detector. The various terms of $H^{\ell m}(v)$ are complex series expansions of the individual modes and are distinct from the series expansions for the energy and flux from above. $\Psi(v)$ is the tail-distorted orbital phase variable [18, 46]

$$\Psi(v) = \phi(v) - 2M\omega \ln\left(\frac{\omega}{\omega_0}\right). \quad (4.17)$$

The constant ω_0 is the reference frequency, often chosen to be the frequency the waveform enters the detector's frequency band. This tail-distorted difference between ϕ and Ψ comes in as a 4PN order correction to the phase [18].

To see why it is a 4PN correction, we consider

$$\frac{d\Psi}{dt} = \frac{v^3}{M} - 6\left(1 + \ln\left(\frac{v^3}{M\omega_0}\right)\right)v^2 \frac{dv}{dt}, \quad (4.18)$$

where we used Eq 4.1. Now from the TaylorT4 expansion, we know that the leading order term in the series expansion of $\frac{dv}{dt}$ enters at v^9 , so then

$$\frac{d\Psi}{dt} = \frac{v^3}{M} \left(1 + \mathcal{O}(v^8)\right) \approx \frac{d\phi}{dt}. \quad (4.19)$$

Beacuse 4PN terms are higher order than anything we consider, we can ignore the tail-distortion term for our work here and let $\Psi(v) = \phi(v)$.

Examining the expression for $H^{22}(v)$ [52], we see that the first complex terms enter at 2.5PN order. Following the concepts used in [106], we approximate that imaginary amplitude term as a phase correction as follows,

$$\begin{aligned} H^{22}(v)e^{-2i\phi(v)} &= A_{\text{BBH}}^{22}(v)(1 + iv^5\delta + \mathcal{O}(v^6))e^{-2i\phi(v)} \\ &\approx A_{\text{BBH}}^{22}(v)e^{iv^5\delta}e^{-2i\phi(v)}, \end{aligned} \quad (4.20)$$

where δ is the imaginary 2.5PN coefficient of $H^{22}(v)$ and $A_{\text{BBH}}^{22}(v) = |H^{22}(v)|$. Thus, this correction to $\phi(v)$ is similar to the tail-distorted term, but at a higher PN order (δ here corresponds to a 5PN phase term), and thus can be ignored by the same arguments as above. The (2,2) mode can then be expressed entirely as an amplitude and phase,

$$h_{\text{BBH}}^{22}(v) = A_{\text{BBH}}^{22}(v)e^{-2i\phi(v)}. \quad (4.21)$$

The complex terms in $H^{\ell m}$ in remaining modes have complex terms arising at lower relative PN order than for the (2,2) mode [52]. We introduce real functions $A_{\text{BBH}}^{\ell m}(v)$ and $\psi_{\text{BBH}}^{\ell m}(v)$ such that we can express the strain modes as amplitudes and phases,

$$h_{\text{BBH}}^{\ell m}(v) = A_{\text{BBH}}^{\ell m}(v)e^{i(\psi_{\text{BBH}}^{\ell m}(v) - m\phi)}. \quad (4.22)$$

For the (2,2) mode, we have $\psi_{\text{BBH}}^{22}(v) = 0$.

Tidal Correction to Strain

Ref [24] computed the leading order PN tidal corrections to the strain modes (explicitly written out in the form we use here in Eq (A14-A17) of [65]). There are no corrections to the phase of the individual modes at leading order, (*i.e.* $\psi_{\text{Tid}}^{\ell m}(v) = 0$), so the leading order corrections can be represented as additive corrections to the strain amplitude,

$$\begin{aligned}
A_{\text{Tid}}^{22}(v) &= \left| 24 \sqrt{\frac{\pi}{5}} v^{12} \bar{\lambda}_{2A} X_A^5 (3 - 5X_A + 2X_A^2) (1 + \alpha_{2A}^{22} v^2 + \alpha_{4A}^{22} v^4) + (A \rightarrow B) \right|, \\
A_{\text{Tid}}^{21}(v) &= \left| 8 \sqrt{\frac{\pi}{5}} v^{13} \bar{\lambda}_{2A} X_A^5 \left(\frac{9}{2} - 15X_A + \frac{33X_A^2}{2} - 6X_A^3 \right) (1 + \alpha_{2A}^{21} v^2) - (A \rightarrow B) \right|, \\
A_{\text{Tid}}^{33}(v) &= \left| 108 \sqrt{\frac{3\pi}{14}} v^{13} \bar{\lambda}_{2A} X_A^5 (1 - 2X_A + X_A^2) (1 + \alpha_{2A}^{33} v^2) - (A \rightarrow B) \right|, \\
A_{\text{Tid}}^{31}(v) &= \left| 12 \sqrt{\frac{\pi}{70}} v^{13} \bar{\lambda}_{2A} X_A^5 (1 - 2X_A + X_A^2) (1 + \alpha_{2A}^{31} v^2) - (A \rightarrow B) \right|, \tag{4.23}
\end{aligned}$$

where $\alpha_i^{\ell m}$ are the coefficients corresponding to the v^i higher order corrections to the strain modes. The term α_2^{22} is

$$\alpha_{2A}^{22} = \frac{-202 + 560X_A - 340X_A^2 + 45X_A^3}{42(3 - 2X_A)}, \tag{4.24}$$

while the rest of the $\alpha_i^{\ell m}$ are currently not known. The corrections arising from the other $A_{\text{Tid}}^{\ell m}$ enter at higher PN orders.

Take care to note that there is a sign flip when switching from object A to B for the $m = \text{odd}$ modes; this is because in the limit the two objects have the same parameters, there is nothing to break the symmetry for the $m = \text{odd}$ modes, and thus the tidal amplitude to those modes vanishes. This is akin to how BBH waveforms of equal mass, nonspinning systems have vanishing $m = \text{odd}$ modes because of symmetry arguments.

The strain modes for systems with tidally deformed objects are then,

$$h_{\text{Tid}}^{\ell m}(t) = \left(A_{\text{BBH}}^{\ell m}(v) + A_{\text{Tid}}^{\ell m}(v) \right) e^{i(\psi_{\text{BBH}}^{\ell m}(v) - m\phi(v))}. \tag{4.25}$$

Dynamical Tides

In addition to the NS static deformation, the objects also have internal f -modes given by the resonant frequencies $\omega_{f\ell}$. As the orbital frequency approaches $\omega_{f\ell}$, the tides become dynamical and not simply proportional to the instantaneous tidal field. Ref [73, 144] analyzed how these dynamical tides affected the orbital motion was explored in. The approximate solution they derive treats the dynamical tidal deformabilities as frequency dependent scalings of their static values. We utilize their results, slightly expanding them to account for the case which the resonating object is spinning.

In effect the dynamical tides serves primarily as an amplification to the static deformability during the evolution, peaking when the orbital frequency is on resonance with one of the object's internal

f -modes, $\omega_{f\ell A}$. We shall also make use of the dimensionless f -mode resonance frequency,

$$\bar{\omega}_{f\ell A} = M\omega_{f\ell A}. \quad (4.26)$$

Note that our choice of defining $\bar{\omega}_{f\ell A}$ by scaling it as the binary's total mass M , rather than the object mass m_A as other works often use, is for our convenience when comparing with the dimensionless orbital frequency, $\bar{\omega} = M\omega$.

In the nonspinning case, we denote the characteristic parameter governing the resonance as

$$\gamma_{\ell A} = \frac{\ell\omega}{\omega_{f\ell A}} = \frac{\ell v^3}{\bar{\omega}_{f\ell A}} \quad (4.27)$$

to characterize how close the system is to resonance.

There are two different correction factors, one for the phase evolution and one for the strain amplitudes. Ref [144] expressed the effective enhancement factor $\kappa_{\ell A}(v)$ on the static deformability of object A for the orbital phase evolution by

$$\kappa_{\ell A}(v) = a_\ell + b_\ell \left[\frac{1}{1 - \gamma_{\ell A}^2} + \frac{4}{3\sqrt{\epsilon_\ell} \hat{t}_\ell \gamma_{\ell A}^2} + \sqrt{\frac{\pi}{3\epsilon_\ell}} \frac{Q_\ell}{\gamma_{\ell A}^2} \right], \quad (4.28)$$

where

$$\begin{aligned} \epsilon_\ell &= \frac{256v\omega_{f\ell A}^{5/3}}{5\ell^{5/3}}, \\ \hat{t}_\ell &= \frac{8}{5\sqrt{\epsilon_\ell}} \left(1 - \gamma_{\ell A}^{-5/3} \right), \\ Q_\ell &= \cos\left(\frac{3\hat{t}_\ell}{8}\right) \left[1 + 2F_S\left(\frac{\sqrt{3}}{2\sqrt{\pi}}\hat{t}_\ell\right) \right] - \sin\left(\frac{3\hat{t}_\ell}{8}\right) \left[1 + 2F_C\left(\frac{\sqrt{3}}{2\sqrt{\pi}}\hat{t}_\ell\right) \right], \end{aligned} \quad (4.29)$$

with F_S and F_C as the Fresnel sine and cosine integrals. The coefficients (a_ℓ, b_ℓ) are given by $(a_2, b_2) = (1/4, 3/4)$ and $(a_3, b_3) = (3/8, 5/8)$. The PN orbital evolution Eq 4.40, 4.42 incorporate the dynamical tides by taking $\bar{\lambda}_{\ell A} \rightarrow \bar{\lambda}_{\ell A} \kappa_{\ell A}(v)$.

In [73], the correction to the strain amplitudes is,

$$\hat{\kappa}_{2A}(v) = \frac{(\kappa_{2A}(v) - 1)\omega_{f2A}^2 + 6(1 - X_A)\kappa_{2A}\omega^2}{(9 - 6X_A)\omega^2}. \quad (4.30)$$

Similar to the orbital evolution, the dynamical strain amplification follows the replacement rule $\bar{\lambda}_{2A} \rightarrow \bar{\lambda}_{2A} \hat{\kappa}_{2A}(v)$ in Eq 4.23.

Note that these replacement rules are not proper power series expansions of v , because the Fresnel formula do not have a well defined power series expansion about $v = 0$ (even though those terms vanish as $v \rightarrow 0$, they also oscillate infinitely fast). So including $\kappa_{\ell A}(v)$ and $\hat{\kappa}_{2A}(v)$ into the evolution and strain formula means the tidal effects can not be represented to an exact, formal PN order. While this is not a problem for the actual generation of the waveforms, it does mean that the differences between the spliced waveforms and the inspiral of true BHNS/BNS systems no longer falls along a well defined PN order.

4.3 Expanding PN Tidal Corrections

Partial 2.5PN Tidal Terms

While [155] introduced the static quadrupolar deformability corrections to the orbital evolution to 1PN order, higher order terms have also been introduced within the EOB formalism. Not only do they include nonspinning $\bar{\lambda}_2$ tidal corrections to the energy (through the EOB Hamiltonian) up to 2PN order, but corrections according to the static octopolar deformability $\bar{\lambda}_3$ as well [34]. Their expressions just have terms up through 2PN, but because the tidal effects only enter at full PN orders, the first unknown terms enter at 3PN meaning the 2.5PN tidal coefficients are 0. These effects are already in use both within SEOBNRv4T [96, 144], and for the frequency domain approximant TaylorF2 [65]. We expand the EOB results to obtain the time domain Taylor approximants here.

The details of how to convert those terms to PN energy coefficients are given in the Appendix 4.6. From that, we know the PN energy expression for a tidally deformed system is

$$E_{\bar{\lambda}_2}(v) = -\frac{\nu v^2}{2} \left[\bar{\lambda}_{2A} v^{10} X_A^4 \left(9(-1 + X_A) + \frac{11}{2} (-3 + X_A - X_A^2 + 3X_A^3) v^2 \right. \right. \\ \left. \left. + \frac{13}{2} \left(\frac{51}{4} + \frac{15}{4} X_A - \frac{361}{42} X_A^2 - \frac{47}{21} X_A^3 - \frac{47}{12} X_A^4 - \frac{7}{4} X_A^5 \right) v^4 + \mathcal{O}(v^6) \right) + (A \rightarrow B) \right], \quad (4.31)$$

$$E_{\bar{\lambda}_3}(v) = -\frac{\nu v^2}{2} \left[\bar{\lambda}_{3A} v^{14} X_A^6 \left((13 - 13X_A) + \frac{5}{2} (-3 + 35X_A - 19X_A^2 - 13X_A^3) v^2 \right. \right. \\ \left. \left. + \frac{17}{4} \left(\frac{73}{6} + \frac{49}{2} X_A - \frac{5}{9} X_A^2 + 23X_A^3 - \frac{307}{6} X_A^4 - \frac{143}{18} X_A^5 \right) v^4 + \mathcal{O}(v^6) \right) + (A \rightarrow B) \right]. \quad (4.32)$$

From here we can see that the leading order octopolar deformability terms enter as $\mathcal{O}(v^{14})$ terms. Numerically, $\bar{\lambda}_3$ is typically larger than $\bar{\lambda}_2$, with $\bar{\lambda}_3 \sim \mathcal{O}(1000 - 10000)$. Thus, similar to $\bar{\lambda}_2$, we treat the leading order $\bar{\lambda}_3$ terms to the same formal order as the leading order PN terms, *i.e.* $\mathcal{O}(1) \sim \mathcal{O}(\bar{\lambda}_2 v^{10}) \sim \mathcal{O}(\bar{\lambda}_3 v^{14})$. Terms for both deformabilities are computed up until the first unknown terms at 3PN (again, the energy 2.5PN terms vanish).

Unfortunately, the flux information is incomplete up through that same PN order. We shall introduce undefined coefficients for the missing terms, $\alpha_4, \beta_0, \beta_2, \beta_4$ so that we may expand the PN expressions to a consistent order. We write the flux terms as

$$F_{\bar{\lambda}_2}(v) = \frac{32\nu^2 v^{10}}{5} \left[\bar{\lambda}_{2A} v^{10} X_A^4 \left(6(3 - 2X_A) + \frac{1}{28} (-704 - 1803X_A + 4501X_A^2 - 2170X_A^3) v^2 \right. \right. \\ \left. \left. + \alpha_4 v^4 + \mathcal{O}(v^6) \right) + (A \rightarrow B) \right], \quad (4.33)$$

$$F_{\bar{\lambda}_3}(v) = \frac{32\nu^2 v^{10}}{5} \left[\bar{\lambda}_{3A} v^{14} X_A^6 \left(\beta_0 + \beta_2 v^2 + \beta_4 v^4 + \mathcal{O}(v^6) \right) + (A \rightarrow B) \right]. \quad (4.34)$$

We hang onto the undefined coefficients, $\alpha_4, \beta_0, \beta_2, \beta_4$ for the purposes of completeness; when the value of those coefficients are computed, those values can simply substituted into the flux expression and the Taylor expansions of the orbital evolution below.

For aligned spin systems, there will also be terms corresponding due to spin-tidal terms, interactions in the Hamiltonian between object spins and the tidal deformations of the NS. The spin-tidal

connection terms are not included in our expansions because of discrepancies in the calculation of the leading order 1.5PN coefficients; a discussion of those coefficients, including how to add them when those discrepancies are resolved, can be found in the Appendix 4.6.

To complete the PN energy and flux, we need to include the dynamics of BBH systems with object spins χ_A, χ_B aligned with the orbital angular momentum, and rotationally induced quadrupole moments \bar{Q}_A, \bar{Q}_B . (Though $\bar{Q}_{BH} = 1$, we allow it to take on arbitrary values in order to extend to general systems). The dimensionless \bar{Q}_A is related the dimensional version by

$$\bar{Q}_A = -\frac{Q_A}{m_A^3 \chi_A^2}. \quad (4.35)$$

To match the 2.5PN order of the tidal terms, we include spin-orbit, spin-spin and rotationally induced quadrupolar moment effects [45, 47, 48, 51, 64, 71, 102, 105, 123, 157] within both the orbital energy,

$$\begin{aligned} E_{\text{BBH}}(v) = & -\frac{v\nu^2}{2} \left[1 + \left(-\frac{3}{4} - \frac{\nu}{12} \right) v^2 + \left(2\chi_A X_A \left(1 + \frac{X_A}{3} \right) - 2\chi_B X_B \left(1 + \frac{X_B}{3} \right) \right) v^3 \right. \\ & + \left(\frac{1}{8} \left(-27 + 19\nu - \frac{\nu^2}{3} \right) + 2\chi_A \chi_B \nu - (\bar{Q}_A + 1)\chi_A^2 X_A^2 - (\bar{Q}_B + 1)\chi_B^2 X_B^2 \right) v^4 \\ & \left. + \left(\chi_A X_A \left(3 + \frac{5X_A}{3} + \frac{29X_A^2}{9} + \frac{X_A^3}{9} \right) + \chi_B X_B \left(3 + \frac{5X_B}{3} + \frac{29X_B^2}{9} + \frac{X_B^3}{9} \right) \right) v^5 + \mathcal{O}(v^6) \right], \end{aligned} \quad (4.36)$$

and the flux,

$$\begin{aligned} F_{\text{BBH}}(v) = & \frac{32v^2\nu^{10}}{5} \left[1 + \left(-\frac{1247}{336} - \frac{35}{12}\nu \right) v^2 \right. \\ & + \left(4\pi + \chi_A X_A \left(-\frac{5}{4} - \frac{3X_A}{2} \right) + \chi_B X_B \left(-\frac{5}{4} - \frac{3X_B}{2} \right) \right) v^3 \\ & + \left(\left(-\frac{44711}{9072} + \frac{9271\nu}{504} + \frac{65\nu^2}{18} \right) + \frac{31}{8}\chi_A \chi_B \nu + \left(\frac{33}{16} + 2\bar{Q}_A \right) \chi_A^2 X_A^2 \right. \\ & + \left(\frac{33}{16} + 2\bar{Q}_B \right) \chi_B^2 X_B^2 \left. \right) v^4 + \left(\left(-\frac{8191}{672} - \frac{583\nu}{25} \right) \pi \right. \\ & + \chi_A X_A \left(-\frac{13}{16} + \frac{63X_A}{8} - \frac{73X_A^2}{36} - \frac{157X_A^3}{18} \right) \\ & \left. + \chi_B X_B \left(-\frac{13}{16} + \frac{63X_B}{8} - \frac{73X_B^2}{36} - \frac{157X_B^3}{18} \right) \right) v^5 + \mathcal{O}(v^6) \left. \right]. \end{aligned} \quad (4.37)$$

Therefore the full 2.5PN energy and flux expression are simply

$$E(v) = E_{\text{BBH}}(v) + E_{\bar{\lambda}_2}(v) + E_{\bar{\lambda}_3}(v), \quad (4.38)$$

$$F(v) = F_{\text{BBH}}(v) + F_{\bar{\lambda}_2}(v) + F_{\bar{\lambda}_3}(v). \quad (4.39)$$

At this point, we can repeat the expansion procedure from above to generate the series terms for the TaylorT4 and TaylorT2 approximants. Again, we treat terms like $\mathcal{O}(1) \sim \mathcal{O}(\bar{\lambda}_2 v^{10}) \sim \mathcal{O}(\bar{\lambda}_3 v^{14})$ as leading order and carry up through 2.5PN order.

Computing the TaylorT4 expansion according to Eq 4.7 where again we can break the series up into the terms corresponding to a BBH system ($\bar{\lambda}_2 = \bar{\lambda}_3 = 0, \bar{Q} = 1$) contained in $\mathcal{F}_{\text{BBH}}(v)$, and all of the expansion terms corresponding to the NS in $\mathcal{F}_{\text{Tid}}(v)$ where,

$$\mathcal{F}_{\text{Tid}}(v) = \frac{32\nu v^9}{5M} \left[\left(5(\bar{Q}_A - 1) \chi_A^2 X_A^2 \right) v^4 + \bar{\lambda}_{2A} X_A^4 v^{10} \left(\sum_{i=0}^5 \mathcal{F}_{2A,i} v^i \right) + \bar{\lambda}_{3A} X_A^6 v^{14} \left(\sum_{i=0}^5 \mathcal{F}_{3A,i} v^i \right) + (A \leftrightarrow B) \right]. \quad (4.40)$$

The coefficients $\mathcal{F}_{2A,i}$ and $\mathcal{F}_{3A,i}$ are given in the Appendix, Eq 4.67.

Again, the $\bar{\lambda}_2 \times \chi_{A,B}$ cross terms appearing in these coefficients are not due to spin-tidal interaction terms in the Hamiltonian, but instead are a consequence of the series expansion power counting. The $(\bar{Q}_A - 1)$ in the v^4 term arises from the fact that we have incorporated the BBH part of \bar{Q}_A into $\mathcal{F}_{\text{BBH}}(v)$ (for which $\bar{Q}_{\text{BH}} = 1$) and included the remainder here.

Similarly for TaylorT2, the updated time and phase expressions for Eq 4.14, 4.15 are

$$\mathcal{T}_{\text{Tid}}(v) = -\frac{5M}{256\nu v^8} \left[-\left(10(\bar{Q}_A - 1) \chi_A^2 X_A^2 \right) v^4 + \bar{\lambda}_{2A} X_A^4 v^{10} \left(\sum_{i=0}^5 \mathcal{T}_{2A,i} v^i \right) + \bar{\lambda}_{3A} X_A^6 v^{14} \left(\sum_{i=0}^5 \mathcal{T}_{3A,i} v^i \right) + (A \leftrightarrow B) \right], \quad (4.41)$$

$$\mathcal{P}_{\text{Tid}}(v) = -\frac{1}{32\nu v^5} \left[-\left(25(\bar{Q}_A - 1) \chi_A^2 X_A^2 \right) v^4 + \bar{\lambda}_{2A} X_A^4 v^{10} \left(\sum_{i=0}^5 \mathcal{P}_{2A,i} v^i \right) + \bar{\lambda}_{3A} X_A^6 v^{14} \left(\sum_{i=0}^5 \mathcal{P}_{3A,i} v^i \right) + (A \leftrightarrow B) \right]. \quad (4.42)$$

The individual coefficients $\mathcal{T}_{2A,i}, \mathcal{T}_{3A,i}, \mathcal{P}_{2A,i}, \mathcal{P}_{3A,i}$ are given in the Appendix, Eq 4.68, 4.69.

Spinning Dynamical Tides

With our extension into spinning systems, we need to take care to treat the dynamical tides more carefully. Since the dynamical tides is caused by the changing tidal field due to the orbital motion interacting with the internal f -modes of the deformable object, when the object is also spinning, then its internal modes will effectively experience a driving frequency equal to the orbital motion shifted by the object's spin. We characterize this by making a slight correction to the characteristic parameter $\gamma_{\ell A}$ in Eq 4.27.

Given an aligned spin of χ_A and a moment of inertia I_A , then we can compute the rotation frequency of the deformable object as

$$\bar{\omega}_A = M\omega_A = \frac{\chi_A}{X_A \bar{I}_A}, \quad (4.43)$$

where we have made I_A dimensionless by

$$\bar{I}_A = \frac{I_A}{m_A^3}. \quad (4.44)$$

Thus, the effective orbital frequency the resonant modes will experience is simply the difference between the orbital frequency and the rotational frequency of the object. With that in mind, we rewrite $\gamma_{\ell A}$ as

$$\gamma_{\ell A} = \left| \frac{\ell (v^3 - \bar{\omega}_A)}{\bar{\omega}_{f\ell A}} \right|. \quad (4.45)$$

We take the absolute value because Eq 4.27 is undefined for negative values of $\gamma_{\ell A}$, which can occur at low orbital frequencies with aligned spin objects. This corresponds to saying that the resonance modes of the object only care about the magnitude of the frequency of the changing tidal field. Within Eq 4.30, we also need to make change $\omega \rightarrow |v^3 - \bar{\omega}_A|/M$.

To show how this affects the profile of the dynamical tides correction, in Fig 4.1 we plot the profile of κ_ℓ from Eq 4.28 as a function of orbital frequency. We assume an NS with $\bar{\lambda}_2 \approx 800$ in an equal mass system and use the universal relations (see Table 4.2) to compute the other relevant tidal parameters. We compare the nonspinning NS against both aligned and antialigned spinning NS with magnitude $|\chi_{\text{NS}}| = .2$, which corresponds to a rotational frequency of $f_{\text{NS}} \approx 312\text{Hz}$. The upper frequency termination point is at an orbital frequency of $M\omega_{\text{ISCO}} = 6^{-3/2}$, which has been used as an estimate a BNS inspiral termination criterion [31].

From Fig 4.1 we can see that aligned spins pushed the resonance peak later in the inspiral while antialigned spins move the peak to earlier frequencies. In fact, with large enough aligned spins it is possible that the peak of the resonance is never reached before the system enters the merger/ringdown phase.

At low frequencies, the nonspinning system has the expected behavior of reducing to the simple static tides behavior ($\kappa_\ell = 1$). However, this is not true of the spinning systems, both of which asymptote to a slightly different value. Physically, these differences are due to the deformations of the object experiencing a driving frequency not from the orbital frequency (which is vanishingly small), but its own rotation along its axis. We expect this difference not to be a significant contribution to the waveform as the relative size of the tidal effects already vanishes ($\mathcal{O}(v^{10})$) at low frequencies anyways. The aligned spin object then passes through a point in the evolution where the orbital frequency matches exactly with its rotational frequency and the effective dynamical tidal field vanishes.

The possible issue is how the antialigned spin object dives through $\kappa_\ell = 0$ and plunges negative. We recognize there is a caveat with Eq 4.28, which is that this formula only valid up to frequencies shortly after the resonance peak [144]. While for nonspinning systems and spin aligned systems the resonance peak occurs near the end of the inspiral or after merger/ringdown and thus within the

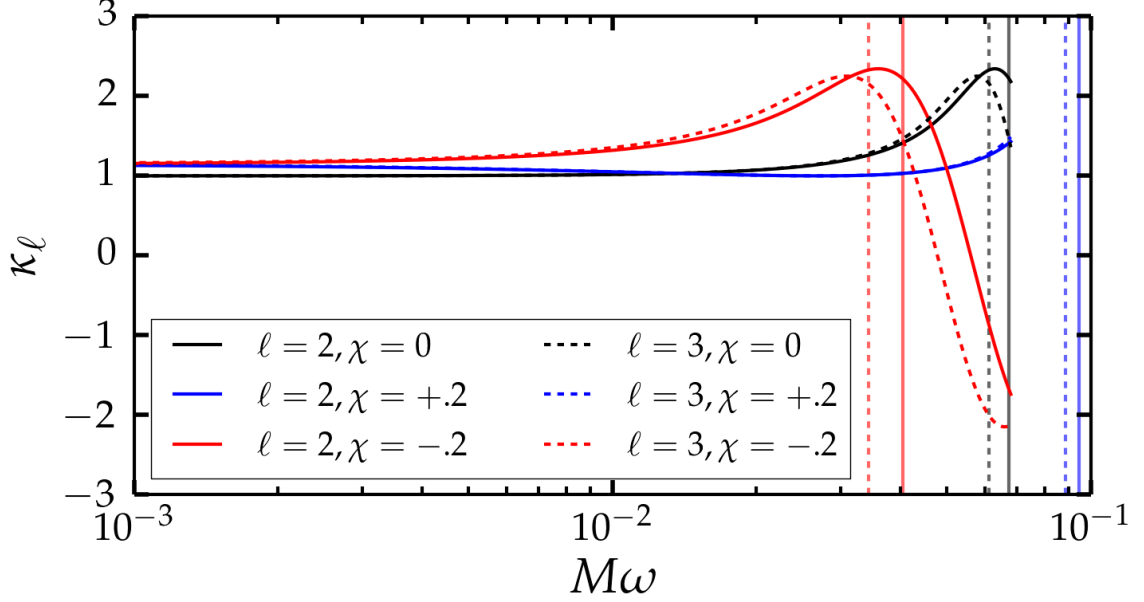


Figure 4.1: The dynamical tide amplification κ_ℓ as a function of orbital frequency, showing how the resonance profile from Eq 4.28 changes between the nonspinning case (black) and the spin aligned/antialigned (blue/red) cases for both $\ell = 2$ (solid) and $\ell = 3$ (dashed) tidal deformabilities. The vertical lines represent the resonance frequency for both modes in every case. The parameters correspond to an NS with $\bar{\lambda}_2 \approx 800$ in an equal mass system. For this NS, a spin magnitude of $|\chi_{\text{NS}}| = .2$ corresponds to a rotational frequency of $f_{\text{NS}} \approx 312\text{Hz}$.

range of validity, that condition does not necessarily apply in the antialigned case. If the antialigned spin is large enough, as seems to be the case in Fig 4.1, the resonance frequency occurs early enough in the evolution that this approximate formalism potentially breaks down while still in the inspiral, necessitating a more delicate handling of the dynamical tides.

Until such a formalism is developed for antialigned NS spins, we instead assume that the object is nonspinning (*i.e.* we set $\omega_A = 0$) for the purposes of Eq 4.28, 4.30; the aligned spin case will use Eq 4.45 as expected.

4.4 Tidal Splicing

Broadly speaking, the PN framework computes gravitational waveforms by solving the equations of motion,

$$\begin{aligned} \frac{d\phi}{dt} &= \frac{v^3}{M}, \\ \frac{dv}{dt} &= \mathcal{F}_{\text{BBH}}(v) + \mathcal{F}_{\text{Tid}}(v), \\ h^{\ell m}(t) &= \left(A_{\text{BBH}}^{\ell m}(v) + A_{\text{Tid}}^{\ell m}(v) \right) e^{i(\psi_{\text{BBH}}^{\ell m}(v) - m\phi)}, \end{aligned} \quad (4.46)$$

where we have expressed the equations within the TaylorT4 framework. Equivalently, they can be written within the TaylorT2 framework as

$$\begin{aligned}\phi(v) &= \phi_0 + \mathcal{P}_{\text{BBH}}(v) + \mathcal{P}_{\text{Tid}}(v), \\ t(v) &= t_0 + \mathcal{T}_{\text{BBH}}(v) + \mathcal{T}_{\text{Tid}}(v), \\ h^{\ell m}(t) &= \left(A_{\text{BBH}}^{\ell m}(v) + A_{\text{Tid}}^{\ell m}(v) \right) e^{i(\psi_{\text{BBH}}^{\ell m}(v) - m\phi)}. \end{aligned} \quad (4.47)$$

Considering the case of a BBH system: in principle if we knew the PN expansions for the expressions of \mathcal{F}_{BBH} (or \mathcal{P}_{BBH} and \mathcal{T}_{BBH}), $A_{\text{BBH}}^{\ell m}$ and $\psi_{\text{BBH}}^{\ell m}$ up through arbitrarily large order, then we could perfectly reproduce the gravitational waveforms of those inspiraling systems. The analytic complexity of computing these terms means we only know them up to a limited order.

Numerical simulations of BBH systems are able to accurately solve the full Einstein equations. Thus, if we can represent these numerical waveforms in a form akin to the systems of equations in either Eq 4.46 or Eq 4.47 (with vanishing tidal terms), they would be perfect representations of the PN expressions up to numerical resolution error. We can then substitute those numerically computed expression within the PN framework for their analytic BBH counterparts. Tidal Splicing is the prescription for decomposing numerical BBH waveforms to obtain PN-like expressions, then reconstructing the equations of motion while incorporating analytic tidal effects to generate waveforms corresponding to BHNS and BNS systems.

Waveform Decomposition

We start by taking a numerical BBH waveform corresponding to a system with a particular mass ratio q and spins aligned with the orbital angular momentum, χ_A and χ_B . Taking advantage of the PN decomposition of the (2,2) mode of a BBH waveform from Eq 4.21 evaluated as a function of time, t_{NR} , we write the (2,2) mode of the numerical waveform as

$$h_{\text{NR}}^{22}(t) = A_{\text{NR}}^{22}(t) e^{-2i\phi_{\text{NR}}(t)}. \quad (4.48)$$

This gives us the orbital phase $\phi_{\text{NR}}(t_{\text{NR}})$, from which we can compute the effective PN expansion parameter v_{NR} ,

$$v_{\text{NR}}(t) = \sqrt[3]{M \frac{d\phi_{\text{NR}}(t)}{dt}}. \quad (4.49)$$

(We use a 6th order finite difference scheme to compute the d/dt derivatives numerically.)

With the orbital phase and effective PN parameters in hand, we decompose each mode from the waveform into an amplitude and phase,

$$h_{\text{NR}}^{\ell m}(t) = A_{\text{NR}}^{\ell m}(t) e^{i\Phi_{\text{NR}}^{\ell m}(t)}. \quad (4.50)$$

Comparing with the expression for strain from Eq 4.22, we can break up the phase as,

$$\Phi_{\text{NR}}^{\ell m}(t) = \psi_{\text{NR}}^{\ell m}(t) - m\phi_{\text{NR}}(t). \quad (4.51)$$

Since we know ϕ_{NR} we can compute $\psi_{\text{NR}}^{\ell m}$ from the total phase by rearranging Eq 4.51,

$$\psi_{\text{NR}}^{\ell m}(t) = \Phi_{\text{NR}}^{\ell m}(t) + m\phi_{\text{NR}}(t). \quad (4.52)$$

Up to this point, we have been treating t_{NR} as the independent variable for the purposes of decomposition. Since the PN formalism considers the frequency expansion parameter ν as the independent variable, we shall now invert $\nu_{\text{NR}}(t)$ to get $t_{\text{NR}}(\nu)$ as a function of ν . From this, we can represent all of the individual parts of our waveform as functions of ν , e.g. $\phi_{\text{NR}}(t_{\text{NR}}(\nu)) = \phi_{\text{NR}}(\nu)$. Then we can write the strain for each mode in the familiar form like,

$$h_{\text{NR}}^{\ell m}(\nu) = A_{\text{NR}}^{\ell m}(\nu) e^{i(\psi_{\text{NR}}^{\ell m}(\nu) - m\phi_{\text{NR}}(\nu))}. \quad (4.53)$$

In this light, we now have numerical equivalents for the various PN expansions for BBH systems which are correct up to an arbitrary PN order limited only by the errors from the simulations themselves.

Evolution Splicing

With the numerical decomposition in hand, we will need the tidal parameters for the particular BHNS or BNS system under consideration. A review of the different tidal effects explored in the previous section show there are 6 different parameters which characterize the tidal behavior of each object: the dimensionless quadru-/octo-polar tidal deformabilities $\bar{\lambda}_2/\bar{\lambda}_3$, their corresponding f -mode resonance frequencies ω_{f2}/ω_{f3} , the dimensionless rotationally-induced quadrupole moment \bar{Q} , and the dimensionless moment of inertial \bar{I} . For our model, we make use of the universal relations, approximate relations between $\bar{\lambda}_2$ and the other tidal parameters; the details are given in Appendix 4.6. These choices would depend on the physical properties of the deformable object in consideration. Once we have chosen them, the next step in tidal splicing is the recomputation of the orbital evolution.

The details of how to specifically splice the PN tidal information into the orbital evolution depends on the specific Taylor expansion considered. We shall discuss the details of tidal splicing with TaylorT4 and TaylorT2. In general though, this method can also be performed for TaylorT3 [68] which involves expanding about an intermediate dimensionless time variable, however that expansion is known to do a poor job in general of reproducing the results of BBH numerical simulations even in the equal mass, nonspinning case [58, 59], so we ignore that method here. Performing TaylorT1 tidal splicing is currently intractable; due to the nature of the TaylorT1 expansion [68], we would need a method of adequately computing the BBH contribution to the PN energy and flux from just the waveform, introducing additional complications which we do not concern ourselves with here. While the [27] discussed tidal splicing under a TaylorF2 framework, in this paper only examine expansion of the the time domain approximants, though many of the concepts brought up here can be similarly expanded to the TaylorF2 formulation [67] as well.

TaylorT4 Splicing

Splicing with TaylorT4, originally introduced within [27], begins by examining how the tidal terms manifest in the TaylorT4 framework. The evolution of the PN parameter as seen in Eq 4.7 for a BBH system is

$$\frac{dv}{dt} = \mathcal{F}_{\text{BBH}}(v). \quad (4.54)$$

With $t_{\text{NR}}(v)$ in hand from the simulation, we can compute a numerically accurate version of $\mathcal{F}_{\text{BBH}}(v)$ which we shall call $\mathcal{F}_{\text{NR}}(v)$,

$$\mathcal{F}_{\text{NR}}(v) = \frac{1}{\frac{dt_{\text{NR}}(v)}{dv}}. \quad (4.55)$$

The tidal terms, $\mathcal{F}_{\text{Tid}}(v_{\text{NR}})$, represent the sum of the additional tidal effects in the evolution and we compute them according Eq 4.67. We incorporate the dynamical tides scaling the deformabilities according to Eq 4.28, *i.e.* $\bar{\lambda}_\ell \rightarrow \bar{\lambda}_\ell \kappa_\ell(v)$.

We express the tidal orbital evolution with a new spliced time coordinate, $t_{\text{Spl}}(v)$, which we compute by integrating the differential equation

$$\frac{dt_{\text{Spl}}}{dv} = \frac{1}{\mathcal{F}_{\text{NR}}(v) + \mathcal{F}_{\text{Tid}}(v)}. \quad (4.56)$$

We terminate the spliced waveforms at late times according to the simulations we test against, the details of which are given in Sec 4.5.

Once we have t_{Spl} , we find the orbital phase of this new waveform by

$$\phi_{\text{Spl}}(v) = \frac{1}{M} \int v(t_{\text{Spl}})^3 dt_{\text{Spl}}. \quad (4.57)$$

As the right hand side terms for this method are known at specific frequency nodes will not be uniformly spaced, we use Simpson's method for integration.

TaylorT2 Splicing

This approximate expands both the orbital phase and the time arrays as expansions of v , and for BBH systems looks like

$$\begin{aligned} t(v) &= t_0 + \mathcal{T}_{\text{BBH}}(v), \\ \phi(v) &= \phi_0 + \mathcal{P}_{\text{BBH}}(v). \end{aligned} \quad (4.58)$$

The constants t_0 and ϕ_0 correspond simply to the starting time and phase of the waveform.

Our numerically corrected versions of \mathcal{T}_{BBH} and \mathcal{P}_{BBH} are simply

$$\mathcal{T}_{\text{NR}}(v) = t_{\text{NR}}(v),$$

$$\mathcal{P}_{\text{NR}}(\nu) = \phi_{\text{NR}}(\nu). \quad (4.59)$$

Similar to TaylorT4, we compute the analytic TaylorT2 tidal effects, $\mathcal{T}_{\text{Tid}}(\nu)$ according to Eq 4.68 and $\mathcal{P}_{\text{Tid}}(\nu)$ according to Eq 4.69, incorporating the dynamical tides by making the frequency dependent adjustment to $\bar{\lambda}_\ell$ from Eq 4.28.

The spliced waveform's time t_{Spl} and phase ϕ_{Spl} are then given by examining Eq 4.13 and making the appropriate substitutions,

$$\begin{aligned} t_{\text{Spl}} &= t_0 + t_{\text{NR}}(\nu) + \mathcal{T}_{\text{Tid}}(\nu), \\ \phi_{\text{Spl}} &= \phi_0 + \phi_{\text{NR}}(\nu) + \mathcal{P}_{\text{Tid}}(\nu). \end{aligned} \quad (4.60)$$

We use the freedom inherent within choosing t_0 and ϕ_0 in order to align the spliced waveform at the initial time to the numerical waveform (though this is somewhat unnecessary as computing mismatches between waveforms marginalizes over these choices). We terminate the spliced waveforms at late times according to the simulations we test against, the details of which are given in Sec 4.5.

As the waveform nears the merger phase of the evolution, the effect from $\mathcal{T}_{\text{Tid}}(\nu)$ might grow larger than that of $t_{\text{NR}}(\nu)$. At that point the change in time values flatten out then decreases with increasing ν leading to unphysical behavior in the waveform, so we consider the PN approximation to have broken down and end the waveform there.

Waveform Reconstruction

Once $t_{\text{Spl}}(\nu)$ and $\phi_{\text{Spl}}(\nu)$ are computed, then the final step is reconstructing the spliced waveform. The expressions for $A_{\text{Tid}}^{\ell m}(\nu)$ in Eq 4.23 are the tidal corrections to the individual modes, with the dynamical tides accounted for by the replacement rule $\bar{\lambda}_2 \rightarrow \bar{\lambda}_{2A} \hat{\kappa}_{2A}(\nu)$ from Eq 4.30.

We then arrive at the final formula for the spliced waveform modes,

$$h_{\text{Spl}}^{\ell m}(t_{\text{Spl}}(\nu)) = \left(A_{\text{NR}}^{\ell m}(\nu) + A_{\text{Tid}}^{\ell m}(\nu) \right) e^{i(\psi_{\text{NR}}^{\ell m}(\nu) - m\phi_{\text{Spl}}(\nu))}. \quad (4.61)$$

From here, the amplitudes and phases of each mode are interpolated onto a uniform time grid using a cubic spline.

4.5 Results

Models for Comparison

To measure the efficacy of the tidal splicing method, we compare our spliced waveforms against numerical simulations of BHNS/BNS inspirals. In particular, we use some of the recent numerical simulations from [83]. In all simulations we compare against, the NSs were generated according to an EOS of $\Gamma = 2$ polytrope with a mass $M_{\text{ADM}} = 1.4M_\odot$ and compactness of $C_{\text{NS}} = 0.1444$ so that the quadrupolar tidal deformability is $\bar{\lambda}_2 \sim 800$. Comparing against 1 specific EOS at a single NS mass is a small slice of the full possible BHNS/BNS parameter space, but should give an idea for how well tidal splicing can perform. See Table 4.1 for the full list of the simulations we consider

Type	q	χ_{NS}	f_0 (Hz)	f_1 (Hz)	N_{cyc}^{22}
BHNS	1	0	218	578	19.9
BNS	1	0	211	629	20.8
BHNS	1	-0.2	217	505	17.0
BHNS	1.5	0	154	537	28.9
BHNS	2	0	156	505	21.0
BHNS	2	-0.2	156	485	19.8

Table 4.1: List of parameters for numerical simulations considered

here. In particular, there are 5 BHNS and 1 BNS runs, and two of the BHNS runs have a small anti-aligned spin on the NS while the rest of the runs are nonspinning.

We generated our tidally spliced waveforms for each of these cases using the hybridized surrogate model ‘NRHybSur3dq8’ [154] to compute the underlying BBH signal and making use of the universal relations to obtain the other tidal parameters from $\bar{\lambda}_2$; the details are given in Appendix 4.6.

To provide an additional point of comparison, we also test another waveform model, SEOBNRv4T, which is the time domain model SEOBNRv4 [53] augmented with most of the same effects we have used here, including higher order corrections to the static tides in the EOB potential Eq 4.63 [34], strain corrections Eq 4.23 [24], and dynamical tides (without the resonance frequency correction for spinning NSs) Eq 4.28, 4.30 [73]. The implementation of SEOBNRv4T we used here only outputs the (2,2) mode; however our analysis involves systems with mass ratios near unity so the (2,2) mode should dominate the gravitational waveforms. Thus, we anticipate this limitation should will be a minor effect on our results.

Waveforms

We include all modes from the numerical waveforms up through $\ell = 5$, while the surrogate and spliced waveforms use all available modes [(2, 0), (2, 1), (2, 2), (3, 2), (3, 0), (3, 1), (3, 3), (4, 2), (4, 3), (4, 4), (5, 5)], and SEOBNRv4T only has the (2,2) mode. (Since the system is spin-aligned, we only need $m \geq 0$ modes, symmetry gives $m < 0$ modes from that).

We choose the beginning of the waveform to be at a time after the initial burst of junk radiation, $t = 200M$. That time also set the starting orbital frequency of the waveform (chosen according half the the time derivative of the phase of the (2,2) mode). To prevent the starting frequency ω_{Initial} from being contaminated by residual junk radiation and slight eccentricities in the imperfect BHNS/BNS initial data, we use a quadratic fit of the simulations’ frequency against time over the first 500M to estimate the precise starting frequency. We window the waveform with a Planck-Taper window over that early 500M region of the waveform. We label the orbital frequency at the end of this window

as ω_0 ; this frequency will serve as the initial frequency considered in our mismatches below.

At late times, we set the upper frequency cutoff ω_{Cutoff} by the frequency attained by the simulation at its peak power, and window the waveform (again with Planck-Taper) over the times from $\omega_1 = .85\omega_{\text{Cutoff}}$ to ω_{Cutoff} . This gives us an inspiraling waveform from orbital frequency ω_0 to ω_1 , the values of which are given in Table 4.1 in physical units as f_0 and f_1 as measured in Hz. The other waveforms we generated from ω_{Initial} to ω_{Cutoff} and windowed in a similar manner. In Table 4.1, we also list the number of cycles in the (2,2) mode, N_{cyc}^{22} , in the numerical simulation within the listed orbital frequency bounds. While this is not necessarily a large frequency range to be making our comparisons, it is during the late inspiral where we expect the tidal effects to make the strongest contributions to the binary's evolution.

After we transform all of the waveforms into the frequency domain, we calculate the mismatches with the numerical waveforms. We follow the procedures used in Appendix D of [41] to evaluate overlap function assuming a 2-detector network, each measuring one of the polarizations with a flat noise spectrum, optimized over time and polarization phase shifts between the waveforms. The starting and ending frequency of the windowed waveforms, as given in Table 4.1, bound the frequency range for the mismatch computations. The mismatch between each of the models and the numerical simulation is then computed across a uniform distribution of sky locations.

As a quick aside, we attempted to compare against a pair of frequency domain tidal waveform models, SEOBNRv4ROM_NRTidal and IMRPhenomD_NRTidal, but found mismatches which we believed to be artificially large, near that of the BBH waveform. This is likely a consequence of having short numerical waveforms; because all of the time domain waveforms here are windowed in the same way, any systematic contamination introduced by the windows should be near identical across them all but that contamination will not affect the frequency domain waveforms. Thus, we have excluded the frequency domain waveforms from the results below.

Mismatch Comparison: All Modes

In Fig 4.2, we plot a histogram for the distribution of mismatches against the numerical waveform across sky locations in the case of the equal mass, nonspinning BHNS system. We do not normalize the vertical axis since the exact heights of the histograms are dependent on the binning choice; the location of the histogram peaks correspond to how well the model does while the spread measures how dependent the models is on sky location.

We estimate of the numerical simulation error during the inspiral by the mismatch between the simulation at two different resolutions (blue). Given that those mismatches are around $\sim 10^{-4}$, that suggests the simulations is well resolved during the inspiral. (Merger/ringdown might be a different story.) The mismatches with the surrogate BBH waveform (black) measures the strength of the tidal effects in the system, showing how poorly the waveforms will be if tidal effects are neglected entirely.

As expected, both of the tidal splicing methods we try here, TaylorT4 (magenta) and TaylorT2 (red),

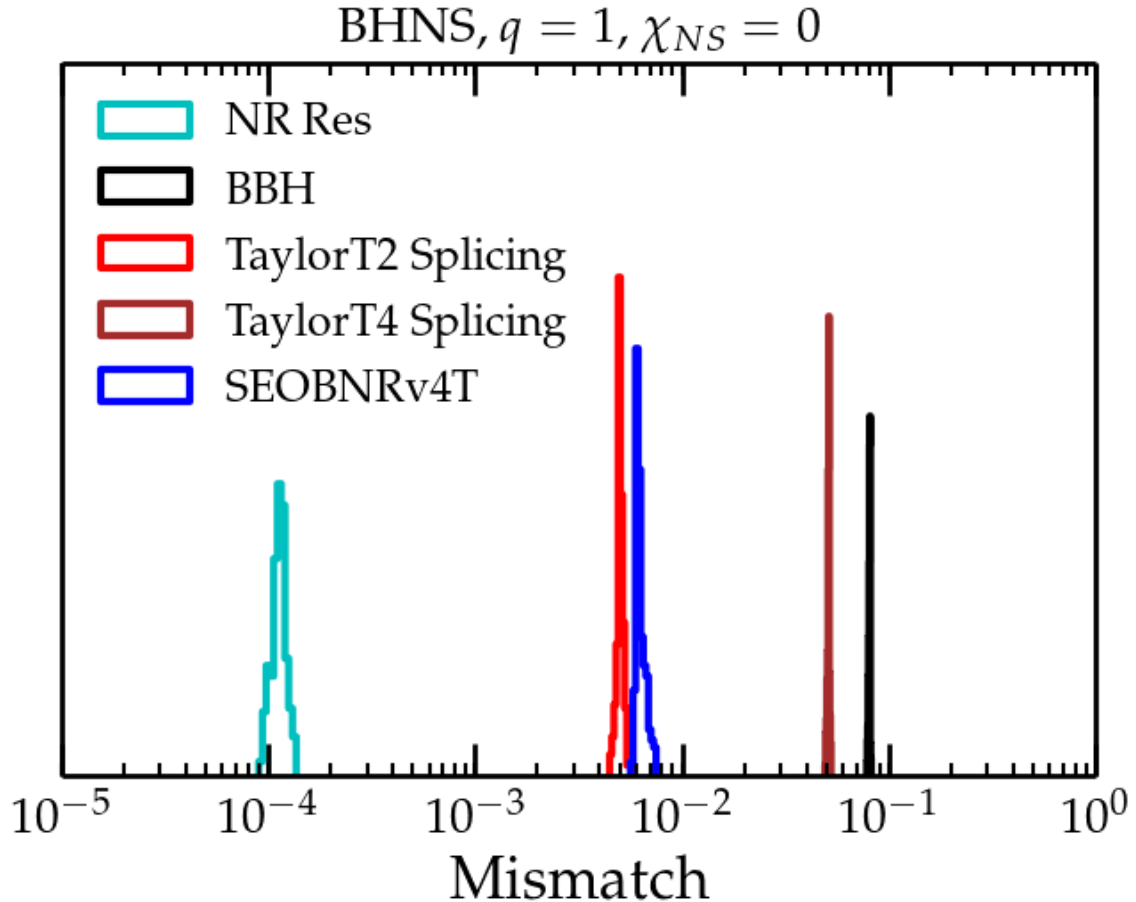


Figure 4.2: Distribution of mismatches against the inspiral of the BHNS, $q = 1$, nonspinning simulation across sky locations.

and the SEOBNRv4T model (cyan), all improve upon the BBH waveform, though to varying degrees. TaylorT4 splicing shows the least improvement, accounting for only some of the NSBH/BNS tidal effects, while both TaylorT2 and SEOBNRv4T have mismatches about an order of magnitude smaller. The narrowness of the peaks here likely correspond to the fact in equal mass, nonspinning systems the gravitational radiation is dominated almost entirely by the (2,2) mode regardless of which way the system is oriented.

In Fig 4.3, we observe similar patterns across most of the waveforms we considered. In all cases, the numerical error of the inspiral is well below any of the mismatches from the waveforms considered here, and the size of the tidal effects behaves qualitatively as expected (*i.e.* more extreme mass ratios have smaller tidal effects, spinning NS has larger tidal effects, ...). The hierarchy between the TaylorT2 splicing, SEOBNRv4T, and TaylorT4 splicing, is more or less preserved in all 6 cases as well; with the exception of the $q = 2$ cases, TaylorT4 is distinctly worse than SEOBNRv4T.

Comparing the $q = 1$ nonspinning BHNS and BNS cases (top- and middle-left) shows very lit-

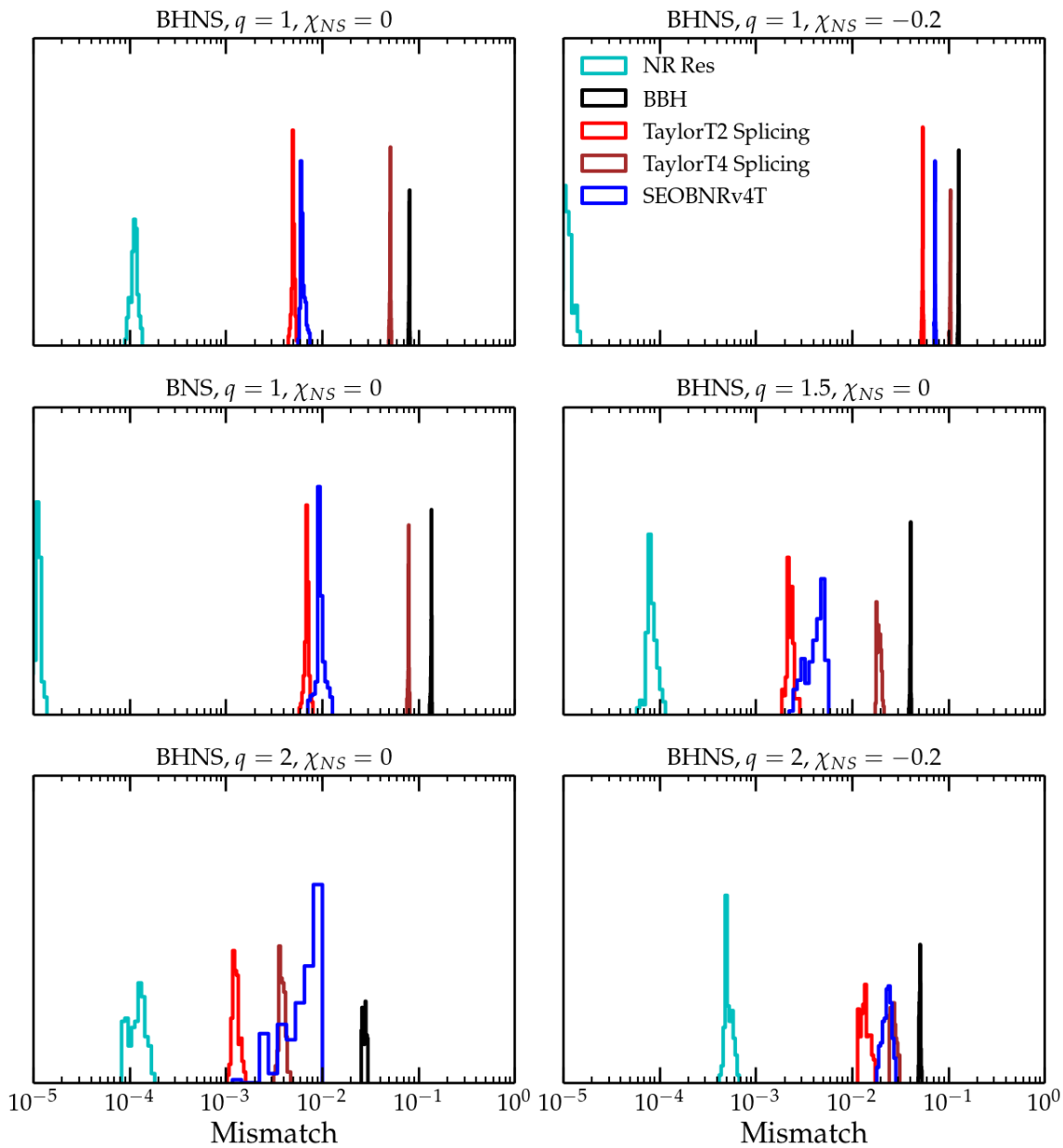


Figure 4.3: Similar to Fig 4.2, except displaying the mismatch histograms for all 6 numerical simulations we consider.

the change in behavior in the mismatches, with the BNS mismatches slightly larger, presumably because the tidal effects are at least twice as large (since two objects being deformed rather than 1). Increasing the BHNS mass ratio from $q = 1$ (top-left) to $q = 1.5$ (middle-right) and $q = 2$ (bottom-left), while keeping the system nonspinning shows improvement in the TaylorT4 splicing waveform in comparison to the others. The distribution for SEOBNRv4T widens significantly with the increasing mass ratio, likely owing at least in part to the growing significance of modes beyond $(2,2)$, as we will discuss below.

The most significant change to the mismatches arises in the case of the spinning NS ($q = 1$ top-right; $q = 2$ bottom-right). In both cases, the mismatches of the waveforms worsen significantly compared to the corresponding nonspinning cases. At best, the effects included here only account for some of the changes the spinning NS has on the evolution of the system and on the gravitational radiation. Either due to the missing spin-tidal terms (see Appendix 4.6), the inaccurate handling of the dynamical tides in the case of anti-aligned NS, or some other unaccounted tidal effect, further work will need to be done in order to properly capture the full behavior of these systems.

Mismatch Comparison: $(2,\pm 2)$ Modes

In order to characterize how much of the disparity between the TaylorT2 spliced and SEOBNRv4T waveforms is due to the inclusion of higher order modes in the former model, we compute the mismatches after restricting the BBH and spliced waveforms to only the $(2,\pm 2)$ modes (see Fig 4.4). The numerical simulations still utilize all the same modes as before.

In the nonspinning $q = 1$ BHNS and BNS systems, there is very little change in the mismatches in the spliced waveforms when excluding the other modes. This is almost certainly because a majority of the power in those waveforms is already concentrated in the $(2,2)$ mode so leaving out the other modes is a negligible change to the result. Thus the difference between the waveforms is within the differences in the models themselves. This also holds true for the spinning systems, as it seems that their handling of the spinning-tidal dynamics limits all of the models.

When moving to higher mass ratios for the nonspinning waveforms, the reverse is true namely TaylorT2 and TaylorT4 became worse with TaylorT2 comparable to SEOBNRv4T. The inclusion of higher order modes accounts entirely for the discrepancy between TaylorT2 spliced and SEOBNRv4T.

Discussion

A curious feature from these results is the rather disparate mismatch values between the TaylorT2 and TaylorT4 methods. That TaylorT4 splicing does so poorly is also odd considering how well TaylorT4 tend to do particularly well for simulating equal mass, nonspinning BBH waveforms. In principle, the only differences between these TaylorT2 spliced and TaylorT4 spliced waveforms should be the how the different PN approximantes handle the truncation error from missing higher order tidal terms. However, the dynamical tides correction do not have a proper power series expansion and thus the differences in the two splicing methods will not fall along neat PN lines; the

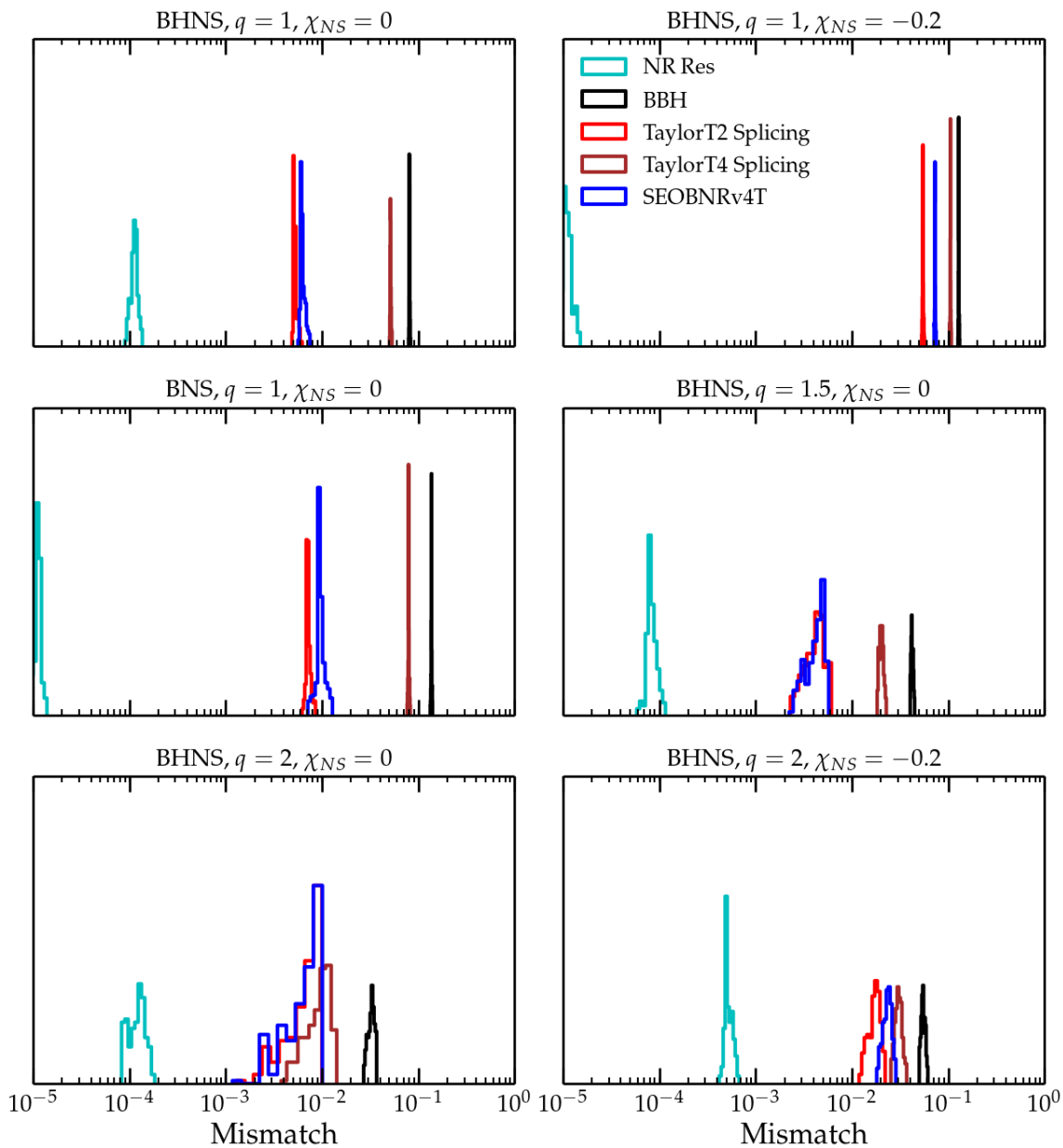


Figure 4.4: Similar to Fig 4.3, except that the BBH and tidally spliced waveforms are generated with only the (2,2) mode.

particular way which we incorporated the dynamical tides may yield different behaviors in the different splicing schemes. Another possibility is that the missing PN flux and strain coefficients which we set 0 might contribute to the difference, though given we expect them to be negligible contributions to the waveforms, so we deem it less likely those terms are the guilty culprit. More work will need to go into understanding if the differences between the methods is owing to the higher order truncations, the missing flux or strain coefficients, a consequence of how the dynamical tidal effects are handled, or some other factor.

Overall, the TaylorT2 splicing method show improvement (albeit very modest) over utilizing SEOB-NRv4T in all waveforms considered here while TaylorT4 needs further study before being used for BHNS/BNS systems.

4.6 Appendices

2.5PN Tidal Energy

Within the EOB framework, the Energy terms of the quadru- and octo-polar static deformation tidal terms are known to 2PN [34], which we can convert to an equivalent expression for the energy within the PN framework. For circular orbits, the full Hamiltonian is

$$H_{\text{EOB}}(u, J) = M \sqrt{1 + 2\nu \left(-1 + \sqrt{\mathcal{A}(u) \left(1 + \frac{J^2 u^2}{m_1^2 m_2^2} \right)} \right)}, \quad (4.62)$$

where $u = M/r$ is the dimensionless inverse EOB radial coordinate, J is the orbital angular momentum, and $\mathcal{A}(u)$ is the nonspinning radial PN potentials, known through 2PN.

This $\mathcal{A}(u)$ is given in [34], which we reproduce here for completeness,

$$\begin{aligned} \mathcal{A}(u) &= \mathcal{A}_{\text{BBH}}(u) + \mathcal{A}_{\bar{\lambda}_2}(u) + \mathcal{A}_{\bar{\lambda}_3}(u), \\ \mathcal{A}_{\text{BBH}}(u) &= 1 - 2u + 2\nu u^3 + \mathcal{O}(u^4), \\ \mathcal{A}_{\bar{\lambda}_2}(u) &= 3\bar{\lambda}_{2A} X_A^4 (1 - X_A) u^5 \left(u + u^2 \left(\frac{5}{2} X_A \right) + u^3 \left(\frac{337}{28} X_A^2 + \frac{1}{8} X_A + 3 \right) + \mathcal{O}(u^4) \right) + (A \rightarrow B), \\ \mathcal{A}_{\bar{\lambda}_3}(u) &= 3\bar{\lambda}_{3A} X_A^6 (1 - X_A) u^7 \left(u + u^2 \left(\frac{15}{2} X_A - 2 \right) + u^3 \left(\frac{110}{2} X_A^2 - \frac{311}{24} X_A + \frac{8}{3} \right) + \mathcal{O}(u^4) \right) \\ &\quad + (A \rightarrow B). \end{aligned} \quad (4.63)$$

Take note that there the first unknown terms in $\mathcal{A}(u)$ of order $\mathcal{O}(u^4)$ beyond leading order, which corresponds to the first unknown terms appearing at $\mathcal{O}(v^6)$ or 3PN order. Since the tidal effects only enter at full PN orders, these potentials are valid until to the first unknown terms at 3PN, *i.e.* up through 2.5PN.

To relate the EOB hamiltonian to the PN energy expansions, we relate the EOB radial variable u to the PN expansion variable, v , via the orbital phase ϕ_{orb} . Namely, ϕ_{orb} is both the conjugate variable of $p_\phi = J$, and one of the PN evolution equations as defined in Eq 4.1, therefore we establish the

relationship between the EOB and PN energy equations with

$$\frac{\partial \phi_{\text{orb}}}{\partial t} = \frac{\partial H_{\text{EOB}}(u, J)}{\partial J} = \frac{v^3}{M}. \quad (4.64)$$

Because we are considering circular orbits, the radial conjugate variable p_u is constant over the orbit, or $p_u = -\partial H_{\text{EOB}}(u, J)/\partial u = 0$, which reduces to

$$0 = \frac{\partial}{\partial u} \left(\mathcal{A}(u) \left(1 + \frac{J^2 u^2}{m_1^2 m_2^2} \right) \right), \quad (4.65)$$

providing a relation between J and u [34],

$$J^2 = - \frac{\frac{\partial \mathcal{A}(u)}{\partial u}}{\frac{\partial (u^2 \mathcal{A}(u))}{\partial u}}. \quad (4.66)$$

We can substitute this expression into Eq 4.64, reducing the expression to a formula connecting u and v , which we then expand to obtain u as a power series of v . We then insert that expansion into the EOB Hamiltonian Eq 4.62. By expressing the EOB Hamiltonian in powers of v , we obtain the PN Energy formula, complete up through the 2.5PN order which the $\mathcal{A}(u)$ potential is complete, which are given in Eq 4.32.

2.5PN Tidal Expressions

TaylorT4

Here are the full PN coefficients for the tidal terms in the TaylorT4 expansion in Eq 4.40,

$$\mathcal{F}_{\text{Tid}}(v) = \frac{32v\nu^9}{5M} \left[(5(\bar{Q}_A - 1)\chi_A^2 X_A^2) v^4 + \bar{\lambda}_{2A} X_A^4 v^{10} \left(\sum_{i=0}^5 \mathcal{F}_{2A,i} v^i \right) + \bar{\lambda}_{3A} X_A^6 v^{14} \left(\sum_{i=0}^5 \mathcal{F}_{3A,i} v^i \right) + (A \leftrightarrow B) \right],$$

$$\mathcal{F}_{2A,0} = 72 - 66X_A,$$

$$\mathcal{F}_{2A,2} = \frac{4421}{56} - \frac{12263X_A}{56} + \frac{1893X_A^2}{4} - \frac{661X_A^3}{2},$$

$$\mathcal{F}_{2A,3} = 216\pi - 216\pi X_A + \left(-\frac{1395X_A}{2} + \frac{753X_A^2}{2} + 281X_A^3 \right) \chi_A$$

$$+ \left(-\frac{1977}{2} + 2228X_A - \frac{3041X_A^2}{2} + 281X_A^3 \right) \chi_B,$$

$$\mathcal{F}_{2A,4} = \frac{2929}{96} + \alpha_4 - \frac{1115273X_A}{672} + \frac{180763X_A^2}{96} - \frac{592651X_A^3}{672} + \frac{25193X_A^4}{24} - \frac{8563X_A^5}{24}$$

$$+ \left(\frac{3915X_A^2}{8} - \frac{3771X_A^3}{8} + \bar{Q}_A (486X_A^2 - 468X_A^3) \right) \chi_A^2$$

$$+ \left(\frac{3861X_A}{4} - \frac{3789X_A^2}{2} + \frac{3717X_A^3}{4} \right) \chi_A \chi_B$$

$$+ \left(\frac{3915}{8} - \frac{11601X_A}{8} + \frac{11457X_A^2}{8} - \frac{3771X_A^3}{8} \right. \\ \left. + \bar{Q}_B (486 - 1440X_A + 1422X_A^2 - 468X_A^3) \right) \chi_B^2,$$

$$\mathcal{F}_{2A,5} = \frac{50601\pi}{112} - \frac{154957\pi X_A}{112} + \frac{5267\pi X_A^2}{2} - \frac{6807\pi X_A^3}{4} \\ + \left(-\frac{48145X_A}{14} + \frac{236779X_A^2}{84} - \frac{650371X_A^3}{168} + \frac{21111X_A^4}{8} + \frac{19277X_A^5}{12} \right) \chi_A \\ + \left(-\frac{570401}{84} + \frac{849409X_A}{42} - \frac{4606397X_A^2}{168} + \frac{319379X_A^3}{14} - \frac{250409X_A^4}{24} + \frac{19277X_A^5}{12} \right) \chi_B,$$

$$\mathcal{F}_{3A,0} = -104 + \beta_0 + 104X_A,$$

$$\mathcal{F}_{3A,2} = \frac{2971}{21} + \frac{3\beta_0}{2} + \beta_2 + \frac{1}{42}(-24898 + 7\beta_0)X_A + \frac{1}{6}(-659 - \beta_0)X_A^2 + \frac{3367X_A^3}{6},$$

$$\mathcal{F}_{3A,3} = -416\pi + 416\pi X_A + \left(-5(-234 + \beta_0)X_A + \frac{1}{3}(-2002 - 5\beta_0)X_A^2 - \frac{1508X_A^3}{3} \right) \chi_A \\ + \left(\frac{5018}{3} - \frac{20\beta_0}{3} + \left(-3848 + \frac{25\beta_0}{3} \right) X_A + \left(2678 - \frac{5\beta_0}{3} \right) X_A^2 - \frac{1508X_A^3}{3} \right) \chi_B,$$

$$\mathcal{F}_{3A,4} = -\frac{30892123}{18144} + \frac{99\beta_0}{8} + \frac{3\beta_2}{2} + \beta_4 + \left(\frac{16939927}{18144} - \frac{53\beta_0}{8} + \frac{\beta_2}{6} \right) X_A \\ + \left(\frac{481135}{672} + \frac{61\beta_0}{9} - \frac{\beta_2}{6} \right) X_A^2 \\ + \left(-\frac{659765}{224} - \frac{11\beta_0}{36} \right) X_A^3 + \left(1596 + \frac{11\beta_0}{72} \right) X_A^4 + \frac{11219X_A^5}{8} \\ + \left(\left(-\frac{1677}{2} + 3\beta_0 \right) X_A^2 + \frac{1677X_A^3}{2} + \bar{Q}_A \left((-832 + 3\beta_0)X_A^2 + 832X_A^3 \right) \right) \chi_A^2 \\ + \left((-1651 + 6\beta_0)X_A + (3302 - 6\beta_0)X_A^2 - 1651X_A^3 \right) \chi_A \chi_B \\ + \left[-\frac{1677}{2} + 3\beta_0 + \left(\frac{5031}{2} - 6\beta_0 \right) X_A + \left(-\frac{5031}{2} + 3\beta_0 \right) X_A^2 + \frac{1677X_A^3}{2} \right. \\ \left. + \bar{Q}_B \left(-832 + 3\beta_0 - 6(-416 + \beta_0)X_A + 3(-832 + \beta_0)X_A^2 + 832X_A^3 \right) \right] \chi_B^2,$$

$$\mathcal{F}_{3A,5} = \frac{24331\pi}{84} - \frac{65687\pi X_A}{84} - \frac{9196\pi X_A^2}{3} + \frac{10673\pi X_A^3}{3} \\ + \left[\left(\frac{456853}{168} - \frac{51\beta_0}{2} - 5\beta_2 \right) X_A + \left(\frac{1874947}{504} - \frac{25\beta_0}{2} - \frac{5\beta_2}{3} \right) X_A^2 + \left(\frac{256033}{56} \right. \right. \\ \left. \left. - \frac{61\beta_0}{6} \right) X_A^3 + \left(-\frac{563327}{72} + \frac{\beta_0}{6} \right) X_A^4 - \frac{114751X_A^5}{36} \right] \chi_A \\ + \left[\frac{3565057}{504} - 48\beta_0 - \frac{20\beta_2}{3} + \left(-\frac{1853417}{126} + \frac{241\beta_0}{3} + \frac{25\beta_2}{3} \right) X_A + \right. \\ \left. + \left(\frac{4784305}{252} - 42\beta_0 - \frac{5\beta_2}{3} \right) X_A^2 \right]$$

$$+ \left(-\frac{6381479}{252} + \frac{19\beta_0}{2} \right) X_A^3 + \left(\frac{1235639}{72} + \frac{\beta_0}{6} \right) X_A^4 - \frac{114751X_A^5}{36} \Big] \chi_B. \quad (4.67)$$

Note that $\mathcal{F}_{2A,0}$ and $\mathcal{F}_{2A,2}$ reproduce the TaylorT4 coefficients from the quadrupolar deformability which Ref [155] first computed.

TaylorT2

Here are the full PN coefficients for the tidal terms in the TaylorT2 expansion in Eq 4.42. For the correction to the time,

$$\begin{aligned} \mathcal{T}_{\text{Tid}}(v) = & -\frac{5M}{256\nu^8} \left[-\left(10(\bar{Q}_A - 1)\chi_A^2 X_A^2\right) v^4 + \bar{\lambda}_{2A} X_A^4 v^{10} \left(\sum_{i=0}^5 \mathcal{T}_{2A,i} v^i \right) \right. \\ & \left. + \bar{\lambda}_{3A} X_A^6 v^{14} \left(\sum_{i=0}^5 \mathcal{T}_{3A,i} v^i \right) + (A \leftrightarrow B) \right], \end{aligned}$$

$$\mathcal{T}_{2A,0} = 288 - 264X_A,$$

$$\mathcal{T}_{2A,2} = \frac{3179}{4} - \frac{919X_A}{4} - \frac{1143X_A^2}{2} + 65X_A^3,$$

$$\begin{aligned} \mathcal{T}_{2A,3} = & -576\pi + \frac{2496\pi X_A}{5} + \left(324X_A + 12X_A^2 - \frac{1096X_A^3}{5} \right) \chi_A \\ & + \left(588 - \frac{6616X_A}{5} + \frac{4772X_A^2}{5} - \frac{1096X_A^3}{5} \right) \chi_B, \end{aligned}$$

$$\begin{aligned} \mathcal{T}_{2A,4} = & \frac{32887109}{21168} + \frac{4\alpha_4}{3} - \frac{213838463X_A}{127008} + \frac{112207X_A^2}{252} - \frac{275777X_A^3}{504} - \frac{320X_A^4}{3} + \frac{1585X_A^5}{3} \\ & + \left(-\frac{639X_A^2}{2} + \frac{525X_A^3}{2} + \bar{Q}_A (-312X_A^2 + 256X_A^3) \right) \chi_A^2 \\ & + (-609X_A + 1108X_A^2 - 499X_A^3) \chi_A \chi_B \\ & + \left(-\frac{639}{2} + \frac{1803X_A}{2} - \frac{1689X_A^2}{2} + \frac{525X_A^3}{2} + \bar{Q}_B (-312 + 880X_A - 824X_A^2 + 256X_A^3) \right) \chi_B^2, \end{aligned}$$

$$\begin{aligned} \mathcal{T}_{2A,5} = & -\frac{241295\pi}{98} + \frac{216921\pi X_A}{98} - \frac{7528\pi X_A^2}{7} + \frac{7142\pi X_A^3}{7} \\ & + \left(\frac{101949X_A}{49} + \frac{48875X_A^2}{294} - \frac{78373X_A^3}{147} - \frac{3417X_A^4}{7} - \frac{2574X_A^5}{7} \right) \chi_A \\ & + \left(\frac{637447}{147} - \frac{1026647X_A}{98} + \frac{931999X_A^2}{98} - \frac{713938X_A^3}{147} + \frac{12977X_A^4}{7} - \frac{2574X_A^5}{7} \right) \chi_B, \end{aligned}$$

$$\mathcal{T}_{3A,0} = \frac{4}{3}(-104 + \beta_0) + \frac{416X_A}{3},$$

$$\mathcal{T}_{3A,2} = -\frac{6688}{21} + \frac{995\beta_0}{168} + \beta_2 + \left(-\frac{4934}{7} + \frac{17\beta_0}{3} \right) X_A + \frac{17}{6}(365 - 2\beta_0)X_A^2 - \frac{65X_A^3}{6},$$

$$\mathcal{T}_{3A,3} = -\frac{64}{9}(-52 + \beta_0)\pi - \frac{3328\pi X_A}{9}$$

$$\begin{aligned}
& + \left(\frac{20}{9}(-52 + 3\beta_0)X_A + \frac{16}{27}(-39 + 7\beta_0)X_A^2 + \frac{416X_A^3}{3} \right) \chi_A \\
& + \left(\frac{4}{27}(-1716 + 73\beta_0) + \left(\frac{5824}{9} - \frac{404\beta_0}{27} \right) X_A + \frac{16}{27}(-897 + 7\beta_0)X_A^2 + \frac{416X_A^3}{3} \right) \chi_B, \\
\mathcal{T}_{3A,4} = & - \frac{35111473}{19845} + \frac{6080015\beta_0}{254016} + \frac{199\beta_2}{42} + \frac{4\beta_4}{5} + \left(-\frac{68598877}{39690} + \frac{16999\beta_0}{840} + \frac{68\beta_2}{15} \right) X_A \\
& + \frac{(-1443037 - 16319\beta_0 - 11424\beta_2)X_A^2}{2520} + \left(\frac{154907}{40} - \frac{2477\beta_0}{90} \right) X_A^3 \\
& + \left(\frac{608}{3} + \frac{2477\beta_0}{180} \right) X_A^4 - \frac{91X_A^5}{18} \\
& + \left(\left(\frac{858}{5} - \frac{57\beta_0}{10} \right) X_A^2 - \frac{858X_A^3}{5} + \bar{Q}_A \left(\frac{4}{5}(208 - 7\beta_0)X_A^2 - \frac{832X_A^3}{5} \right) \right) \chi_A^2 \\
& + \left(\left(\frac{1612}{5} - 11\beta_0 \right) X_A + \left(-\frac{3224}{5} + 11\beta_0 \right) X_A^2 + \frac{1612X_A^3}{5} \right) \chi_A \chi_B \\
& + \left[\frac{858}{5} - \frac{57\beta_0}{10} + \frac{3}{5}(-858 + 19\beta_0)X_A + \left(\frac{2574}{5} - \frac{57\beta_0}{10} \right) X_A^2 - \frac{858X_A^3}{5} \right. \\
& \quad \left. + \bar{Q}_B \left(\frac{4}{5}(208 - 7\beta_0) + \frac{8}{5}(-312 + 7\beta_0)X_A - \frac{4}{5}(-624 + 7\beta_0)X_A^2 - \frac{832X_A^3}{5} \right) \right] \chi_B^2, \\
\mathcal{T}_{3A,5} = & - \frac{1}{462}(-520852 + 17705\beta_0 + 2688\beta_2)\pi \\
& + \left(\frac{68890}{77} - \frac{482\beta_0}{33} \right) \pi X_A + \frac{2}{33}(-18128 + 241\beta_0)\pi X_A^2 - \frac{30472\pi X_A^3}{33} \\
& + \left[\frac{1}{924}(-648524 + 49273\beta_0 + 5040\beta_2)X_A + \frac{(-938394 + 82637\beta_0 + 4704\beta_2)X_A^2}{1386} \right. \\
& + \frac{1}{693}(44267 + 91\beta_0)X_A^3 + \frac{1}{99}(98807 - 1270\beta_0)X_A^4 + \left. \frac{31382X_A^5}{99} \right] \chi_A \\
& + \left[\frac{-4678620 + 277897\beta_0 + 24528\beta_2}{2772} + \frac{(8817872 - 337219\beta_0 - 33936\beta_2)X_A}{2772} \right. \\
& \quad \left. + \frac{(-1878832 - 23497\beta_0 + 4704\beta_2)X_A^2}{1386} + \left(\frac{54574}{231} + \frac{563\beta_0}{11} \right) X_A^3 \right. \\
& \quad \left. + \frac{1}{99}(-68399 - 1270\beta_0)X_A^4 + \frac{31382X_A^5}{99} \right] \chi_B, \tag{4.68}
\end{aligned}$$

and for the phase,

$$\begin{aligned}
\mathcal{P}_{\text{Tid}}(v) = & - \frac{1}{32v^5} \left[- (25(\bar{Q}_A - 1)\chi_A^2 X_A^2) v^4 + \bar{\lambda}_{2A} X_A^4 v^{10} \left(\sum_{i=0}^5 \mathcal{P}_{2A,i} v^i \right) \right. \\
& \left. + \bar{\lambda}_{3A} X_A^6 v^{14} \left(\sum_{i=0}^5 \mathcal{P}_{3A,i} v^i \right) + (A \leftrightarrow B) \right],
\end{aligned}$$

$$\mathcal{P}_{2A,0} = 72 - 66X_A,$$

$$\begin{aligned}
\mathcal{P}_{2A,2} &= \frac{15895}{56} - \frac{4595X_A}{56} - \frac{5715X_A^2}{28} + \frac{325X_A^3}{14}, \\
\mathcal{P}_{2A,3} &= -225\pi + 195\pi X_A + \left(\frac{2025X_A}{16} + \frac{75X_A^2}{16} - \frac{685X_A^3}{8} \right) \chi_A \\
&\quad + \left(\frac{3675}{16} - \frac{4135X_A}{8} + \frac{5965X_A^2}{16} - \frac{685X_A^3}{8} \right) \chi_B, \\
\mathcal{P}_{2A,4} &= \frac{164435545}{254016} + \frac{5\alpha_4}{9} - \frac{1069192315X_A}{1524096} + \frac{561035X_A^2}{3024} - \frac{1378885X_A^3}{6048} - \frac{400X_A^4}{9} + \frac{7925X_A^5}{36} \\
&\quad + \left(-\frac{1065X_A^2}{8} + \frac{875X_A^3}{8} + \bar{Q}_A \left(-130X_A^2 + \frac{320X_A^3}{3} \right) \right) \chi_A^2 \\
&\quad + \left(-\frac{1015X_A}{4} + \frac{1385X_A^2}{3} - \frac{2495X_A^3}{12} \right) \chi_A \chi_B \\
&\quad + \left(-\frac{1065}{8} + \frac{3005X_A}{8} - \frac{2815X_A^2}{8} + \frac{875X_A^3}{8} \right. \\
&\quad \left. + \bar{Q}_B \left(-130 + \frac{1100X_A}{3} - \frac{1030X_A^2}{3} + \frac{320X_A^3}{3} \right) \right) \chi_B^2, \\
\mathcal{P}_{2A,5} &= -\frac{241295\pi}{224} + \frac{216921\pi X_A}{224} - \frac{941\pi X_A^2}{2} + \frac{3571\pi X_A^3}{8} \\
&\quad + \left(\frac{101949X_A}{112} + \frac{48875X_A^2}{672} - \frac{78373X_A^3}{336} - \frac{3417X_A^4}{16} - \frac{1287X_A^5}{8} \right) \chi_A \\
&\quad + \left(\frac{637447}{336} - \frac{1026647X_A}{224} + \frac{931999X_A^2}{224} - \frac{356969X_A^3}{168} + \frac{12977X_A^4}{16} - \frac{1287X_A^5}{8} \right) \chi_B, \\
\mathcal{P}_{3A,0} &= \frac{5}{9}(-104 + \beta_0) + \frac{520X_A}{9}, \\
\mathcal{P}_{3A,2} &= \frac{5(-53504 + 995\beta_0 + 168\beta_2)}{1848} + \left(-\frac{24670}{77} + \frac{85\beta_0}{33} \right) X_A - \frac{85}{66}(-365 + 2\beta_0)X_A^2 - \frac{325X_A^3}{66}, \\
\mathcal{P}_{3A,3} &= -\frac{10}{3}(-52 + \beta_0)\pi - \frac{520\pi X_A}{3} + \left(\frac{25}{24}(-52 + 3\beta_0)X_A + \frac{5}{18}(-39 + 7\beta_0)X_A^2 + 65X_A^3 \right) \chi_A \\
&\quad + \left(\frac{5}{72}(-1716 + 73\beta_0) + \left(\frac{910}{3} - \frac{505\beta_0}{72} \right) X_A + \frac{5}{18}(-897 + 7\beta_0)X_A^2 + 65X_A^3 \right) \chi_B, \\
\mathcal{P}_{3A,4} &= \frac{5(-2247134272 + 30400075\beta_0 + 6017760\beta_2)}{13208832} + \frac{5\beta_4}{13} \\
&\quad + \left(-\frac{342994385}{412776} + \frac{84995\beta_0}{8736} + \frac{85\beta_2}{39} \right) X_A - \frac{5(1443037 + 16319\beta_0 + 11424\beta_2)X_A^2}{26208} \\
&\quad + \frac{5(1394163 - 9908\beta_0)X_A^3}{3744} + \frac{5(36480 + 2477\beta_0)X_A^4}{1872} - \frac{175X_A^5}{72} \\
&\quad + \left(\left(\frac{165}{2} - \frac{285\beta_0}{104} \right) X_A^2 - \frac{165X_A^3}{2} + \bar{Q}_A \left(\left(80 - \frac{35\beta_0}{13} \right) X_A^2 - 80X_A^3 \right) \right) \chi_A^2 \\
&\quad + \left(\left(155 - \frac{275\beta_0}{52} \right) X_A + \left(-310 + \frac{275\beta_0}{52} \right) X_A^2 + 155X_A^3 \right) \chi_A \chi_B
\end{aligned}$$

$$\begin{aligned}
& + \left[\frac{165}{2} - \frac{285\beta_0}{104} + \frac{15}{52}(-858 + 19\beta_0)X_A + \left(\frac{495}{2} - \frac{285\beta_0}{104} \right) X_A^2 - \frac{165X_A^3}{2} \right. \\
& \quad \left. + \bar{Q}_B \left(80 - \frac{35\beta_0}{13} + \left(-240 + \frac{70\beta_0}{13} \right) X_A + \left(240 - \frac{35\beta_0}{13} \right) X_A^2 - 80X_A^3 \right) \right] \chi_B^2, \\
\mathcal{P}_{3A,5} = & - \frac{5(-520852 + 17705\beta_0 + 2688\beta_2)\pi}{4704} + \frac{5(103335 - 1687\beta_0)\pi X_A}{1176} \\
& + \frac{5}{168}(-18128 + 241\beta_0)\pi X_A^2 - \frac{19045\pi X_A^3}{42} \\
& + \left[\frac{5(-648524 + 49273\beta_0 + 5040\beta_2)X_A}{9408} + \frac{5(-938394 + 82637\beta_0 + 4704\beta_2)X_A^2}{14112} \right. \\
& \quad \left. + \frac{5(44267 + 91\beta_0)X_A^3}{7056} - \frac{5(-98807 + 1270\beta_0)X_A^4}{1008} + \frac{78455X_A^5}{504} \right] \chi_A \\
& + \left[\frac{5(-4678620 + 277897\beta_0 + 24528\beta_2)}{28224} - \frac{5(-8817872 + 337219\beta_0 + 33936\beta_2)X_A}{28224} \right. \\
& \quad \left. + \left(-\frac{5(1878832 + 23497\beta_0)}{14112} + \frac{5\beta_2}{3} \right) X_A^2 + \frac{5(54574 + 11823\beta_0)X_A^3}{2352} \right. \\
& \quad \left. - \frac{5(68399 + 1270\beta_0)X_A^4}{1008} + \frac{78455X_A^5}{504} \right] \chi_B. \tag{4.69}
\end{aligned}$$

Model Parameters

To serve as our underlying proxy for numerical data instead, we use the hybridized surrogate model ‘NRHybSur3dq8’ [154]. This model accurately captures the behavior of nonprecessing BBH systems for mass ratios up to $q = 8$ with component spins $\chi \leq .8$ and including all of the following modes: [(2, 0), (2, 1), (2, 2), (3, 2), (3, 0), (3, 1), (3, 3), (4, 2), (4, 3), (4, 4), (5, 5)]. This parameter space spans across the corresponding space of BNS and BHNS systems where the expected breakup spin for a neutron star ($\chi \sim .7$), and the size tidal effects rapidly diminishes for mass ratios significantly larger than on (the leading order tidal term in the Taylor expansions goes as X_A^4).

The tidal effects of each object are then dependent on the object’s mass and the choice of EOS. There are currently six tidal parameters which enter into our model: the quadru-/octo-pole static tidal deformabilities, $\bar{\lambda}_2/\bar{\lambda}_3$, their corresponding f -mode resonant frequencies, $\bar{\omega}_{f2}/\bar{\omega}_{f3}$, the dimensionless rotationally-induced quadrupole moment \bar{Q} , and the dimensionless moment of inertia \bar{I} . (In Appendix 4.6, we also briefly discuss how to include the 4 spin-tidal deformability parameters though they currently are not a part of our model)

While in general, all of these parameters depend on the specific details of the object’s mass and EOS, recent analysis of these numbers show that the various parameters follow a series of universal relations which can accurately approximate their values given just $\bar{\lambda}_2$. The universal relations we use here all follow the same form [161, 162],

$$y = \sum_{i=0}^4 a_i (\ln x)^i, \tag{4.70}$$

x	y	a_0	a_1	a_2	a_3	a_4	Ref
$\bar{\lambda}_2$	$\ln \bar{Q}$	0.194	0.0936	0.0474	-4.21×10^{-3}	1.23×10^{-4}	[161, 162]
$\bar{\lambda}_2$	$\ln \bar{I}$	1.47	0.0817	0.0149	2.87×10^{-4}	-3.64×10^{-5}	[161, 162]
$\bar{\lambda}_2$	$\ln \bar{\lambda}_3$	-1.15	1.18	-0.0251	-1.31×10^{-3}	2.52×10^{-5}	[158]
$\bar{\lambda}_2$	$X_A \bar{\omega}_{f2}$	0.1820	-6.836×10^{-3}	-4.196×10^{-3}	5.215×10^{-4}	-1.857×10^{-5}	[62]
$\bar{\lambda}_3$	$X_A \bar{\omega}_{f3}$	0.2245	-0.01500	-1.412×10^{-3}	1.832×10^{-4}	-5.561×10^{-6}	[62]

Table 4.2: Universal Relations relating the static dimensionless deformability to various other dimensionless tidal parameters using Eq 4.70

where a_i are the numerically fitted coefficients relating the two tidal parameters, x and y , to each other on Table 4.2. Thus, the properties of the NS of different theoretical EOS could be represented by how that EOS traces out the curve of allowable $\bar{\lambda}_2$ as a function of the mass of the NS. The extra factor of X_A which appears as part of the dimensionless resonance frequencies $\bar{\omega}_{f\ell}$ in Table 4.2 arises because [62] defines their dimensionless resonance frequency as $m_A \omega_{f\ell}$ whereas we use $\bar{\omega}_{f\ell} = M \omega_{f\ell}$.

Utilizing these universal relations reduces the effective parameter space of the tidal information from 12 (6 for each object) to just the static quadrupolar tidal deformability for each object, since they are all derived simply from the choice of $\bar{\lambda}_2$. All together our spliced waveforms effectively fill a 6D parameter space: $(q, M, \chi_A, \chi_B, \bar{\lambda}_{2A}, \bar{\lambda}_{2B})$.

For all of the various, unknown higher order coefficients (α_4 from the quadrupolar tidal flux Eq 4.34, $\beta_0, \beta_2, \beta_4$ from the octopolar tidal flux Eq 4.34, and $\alpha_4^{22}, \alpha_2^{21}, \alpha_2^{33}, \alpha_2^{31}$ from the tidal strain amplitude corrections Eq 4.23), we set them to 0 uniformly. Further study is needed in order to characterize the error associated with such a choice. In the case of the strain amplification corrections, the we expect missing coefficients to be subdominant contributions to the signal according to Ref [65].

Spin-Tidal Connection Terms

In the expressions above, there are a number of terms which scale as $\bar{\lambda}_{2A} \chi_A$, so one might be tempted to view them as connection between the object's tidal deformation and spin. Tracing back to the original energy and flux expressions, we know that instead these terms arise naturally as a consequence of power counting in the series expansion, and are merely cross terms between the tidal and SO or SS effects.

Two different groups, Ref [153] and [110], derived the first spin-tidal connection terms in the PN expansion. However, their two results are not consistent with each other, so we do not include either within our current splicing model. We do look at each paper and summarize how to implement either these effects within our framework so that when this discrepancy is resolved, tidal splicing can be updated.

The leading order spin-tidal terms all enter at the ν^{13} order and there are 4 related effects which

all enter at this order, each with its own dimensionless tidal deformability coefficient: $\bar{\lambda}_{23}$ the mass quadrupole tidal deformation arising due to the gravitomagnetic octopole tidal field; $\bar{\lambda}_{32}$ the mass octopole tidal deformation arising due to the gravitomagnetic quadrupole tidal field; $\bar{\sigma}_{23}$ the current quadrupole tidal deformation arising due to the gravitoelectric octopole tidal field; $\bar{\sigma}_{32}$ the current octopole tidal deformation arising due to the gravitoelectric quadrupole tidal field.

To obtain the TaylorT terms, examine leading order terms in the PN energy and flux, so then

$$\begin{aligned} E_{\text{ST}} &= -\frac{\nu v^2}{2} \left(1 + v^{13} \chi_A X_A^6 \sum_i \epsilon_{iA} \bar{\Lambda}_{iA} + (A \rightarrow B) \right), \\ F_{\text{ST}} &= \frac{32\nu^2 v^{10}}{5} \left(1 + v^{13} \chi_A X_A^6 \sum_i \rho_{iA} \bar{\Lambda}_{iA} + (A \rightarrow B) \right), \end{aligned} \quad (4.71)$$

where the sums are over each of the ST parameters $\bar{\Lambda}_{iA} = (\bar{\lambda}_{23A}, \bar{\lambda}_{32A}, \bar{\sigma}_{23A}, \bar{\sigma}_{32A})$, with energy coefficients ϵ_{iA} and flux coefficients ρ_{iA} which are functions only on the mass fraction of the object X_A . In principle, we would need to include these energy and flux corrections into the full energy (Eq 4.32 and flux (Eq 4.34 equations. In practice, any cross terms which enter the full TaylorT expansions will show up earliest as $\bar{\lambda}_2 \times \bar{\lambda}_2$ cross terms to order v^{20} , coupled with tossing any higher orders terms which drop out, means we only need to consider the above expressions to obtain the results we desire.

We can expand this now in both the TaylorT4 and TaylorT2 manner yielding

$$\begin{aligned} \mathcal{F}_{\text{ST}}(v) &= \frac{32\nu v^9}{5M} \left[v^{13} \chi_A X_A^6 \sum_i \left(-\frac{15}{2} \epsilon_{iA} + \rho_{iA} \right) \bar{\Lambda}_{iA} \right], \\ \mathcal{T}_{\text{ST}}(v) &= -\frac{5M}{256\nu v^8} \left[v^{13} \chi_A X_A^6 \sum_i \left(-12\epsilon_{iA} + \frac{8}{5} \rho_{iA} \right) \bar{\Lambda}_{iA} \right], \\ \mathcal{P}_{\text{ST}}(v) &= -\frac{1}{32\nu v^5} \left[v^{13} \chi_A X_A^6 \sum_i \left(-\frac{75}{16} \epsilon_{iA} + \frac{5}{8} \rho_{iA} \right) \bar{\Lambda}_{iA} \right]. \end{aligned} \quad (4.72)$$

We can linearly add to the full tidal PN expressions $\mathcal{F}_{\text{Tid}}(v)$, $\mathcal{T}_{\text{Tid}}(v)$, and $\mathcal{P}_{\text{Tid}}(v)$, respectively.

To showcase the effects which these spin-tidal terms can have on the results of our spliced surrogate, we tested how our mismatch results changed for the spinning BNS systems using the results from both papers [110, 153]. In no particular order, we first examine [110], beginning with the correspondence between their (dimensionful) definitions of the deformability parameters,

$$\begin{aligned} \bar{\lambda}_{23} &= m_A^{-6} \hat{\lambda}_2, \\ \bar{\lambda}_{32} &= m_A^{-6} \hat{\lambda}_3, \\ \bar{\sigma}_{23} &= -m_A^{-6} \hat{\sigma}_2, \\ \bar{\sigma}_{32} &= -m_A^{-6} \hat{\sigma}_3. \end{aligned} \quad (4.73)$$

From this we can write their energy and flux coeffs by reading off from Eq (28),(30) of [110],

$$\begin{aligned}\epsilon_{iA} &= \frac{44(1 - X_A)}{7X_A} (18, -2, -4, 3), \\ \rho_{iA} &= \left(144 - \frac{204}{X_A}, -16 + \frac{16}{X_A}, -38 + \frac{113}{3X_A}, 24 - \frac{24}{X_A} \right).\end{aligned}\quad (4.74)$$

Repeating this same setup but with [153], we find the correspondence between their definitions and ours as

$$\begin{aligned}\bar{\lambda}_{23} &= \frac{M^2}{m_A^6} \lambda_{23}, \\ \bar{\lambda}_{32} &= \frac{M^2}{m_A^6} \lambda_{32}, \\ \bar{\sigma}_{23} &= \frac{M^2}{m_A^6} \sigma_{23}, \\ \bar{\sigma}_{32} &= \frac{M^2}{m_A^6} \sigma_{32},\end{aligned}\quad (4.75)$$

and using their Eq (90),(95),

$$\begin{aligned}\epsilon_{iA} &= \frac{1 - X_A}{X_A} (96, -32, -32, 24), \\ \rho_{iA} &= \left(96 - \frac{136}{X_A}, -32 + \frac{32}{X_A}, -38 + \frac{113}{3X_A}, 24 - \frac{24}{X_A} \right).\end{aligned}\quad (4.76)$$

$\bar{\lambda}_2 \times \bar{\lambda}_2$ Self-Cross Terms

An odd quirk of how the PN formulation of the quadrupolar static tidal results, means that the leading order tidal terms are treated as effectively being the same formal order as the leading Newtonian order for the BBH for the purposes of power series expansions. Or in otherwords, PN views $\mathcal{O}(\bar{\lambda}_2 v^{10}) \sim \mathcal{O}(1)$. Extending this logic, we see that this analytic equivalence holds for $\mathcal{O}(\bar{\lambda}_2^2 v^{20}), \mathcal{O}(\bar{\lambda}_2^3 v^{30})$ and all higher terms of the form $\mathcal{O}(\bar{\lambda}_2^n v^{10n})$. To be clear, these are not nonlinear static tidal terms despite their appearance as such. Similar to how the terms which go as $\bar{\lambda}_2 \times \chi_{A,B}$ in Eq 4.67, 4.68, and 4.69 are power series cross terms between spin-orbit and tidal terms and not spin-tidal coefficients, these $\bar{\lambda}_2 \times \bar{\lambda}_2$ are not nonlinear tidal static effects (where the deformed tidal field of one object perturbs the tidal deformation of the other object), but simply linear self-cross terms.

Now while $v \rightarrow 0$, this equivalence is numerically not true, with $\mathcal{O}(\bar{\lambda}_2 v^{10}) \ll \mathcal{O}(1)$. But as the binary approaches merger, and v is no longer small, then we cannot assume this holds true without further exploration, which we perform here.

To facilitate, we examine truncated versions of the PN Energy and Flux equations keeping just the leading order BBH and Tidal terms,

$$E(v) = -\frac{v v^2}{2} \left(1 + 9\bar{\lambda}_{2A} v^{10} X_A^4 (-1 + X_A) + 9\bar{\lambda}_{2B} v^{10} X_B^4 (-1 + X_B) + \mathcal{O}(v) + \mathcal{O}(\bar{\lambda}_2 v^{11}) \right),$$

$$F(v) = \frac{32v^2v^{10}}{5} \left(1 + 6\bar{\lambda}_{2A}v^{10}X_A^4(3 - 2X_A) + 6\bar{\lambda}_{2B}v^{10}X_B^4(3 - 2X_B) + \mathcal{O}(v) + \mathcal{O}(\bar{\lambda}_2v^{11}) \right). \quad (4.77)$$

Performing the PN series expansion for the TaylorT approximants is the same as before, except we carry it out to the next higher tidal cross terms,

$$\begin{aligned} \mathcal{F}_{\bar{\lambda}_2 \times \bar{\lambda}_2}(v) &= \frac{32v^9}{5M} \left[1 + v^{10} \left(\bar{\lambda}_{2A}X_A^4(72 - 66X_A) + \bar{\lambda}_{2B}X_B^4(72 - 66X_B) \right) \right. \\ &\quad + 324v^{20} \left(\bar{\lambda}_{2A}^2 X_A^8 (12 - 23X_A + 11X_A^2) \right. \\ &\quad + \bar{\lambda}_{2A}\bar{\lambda}_{2B}X_A^4X_B^4(24 - 23(X_A + X_B) + 22X_AX_B) \\ &\quad \left. \left. + \bar{\lambda}_{2B}^2 X_B^8 (12 - 23X_B + 11X_B^2) \right) + \mathcal{O}(v) + \mathcal{O}(\lambda_2v^{11}) + \mathcal{O}(\lambda_2^3v^{30}) \right], \\ \mathcal{T}_{\bar{\lambda}_2 \times \bar{\lambda}_2}(v) &= -\frac{5M}{256v^8} \left[1 + v^{10} \left(\bar{\lambda}_{2A}X_A^4(288 - 264X_A) + \bar{\lambda}_{2B}X_B^4(288 - 264X_B) \right) \right. \\ &\quad + 24v^{20} \left(\bar{\lambda}_{2A}^2 X_A^8 (-36 + 57X_A - 22X_A^2) \right. \\ &\quad + \bar{\lambda}_{2A}\bar{\lambda}_{2B}X_A^4X_B^4(-72 + 57(X_A + X_B) - 44X_AX_B) \\ &\quad \left. \left. + \bar{\lambda}_{2B}^2 X_B^8 (-36 + 57X_B - 22X_B^2) \right) + \mathcal{O}(v) + \mathcal{O}(\lambda_2v^{11}) + \mathcal{O}(\lambda_2^3v^{30}) \right], \\ \mathcal{P}_{\bar{\lambda}_2 \times \bar{\lambda}_2}(v) &= -\frac{1}{32v^5} \left[1 + v^{10} \left(\bar{\lambda}_{2A}X_A^4(72 - 66X_A) + \bar{\lambda}_{2B}X_B^4(72 - 66X_B) \right) \right. \\ &\quad + 12v^{20} \left(\bar{\lambda}_{2A}^2 X_A^8 (-36 + 57X_A - 22X_A^2) \right. \\ &\quad + \bar{\lambda}_{2A}\bar{\lambda}_{2B}X_A^4X_B^4(-72 + 57(X_A + X_B) - 44X_AX_B) + \bar{\lambda}_{2B}^2 X_B^8 (-36 + 57X_B - 22X_B^2) \left. \right) \\ &\quad \left. + \mathcal{O}(v) + \mathcal{O}(\lambda_2v^{11}) + \mathcal{O}(\lambda_2^3v^{30}) \right]. \quad (4.78) \end{aligned}$$

Because these cross terms will most strongly influence the waveform during the final stages of the inspirals, we estimate the size of the effect by comparing the magnitude of the various terms here two different frequencies $\bar{\omega}_{\text{ISCO}} = 6^{-3/2}$ and $\bar{\omega}_{\text{test}} = \bar{\omega}_{\text{ISCO}}/5$. We assume a fiducial binary system where $q = 1$, $\chi_A = \chi_B = 0$, $\bar{\lambda}_{2A} = 1000$, $\bar{\lambda}_{2B} = 0$. The results are displayed in Tables 4.3 and 4.4. We also include the highest PN term of order $\bar{\lambda}_2$ which we've computed (entering at v^{15}), which serves as an error bound estimate arising from the unknown quadrupolar tidal terms. If the self-cross terms are larger than these, or near the size of the LO tidal terms, then we should not neglect them.

At the end of the waveform (*i.e.* at $\bar{\omega}_{\text{ISCO}}$), in the TaylorT4 case, the size of the self-cross terms is an appreciable fraction of the $\bar{\lambda}_2v^{10}$ term and the same size as the $\bar{\lambda}_2v^{15}$ term. This is also true in TaylorT2, but to a lesser extent, as the self-cross terms there are a factor of a few smaller. However, looking just a bit earlier in the inspiral and the self-cross terms drop off until they are distinctly smaller than even $\bar{\lambda}_2v^{15}$. Our general conclusion is that we are fine neglecting the self-cross terms for the time being, but as more tidal terms are introduced, we will eventually need to include this

	$\bar{\omega}_{\text{ISCO}}$	$\bar{\lambda}_2 v_{\text{ISCO}}^{10}$	$\bar{\lambda}_2 v_{\text{ISCO}}^{15}$	$\bar{\lambda}_2^2 v_{\text{ISCO}}^{20}$
$\mathcal{F}_{\text{Tid}}(v)$	$6^{-3/2}$	0.313465	0.0588958	0.0680262
$\mathcal{T}_{\text{Tid}}(v)$	$6^{-3/2}$	1.25386	-0.4286	-0.0201559
$\mathcal{P}_{\text{Tid}}(v)$	$6^{-3/2}$	0.313465	-0.187513	-0.0100779

Table 4.3: Estimating the size of the PN tidal self-cross terms from Eq 4.78, assuming a fiducial system where $q = 1$, $\chi_A = \chi_B = 0$, $\bar{\lambda}_{2A} = 1000$, $\bar{\lambda}_{2B} = 0$, evaluated at $\bar{\omega}_{\text{ISCO}} = 6^{-3/2}$.

	$\bar{\omega}_{\text{test}}$	$\bar{\lambda}_2 v_{\text{test}}^{10}$	$\bar{\lambda}_2 v_{\text{test}}^{15}$	$\bar{\lambda}_2^2 v_{\text{test}}^{20}$
$\mathcal{F}_{\text{Tid}}(v)$	$6^{-3/2}/5$	1.46652×10^{-3}	1.88467×10^{-5}	1.48894×10^{-6}
$\mathcal{T}_{\text{Tid}}(v)$	$6^{-3/2}/5$	5.86608×10^{-3}	-1.37152×10^{-4}	-4.41166×10^{-7}
$\mathcal{P}_{\text{Tid}}(v)$	$6^{-3/2}/5$	1.46652×10^{-3}	-6.0004×10^{-5}	-2.20583×10^{-7}

Table 4.4: Similar to Table 4.3, except evaluated at $\bar{\omega}_{\text{test}} = \bar{\omega}_{\text{ISCO}}/5$.

effect, especially to get the last orbits of the inspiral before contact between the objects and the start of merger/ringdown.

This entire argument generalizes to the octopolar static tides, with $\mathcal{O}(1) \sim \mathcal{O}(\bar{\lambda}_3 v^{14}) \sim \mathcal{O}(\bar{\lambda}_3^2 v^{28})$, yet the octopolar effects are suppressed compared to the quadrupolar static tides. All of the arguments in favor of neglecting the $\mathcal{O}(\bar{\lambda}_2^2 v^{20})$ terms should apply even more strongly to $\mathcal{O}(\bar{\lambda}_3^2 v^{28})$, and so we ignore those effects as well.

Paper Definition Key

Here we define the critical quantities used in the paper for ease of reference.

$A_{\text{Tid}}^{\ell m}(v)$: Tidal Strain Correction, Eq 4.23

α_4 : Undefined Quadrupole Tidal v^4 Flux Coefficient

$\alpha_i^{\ell m}$: Undefined Quadrupole Tidal v^i Strain Coefficient

β_i : Undefined Octopole Tidal v^i Flux Coefficient

$C_A = m_A/R_A$: Compactness of Object A

$E(v)$: PN Energy Expansion, Eq 4.32

$F(v)$: PN Flux Expansion, Eq 4.34

$\mathcal{F}_{\text{BBH}}(v)$: TaylorT4 Expansion of v Evolution BBH Terms, Eq 4.54

$\mathcal{F}_{\text{Tid}}(v)$: TaylorT4 Expansion of v Evolution Tidal Terms, Eq 4.67

$h^{\ell m}(v)$: Waveform Strain Modal Representation

\bar{I}_A : Dimensionless Moment of Inertia, Eq 4.44

- $\kappa_{\ell A}$: Dynamical Tidal Enhancement Factor, Eq 4.28
 $\hat{\kappa}_{2A}$: Dynamical Tidal Strain Enhancement Factor, Eq 4.30
 $\bar{\lambda}_{\ell A}$: ℓ – polar Dimensionless Tidal Deformability, Eq 4.3
 $\bar{\lambda}_{\ell\ell' A}$: Dimensionless Mass Spin-Tidal Coefficient
 m_A : Mass of Object A
 M : Total Mass of Binary
 $\mathcal{P}_{\text{BBH}}(\nu)$: TaylorT2 Expansion of Orbital Phase BBH Terms, Eq 4.58
 $\mathcal{P}_{\text{Tid}}(\nu)$: TaylorT2 Expansion of Orbital Phase Tidal Terms, Eq 4.69
 ϕ : Orbital Phase
 q : Mass Ratio of Binary
 \bar{Q}_A : Dimensionless Rotationally-Induced Quadrupole Moment, Eq 4.35
 R_A : Radius of Object A
 $\bar{\sigma}_{\ell\ell' A}$: Dimensionless Current Spin-Tidal Coefficient
 t : Time
 $\mathcal{T}_{\text{BBH}}(\nu)$: TaylorT2 Expansion of Time BBH Terms, Eq 4.58
 $\mathcal{T}_{\text{Tid}}(\nu)$: TaylorT2 Expansion of Time Tidal Terms, Eq 4.68
 ν : PN Expansion Parameter, Eq 4.1
 $\nu = X_A X_B$: Symmetric Mass Ratio of Binary
 $\bar{\omega}_{f\ell A}$: Dimensionless ℓ – polar f – mode Resonant Frequency, Eq 4.26
 $X_A = m_A/M$: Mass Fraction of Object A
 χ_A : Dimensionless (Aligned) Spin of Object A

Chapter 5

RESONANTING ULTRA-COMPACT OBJECT SPLICING MODEL

5.1 Preface

Gravitational waves serve as a testbed for comparing Beyond GR theories. One of the major hopes for future detections, especially as the field moves towards next generation detectors with ever better sensitivity, is the hope of finding deviations from pure GR within the gravitational wave signals. Because of the current constraints on such theories placed by the signals that have already been detected [5, 8, 9], deviations to pure BBH inspirals are likely to manifest as small corrections to GR.

In this paper, we explore the versatility of the splicing methods, originally introduced in [27], to approximate waveforms for testing theories which deviate from GR. By applying the changes as deviations to the orbital evolution of the energy and flux within the system, spliced waveforms utilize the accuracy of numerically computed BBH waveforms to quickly generated waveforms which are corrected according to Beyond GR theories. We demonstrate the utility of splicing methods by modeling a resonating gravastar and estimating how strong the resonance must be in order to distinguish such a system from BBH waveform.

5.2 Theoretical Framework

Our choice of toy model is to take the black holes in the binary and replace them with gravastars with slightly reflective boundary conditions rather than event horizons, as Ref [111] examined. In particular, they considered a structure where the reflective surface of the gravastar and the effective potential barrier around that object in when in orbit. That structure approximately forms an effective resonant cavity While their work was for extreme mass ratio binaries, we shall use it as a jumping off point for our test.

In particular, they give a leading order correction to the energy flux from the $\ell = 2, m = \pm 2$ mode relative to the standard flux from a black holes as [111],

$$F_{\text{Res}}^{2\pm 2}(v) = F_{\text{BBH}}^{2\pm 2}(v) \left| 1 - \frac{128i\mathcal{R}v^{13}}{15\beta} \right|^2, \quad (5.1)$$

where

$$\beta = 1 + \frac{\mathcal{R}A_{\ell}^{\text{out}}}{A_{\ell}^{\text{in}}} \quad (5.2)$$

is a boundary condition on the reflective horizon, and \mathcal{R} is the reflection coefficient so that $|\mathcal{R}|^2$ is the reflectivity of the energy at the horizon (0 in the case of BH). Here v is still the usual PN parameter related to the (2,2) mode gravitational wave frequency, $\omega^{22} = 2v^3/M$.

Now A_{out}^ℓ and A_{in}^ℓ are related to the asymptotic limits of the Regge-Wheeler function in the Teukolsky perturbation formalism. Ref [124] computed these expressions, expanding them in terms of $\epsilon = 2M\omega^{22}$, which to order $O(\epsilon)$ is

$$\begin{aligned} A_{\text{in}}^{\ell m} &= \frac{(2\ell)!(2\ell+1)!!}{2(\ell-2)!(\ell+2)!} \left(\frac{i}{\epsilon}\right)^{\ell+1} e^{-i\epsilon(\ln 2\epsilon - \alpha_\ell - \beta_\ell)} \left(1 - \frac{\pi}{2}\epsilon + O(\epsilon^2)\right), \\ A_{\text{out}}^{\ell m} &= \frac{(2\ell)!(2\ell+1)!!}{2(\ell-2)!(\ell+2)!} \left(\frac{-i}{\epsilon}\right)^{\ell+1} e^{i\epsilon(\ln 2\epsilon + \alpha_\ell - \beta_\ell)} \left(1 - \frac{\pi}{2}\epsilon + O(\epsilon^2)\right). \end{aligned} \quad (5.3)$$

Here a_ℓ and b_ℓ are both constants, the former of which will disappear from our calculations and the later of which is (after simplifying from their expression)

$$b_\ell = -\gamma + \sum_{k=1}^{\ell-1} \frac{1}{k} + \frac{1}{2\ell} + \frac{(\ell-1)(\ell+3)}{2\ell(\ell+1)}, \quad (5.4)$$

and γ is the Euler constant.

As [124] points out, the amplitudes of $A_{\text{in}}^{\ell m}$ and $A_{\text{out}}^{\ell m}$ are identical up through $O(\epsilon^{2(\ell+1)})$, or in other words, $|A_{\text{in}}^{\ell m}/A_{\text{out}}^{\ell m}| = 1 + O(\epsilon^{2(\ell+1)})$. What remains of that ratio is the phasing information,

$$\frac{A_{\text{out}}^{\ell m}}{A_{\text{in}}^{\ell m}} = (-1)^{\ell+1} e^{i2\epsilon(\ln 2\epsilon + b_\ell)}. \quad (5.5)$$

Then all that is left to compute β is to establish the reflectivity. For our toy model, we choose a simple frequency-dependent reflectivity,

$$\mathcal{R} = (-1)^{\ell+1} R e^{2i\omega^{22}L}, \quad (5.6)$$

where L is the effective length corresponding to the characteristic length of the resonant cavity. Then the expression for β reduces to,

$$\beta = 1 + R e^{2i(L\omega^{22} + 2M\omega^{22}(\ln 4M\omega^{22} + b_\ell))}. \quad (5.7)$$

Examining Eq 5.1 again, we note that because reflectivity term is suppressed by a factor of v^{13} , it will likely be a negligible contribution except when near resonance, *i.e.* β is zero. To get the resonant frequency, we write $\omega^{22} = \omega_R + i\omega_I$, (where $\omega_I \ll \omega_R$), plugging into $\beta = 0$, then solve for the amplitude and phase separately. We find the following conditions on ω_R and ω_I :

$$\begin{aligned} 2\omega_R (L + 2M \ln 4M\omega_R + 4Mb_\ell) &= \pi, 3\pi, 5\pi, \dots, \\ \omega_I &= \frac{\ln R}{2L + 4M \ln 4M\omega_R + 4Mb_\ell}. \end{aligned} \quad (5.8)$$

If we further look at the case $L \gg M$, where the effective length of the resonant cavity is an appreciable fraction of the binary's orbit, then those expressions to reduce to,

$$2L\omega_R \approx \pi, 3\pi, 5\pi, \dots,$$

$$\omega_I \approx \frac{\ln R}{2L}. \quad (5.9)$$

If the system is near resonance, $\omega^{22} = \xi + \omega_R + i\omega_I$ for $\xi \ll \omega_R$, then β looks like

$$\beta = 1 - e^{2iL\xi} \approx -2iL\xi = -2iL[(\omega_{2,2} - \omega_R) - i\omega_I]. \quad (5.10)$$

Since ω_I is small compared to ω_R , that means relative width of β 's behavior near resonance only over a narrow range of frequencies, with a very tight peak. That means we can approximate the behavior of ν in Eq 5.1 as nearly constant, $\nu_R = (M\omega_R/2)^{1/3}$. Lastly, the reflectivity $\mathcal{R} \approx -Re^{2iL\omega_R} \approx R$.

Plugging all this back into Eq 5.1 gives us the resonant behavior of the (2,2) mode energy flux,

$$\begin{aligned} F_{\text{Res}}^{2\pm 2}(\nu) &= F_{\text{BBH}}^{2\pm 2}(\nu) \left| 1 + \frac{\alpha}{\omega^{22} - \omega_R + i\gamma} \right|^2, \\ \alpha &= \frac{128R\nu_R^{13}}{30L}, \\ \gamma &= -\frac{\ln R}{2L}. \end{aligned} \quad (5.11)$$

Because this is just a correction to the (2,2) mode, the total correction to the total energy flux is scaled by its fractional contribution to the total energy, which we can represent as a sum,

$$F_{\text{BBH}}(\nu) = \sum_{\ell m} F_{\text{BBH}}^{\ell m}, \quad (5.12)$$

so the effect of the resonance on the total energy flux is scaled by the fraction of flux in the resonating (2,2) which can resonate, or

$$F_{\text{Res}}(\nu) = F_{\text{BBH}}(\nu) \left[1 + \frac{F_{\text{BBH}}^{22}(\nu)}{F_{\text{BBH}}(\nu)} \left(\left| 1 + \frac{\alpha}{\omega^{22} - \omega_R + i\gamma} \right|^2 - 1 \right) \right]. \quad (5.13)$$

5.3 Splicing Details

We are now ready to set up the system for tidal splicing; in this case, we shall examine this system via the TaylorT4 framework,

$$\mathcal{F}_{\text{BBH}}(\nu) = \frac{F_{\text{BBH}}(\nu)}{M \frac{dE(\nu)}{d\nu}}. \quad (5.14)$$

Now the change in flux due to the resonance does not affect the total energy in the system, $E(\nu)$, merely how fast it is resonating. Thus, when we change $F_{\text{BBH}} \rightarrow F_{\text{Res}}$, then $E(\nu)$ is unchanged, and thus,

$$\mathcal{F}_{\text{Res}}(\nu) = \mathcal{F}_{\text{BBH}}(\nu) \left[1 + \frac{F_{\text{BBH}}^{22}(\nu)}{F_{\text{BBH}}(\nu)} \left(\left| 1 + \frac{\alpha}{\omega^{22} - \omega_R + i\gamma} \right|^2 - 1 \right) \right]. \quad (5.15)$$

With this expression in hand, we can now repeat the same procedure as was done with splicing the NS tidal terms, except instead of Eq 4.56 we use Eq 5.15 after making the usual numerical substitution of $\mathcal{F}_{\text{BBH}} \rightarrow \mathcal{F}_{\text{NR}}$.

The last point of note is the computation of the energy flux fraction contained within the (2,2) mode. Given the modal composition of the strain data at \mathcal{S}^+ , $h^{\ell m}(t)$, then we can write the energy radiated by that mode as [137]

$$F^{\ell m} = \frac{1}{16\pi} \left| \frac{dh^{\ell m}(t)}{dt} \right|^2, \quad (5.16)$$

$$F(v) = \sum_{\ell m} F^{\ell m}.$$

While this sum is supposed to be over all modes, we perform the sum only over the modes provided by the surrogate we are using as our underlying base for generating the BBH waveforms. Even though the surrogate model does not have all modes, they will likely be an insignificant contribution to the energy flux during the inspiral.

A minor technical note: while the form of Eq 5.15 ensures that analytically the splicing integral for $\frac{d\tilde{t}}{dv_{\text{NR}}}$ does not go negative, the extreme sharpness of the resonance peak combined with way we performed the numerical integrals means there is occasionally a data point which goes ever so slightly backwards in time at that peak. We have accounted for this by shifting the time array so that point is barely positive. We expect this to be a negligible effect on the results.

5.4 Test Results

Given this correction to the BBH evolution, we can estimate at when waveforms with this resonant profile will be distinguishable from the pure GR waveforms. In particular, we will examine the waveforms of an equal mass, non-spinning binary with total mass of $30M$ with and without the resonance on 1 member of the binary.

We generated waveforms to cover the range of (2,2) gravitational wave frequencies $f_0 = 10\text{Hz}$ to $f_1 \approx 147\text{Hz}$ (corresponding to an orbital angular frequency of $M\omega_{\text{ISCO}} = 6^{-3/2}$), with the signals windowed with Planck-taper windowing function extending down to 9.5Hz and up to $1.4f_1$ for purposes of facilitating the Fourier transformations.

We compared the differences in the waveforms using the overlap function over the inspiral between 2 signals h_1, h_2 , is given by

$$O(h_1, h_2) = \max_{t_s, \phi_s} \frac{\langle h_1 | h_2 e^{i(\phi_s + 2\pi t_s f)} \rangle}{\sqrt{\langle h_1 | h_1 \rangle \langle h_2 | h_2 \rangle}}, \quad (5.17)$$

where t_s and ϕ_s correspond to the time and phase shift, respectively, between the two waveforms, and the inner product between those two waveforms is computed in the frequency domain,

$$\langle h_1 | h_2 \rangle = 4 \int_{f_0}^{f_1} \frac{h_1(f) \bar{h}_2(f)}{S_n(f)} df. \quad (5.18)$$

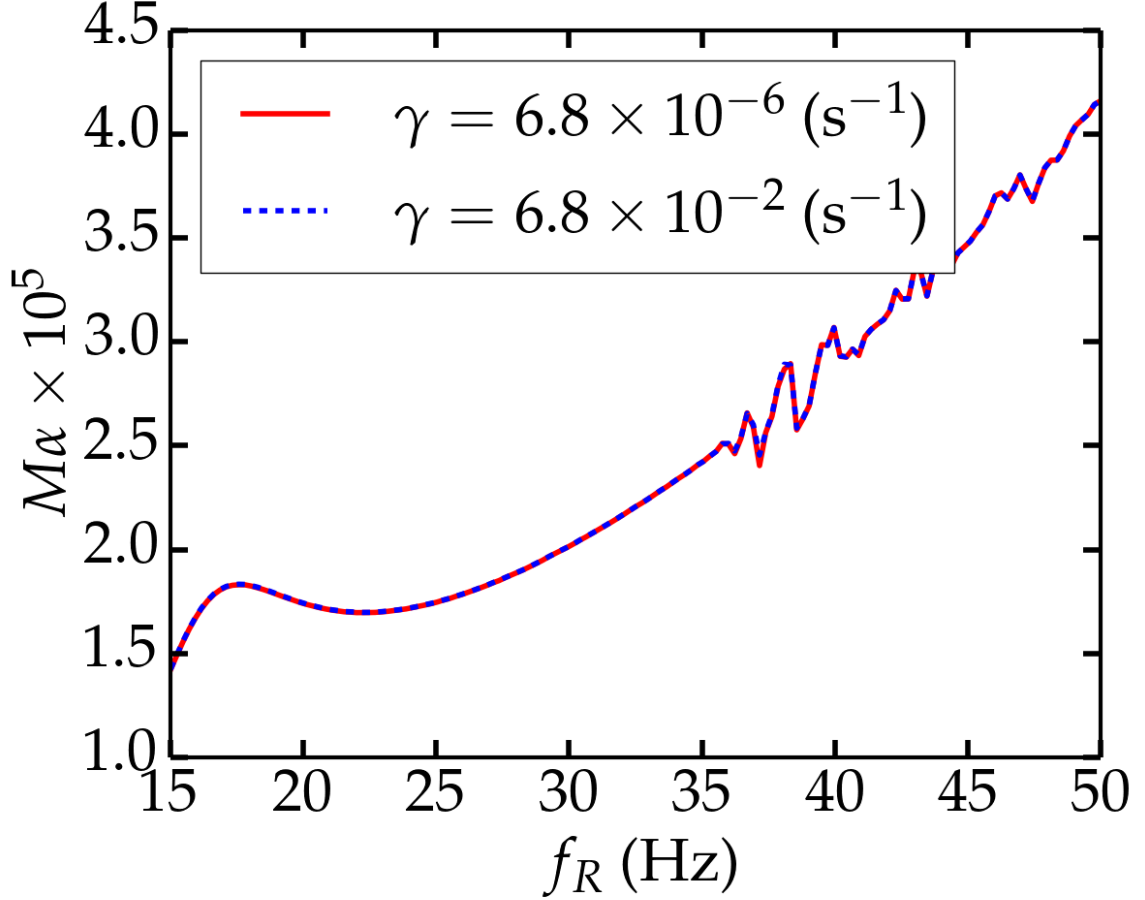


Figure 5.1: The value of $M\alpha$ at which the spliced waveform is distinguishable (overlap $< .97$) from the pure GR inspiral signal, as a function of the other resonant parameters, γ and ω_R . While there is a noticeable affect of $\omega_R = 2\pi f_R$ on the waveform, varying γ barely affects α despite the wide range of γ values shown here.

The integral is weighted by the noise spectrum, $S_n(f)$, which in our case we take to be uniformly flat. Because a vast majority of the waveform's power is in the $(2, \pm 2)$ mode, we simplify our computation by comparing just the $(2, 2)$ mode, assuming optimal orientation for that mode.

Our goal is to estimate an upper limit on the three parameters governing the resonant profile, $(\alpha, \gamma, \omega_R)$. Since of the three, α corresponds to the amplitude of the resonant effect, we generate waveforms various values of γ and ω_R , comparing them with the GR signal to find the α at which the two are distinguishable, which we set to be when the overlap between 2 waveforms drops below .97.

We have plotted the results of α for different values of $\gamma = 6.8 \times 10^{-6} \text{s}^{-1}$, $6.8 \times 10^{-2} \text{s}^{-1}$ (which correspond to dimensionless $M\gamma = 10^{-9}, 10^{-5}$), and a range of $f_R = 15 - 50 \text{Hz}$ in Fig 5.1. From the plot, we see that the estimate of α for which the resonant system is distinguishable is largely independent across a wide range of γ . We interpret this as a consequence of having such a narrow

peak width, $\gamma \ll \omega_R$. In effect, the waveform sweeps through resonance peak quickly enough that it serves as effectively as a blip the frequency evolution. γ governs the exact sharpness of the blip, but the overlap seems not to distinguish much between the blip sharpness over the range we considered. Perhaps γ will have an impact in higher frequencies but the inspiral portion of the waveform is indifferent to the exact shape.

The location of the resonance in the inspiral, ω_R , has a noticeable influence on the signal, with resonance peaks later in the inspiral being easier to distinguish (*i.e.* smaller α) than those appearing earlier by a factor of 2-3. We posit that having the resonance so early in the waveform makes it easier to align for the overlap calculation, especially as the mode amplitude is smaller at lower frequencies. In the limit the resonance peak is far below the lower limit of the detector's band of sensitivity, the waveforms will be indistinguishable. As the peak is deeper into the inspiral, the more disruptive it is to the overall waveform profile.

While we have chosen a particular fiducial mass for our comparisons here which means the waveforms we have considered only extend to a short time before it reaches resonance. One concern of our method is that the effect of the Lorentzian on the evolution may not be bounded in a compact region nearby the resonance peak. Specifically, as the tail of the profile extends to lower frequencies, the orbital evolution lasts for longer spans of time. This can lead to an ever growing accumulation of phase difference between this ultra-compact system and a pure GR evolution even as the resonance profile decays away. As such, we will need to examine the behavior of our approximations at low frequencies and whether a more careful treatment will be necessary to handle the evolution of this system long before resonance.

BIBLIOGRAPHY

- [1] The Spectral Einstein Code. <http://www.black-holes.org/SpEC.html>.
- [2] J. Aasi et al. Advanced LIGO. *Class. Quantum Grav.*, 32:074001, 2015. doi: 10.1088/0264-9381/32/7/074001.
- [3] J. Abadie et al. Predictions for the Rates of Compact Binary Coalescences Observable by Ground-based Gravitational-wave Detectors. *Class. Quantum Grav.*, 27:173001, 2010.
- [4] B. P. Abbott, R. Abbott, T. D. Abbott, F. Acernese, K. Ackley, C. Adams, T. Adams, P. Addesso, R. X. Adhikari, V. B. Adya, and et al. Gravitational Waves and Gamma-Rays from a Binary Neutron Star Merger: GW170817 and GRB 170817A. *"Astrophys. J. Lett."*, 848: L13, October 2017. doi: 10.3847/2041-8213/aa920c.
- [5] B. P. Abbott et al. Tests of General Relativity with GW170817.
- [6] B. P. Abbott et al. GW151226: Observation of Gravitational Waves from a 22-Solar-Mass Binary Black Hole Coalescence. *Phys. Rev. Lett.*, 116(24):241103, 2016. doi: 10.1103/PhysRevLett.116.241103.
- [7] B. P. Abbott et al. Observation of gravitational waves from a binary black hole merger. *Phys. Rev. Lett.*, 116:061102, Feb 2016. doi: 10.1103/PhysRevLett.116.061102. URL <http://link.aps.org/doi/10.1103/PhysRevLett.116.061102>.
- [8] B. P. Abbott et al. Binary Black Hole Mergers in the first Advanced LIGO Observing Run. *Phys. Rev.*, X6(4):041015, 2016. doi: 10.1103/PhysRevX.6.041015.
- [9] B. P. Abbott et al. Tests of general relativity with GW150914. *Phys. Rev. Lett.*, 116:221101, 2016.
- [10] B.. P. Abbott et al. GW170608: Observation of a 19-solar-mass Binary Black Hole Coalescence. *Astrophys. J.*, 851(2):L35, 2017. doi: 10.3847/2041-8213/aa9f0c.
- [11] B. P. Abbott et al. GW170814: A Three-Detector Observation of Gravitational Waves from a Binary Black Hole Coalescence. *Phys. Rev. Lett.*, 119(14):141101, 2017. doi: 10.1103/PhysRevLett.119.141101.
- [12] Benjamin P. Abbott et al. GW170104: Observation of a 50-Solar-Mass Binary Black Hole Coalescence at Redshift 0.2. *Phys. Rev. Lett.*, 118(22):221101, 2017. doi: 10.1103/PhysRevLett.118.221101.
- [13] Benjamin P. Abbott et al. GW170817: Observation of Gravitational Waves from a Binary Neutron Star Inspiral. *Phys. Rev. Lett.*, 119(16):161101, 2017. doi: 10.1103/PhysRevLett.119.161101.
- [14] F. Acernese et al. Advanced Virgo: a second-generation interferometric gravitational wave detector. *Class. Quantum Grav.*, 32(2):024001, 2015. doi: 10.1088/0264-9381/32/2/024001.
- [15] J. C. Adams and P. N. Swartztrauber. Spherepack 3.0. <http://www.scd.ucar.edu/css/software/spherepack>.

- [16] Michalis Agathos, Jeroen Meidan, Walter Del Pozzo, Tjonnie G. F. Li, Marco Tompitak, John Veitch, Salvatore Vitale, and Chris Van Den Broeck. Constraining the neutron star equation of state with gravitational wave signals from coalescing binary neutron stars. *Phys. Rev. D*, 92:023012, 2015. doi: 10.1103/PhysRevD.92.023012.
- [17] P. Ajith et al. The NINJA-2 catalog of hybrid post-Newtonian/numerical-relativity waveforms for non-precessing black-hole binaries. *Class. Quant. Grav.*, 29:124001, 2012. doi: 10.1088/0264-9381/30/19/199401,10.1088/0264-9381/29/12/124001. [Erratum: *Class. Quant. Grav.*30,199401(2013)].
- [18] K. G. Arun, L. Blanchet, B. R. Iyer, and M. S. S. Qusailah. The 2.5PN gravitational wave polarizations from inspiralling compact binaries in circular orbits. *Class. Quantum Grav.*, 21:3771–3801, August 2004. doi: 10.1088/0264-9381/21/15/010.
- [19] Yoichi Aso, Yuta Michimura, Kentaro Somiya, Masaki Ando, Osamu Miyakawa, Takanori Sekiguchi, Daisuke Tatsumi, and Hiroaki Yamamoto. Interferometer design of the kagra gravitational wave detector. *Phys. Rev. D*, 88:043007, Aug 2013. doi: 10.1103/PhysRevD.88.043007. URL <http://link.aps.org/doi/10.1103/PhysRevD.88.043007>.
- [20] Benjamin Aylott, John G. Baker, William D. Boggs, Michael Boyle, Patrick R. Brady, et al. Testing gravitational-wave searches with numerical relativity waveforms: Results from the first Numerical INJection Analysis (NINJA) project. *Class. Quantum Grav.*, 26:165008, 2009. doi: 10.1088/0264-9381/26/16/165008.
- [21] M. C. Babiuc, B. Szilágyi, J. Winicour, and Y. Zlochower. A characteristic extraction tool for gravitational waveforms. *Phys. Rev. D*, 84:044057, Aug 2011. doi: 10.1103/PhysRevD.84.044057. URL <http://link.aps.org/doi/10.1103/PhysRevD.84.044057>.
- [22] Maria Babiuc, Béla Szilágyi, Ian Hawke, and Yosef Zlochower. Gravitational wave extraction based on Cauchy-characteristic extraction and characteristic evolution. *Class. Quantum Grav.*, 22(23):5089–5107, 2005. URL <http://stacks.iop.org/0264-9381/22/5089>.
- [23] Maria C. Babiuc, Nigel T. Bishop, Béla Szilágyi, and Jeffrey Winicour. Strategies for the characteristic extraction of gravitational waveforms. *Phys. Rev. D*, 79:084011, 2009.
- [24] L. Baiotti, T. Damour, B. Giacomazzo, A. Nagar, and L. Rezzolla. Accurate numerical simulations of inspiralling binary neutron stars and their comparison with effective-one-body analytical models. *Phys. Rev. D*, 84(2):024017, July 2011. doi: 10.1103/PhysRevD.84.024017.
- [25] Luca Baiotti, Thibault Damour, Bruno Giacomazzo, Alessandro Nagar, and Luciano Rezzolla. Analytic modelling of tidal effects in the relativistic inspiral of binary neutron stars. *Phys. Rev. Lett.*, 105:261101, 2010. doi: 10.1103/PhysRevLett.105.261101.
- [26] John G. Baker, Joan Centrella, Dae-II Choi, Michael Koppitz, and James van Meter. Binary black hole merger dynamics and waveforms. *Phys. Rev. D*, 73(10):104002, 2006. doi: 10.1103/PhysRevD.73.104002. URL <http://link.aps.org/abstract/PRD/v73/e104002>.
- [27] K. Barkett, M. A. Scheel, R. Haas, C. D. Ott, S. Bernuzzi, D. A. Brown, B. Szilágyi, J. D. Kaplan, J. Lippuner, C. D. Muhlberger, F. Foucart, and M. D. Duez. Gravitational waveforms for neutron star binaries from binary black hole simulations. *Phys. Rev. D*, 93:044064, Feb

2016. doi: 10.1103/PhysRevD.93.044064. URL <http://link.aps.org/doi/10.1103/PhysRevD.93.044064>.
- [28] S. Bernuzzi, A. Nagar, M. Thierfelder, and B. Brügmann. Tidal effects in binary neutron star coalescence. *Phys. Rev. D*, 86(4):044030, August 2012. doi: 10.1103/PhysRevD.86.044030.
- [29] S. Bernuzzi, A. Nagar, T. Dietrich, and T. Damour. Modeling the Dynamics of Tidally Interacting Binary Neutron Stars up to the Merger. *Phys. Rev. Lett.*, 114(16):161103, April 2015. doi: 10.1103/PhysRevLett.114.161103.
- [30] Sebastiano Bernuzzi, Marcus Thierfelder, and Bernd Bruegmann. Accuracy of numerical relativity waveforms from binary neutron star mergers and their comparison with post-Newtonian waveforms. *Phys. Rev. D*, 85:104030, 2012. doi: 10.1103/PhysRevD.85.104030.
- [31] Sebastiano Bernuzzi, Alessandro Nagar, Simone Balmelli, Tim Dietrich, and Maximiliano Ujevic. Quasiuniversal properties of neutron star mergers. *Phys. Rev. Lett.*, 112:201101, 2014. doi: 10.1103/PhysRevLett.112.201101.
- [32] S. Bhagwat, M. Okounkova, S. W. Ballmer, D. A. Brown, M. Giesler, M. A. Scheel, and S. A. Teukolsky. On choosing the start time of binary black hole ringdown. *ArXiv e-prints*, November 2017.
- [33] Donato Bini and Thibault Damour. Gravitational self-force corrections to two-body tidal interactions and the effective one-body formalism. *Phys. Rev. D*, 90:124037, 2014. doi: 10.1103/PhysRevD.90.124037.
- [34] Donato Bini, Thibault Damour, and Guillaume Faye. Effective action approach to higher-order relativistic tidal interactions in binary systems and their effective one body description. *Phys. Rev. D*, 85:124034, 2012. doi: 10.1103/PhysRevD.85.124034.
- [35] N. T. Bishop, R. Gomez, L. Lehner, M. Maharaj, and J. Winicour. High-powered gravitational news. *Phys. Rev. D*, 56:6298–6309, 1997. doi: 10.1103/PhysRevD.56.6298.
- [36] N. T. Bishop, R. Gómez, R. A. Isaacson, L. Lehner, B. Szilágyi, and J. Winicour. Cauchy-characteristic matching. In Bala R. Iyer and Biplab Bhawal, editors, *Black Holes, Gravitational Radiation and the Universe*, chapter 24. Kluwer, Dordrecht, 1998.
- [37] Nigel Bishop, Denis Pollney, and Christian Reisswig. Initial data transients in binary black hole evolutions. *Class. Quantum Grav.*, 28:155019, 2011. doi: 10.1088/0264-9381/28/15/155019.
- [38] Nigel T. Bishop. Linearized solutions of the einstein equations within a bondi–sachs framework, and implications for boundary conditions in numerical simulations. *Class. Quantum Grav.*, 22:2393, 2005. URL <http://stacks.iop.org/0264-9381/22/i=12/a=006>.
- [39] Nigel T. Bishop, Roberto Gómez, Luis Lehner, and Jeffrey Winicour. Cauchy-characteristic extraction in numerical relativity. *Phys. Rev. D*, 54(10):6153–6165, Nov 1996. doi: 10.1103/PhysRevD.54.6153. URL <http://link.aps.org/abstract/PRD/v54/p6153>.
- [40] J. Blackman, S. E. Field, C. R. Galley, B. Szilágyi, M. A. Scheel, M. Tiglio, and D. A. Hemberger. Fast and Accurate Prediction of Numerical Relativity Waveforms from Binary Black Hole Coalescences Using Surrogate Models. *Phys. Rev. Lett.*, 115(12):121102, September 2015. doi: 10.1103/PhysRevLett.115.121102.

- [41] Jonathan Blackman, Scott E. Field, Mark A. Scheel, Chad R. Galley, Daniel A. Hemberger, Patricia Schmidt, and Rory Smith. A Surrogate Model of Gravitational Waveforms from Numerical Relativity Simulations of Precessing Binary Black Hole Mergers. *Phys. Rev.*, D95(10):104023, 2017. doi: 10.1103/PhysRevD.95.104023.
- [42] Jonathan Blackman, Scott E. Field, Mark A. Scheel, Chad R. Galley, Christian D. Ott, Michael Boyle, Lawrence E. Kidder, Harald P. Pfeiffer, and Béla Szilágyi. Numerical relativity waveform surrogate model for generically precessing binary black hole mergers. *Phys. Rev.*, D96(2):024058, 2017. doi: 10.1103/PhysRevD.96.024058.
- [43] Luc Blanchet. Gravitational Radiation from Post-Newtonian Sources and Inspiralling Compact Binaries. *Living Rev. Rel.*, 17:2, 2014. doi: 10.12942/lrr-2014-2.
- [44] Luc Blanchet. Gravitational Radiation from Post-Newtonian Sources and Inspiralling Compact Binaries. *Living Rev. Rel.*, 17:2, 2014. doi: 10.12942/lrr-2014-2.
- [45] Luc Blanchet and Guillaume Faye. General relativistic dynamics of compact binaries at the third postNewtonian order. *Phys. Rev.*, D63:062005, 2001. doi: 10.1103/PhysRevD.63.062005.
- [46] Luc Blanchet and Gerhard Schäfer. Gravitational wave tails and binary star systems. *Class. Quantum Grav.*, 10(12):2699–2721, 1993. URL <http://stacks.iop.org/0264-9381/10/2699>.
- [47] Luc Blanchet, Guillaume Faye, Bala R. Iyer, and Benoit Joguet. Gravitational-wave inspiral of compact binary systems to $7/2$ post-Newtonian order. *Phys. Rev. D*, 65(6):061501, Feb 2002. doi: 10.1103/PhysRevD.65.061501. URL <http://link.aps.org/abstract/PRD/v65/e061501>. Erratum: [50].
- [48] Luc Blanchet, Thibault Damour, Gilles Esposito-Farese, and Bala R. Iyer. Gravitational radiation from inspiralling compact binaries completed at the third post-Newtonian order. *Phys. Rev. Lett.*, 93:091101, 2004. doi: 10.1103/PhysRevLett.93.091101.
- [49] Luc Blanchet, Thibault Damour, Gilles Esposito-Farèse, and Bala R. Iyer. Dimensional regularization of the third post-Newtonian gravitational wave generation from two point masses. *Phys. Rev. D*, 71(12):124004, 2005. doi: 10.1103/PhysRevD.71.124004. URL <http://link.aps.org/abstract/PRD/v71/e124004>.
- [50] Luc Blanchet, Guillaume Faye, Bala R. Iyer, and Benoit Joguet. Erratum: Gravitational-wave inspiral of compact binary systems to $7/2$ post-Newtonian order. *Phys. Rev. D*, 71(12):129902, 2005. doi: 10.1103/PhysRevD.71.129902. URL <http://link.aps.org/abstract/PRD/v71/e129902>.
- [51] Luc Blanchet, Alessandra Buonanno, and Guillaume Faye. Higher-order spin effects in the dynamics of compact binaries. II. Radiation field. *Phys. Rev. D*, 74(10):104034, 2006. doi: 10.1103/PhysRevD.74.104034. URL <http://link.aps.org/abstract/PRD/v74/e104034>.
- [52] Luc Blanchet, Guillaume Faye, Bala R. Iyer, and Siddhartha Sinha. The Third post-Newtonian gravitational wave polarisations and associated spherical harmonic modes for inspiralling compact binaries in quasi-circular orbits. *Class. Quantum Grav.*, 25:165003, 2008. doi: 10.1088/0264-9381/25/16/165003.

- [53] Alejandro Bohé, Lijing Shao, Andrea Taracchini, Alessandra Buonanno, Stanislav Babak, Ian W. Harry, Ian Hinder, Serguei Ossokine, Michael Pürrer, Vivien Raymond, Tony Chu, Heather Fong, Prayush Kumar, Harald P. Pfeiffer, Michael Boyle, Daniel A. Hemberger, Lawrence E. Kidder, Geoffrey Lovelace, Mark A. Scheel, and Béla Szilágyi. Improved effective-one-body model of spinning, nonprecessing binary black holes for the era of gravitational-wave astrophysics with advanced detectors. *Phys. Rev. D*, 95:044028, Feb 2017. doi: 10.1103/PhysRevD.95.044028. URL <https://link.aps.org/doi/10.1103/PhysRevD.95.044028>.
- [54] H. Bondi, M. G. J. van der Burg, and A. W. K. Metzner. Gravitational waves in general relativity VII. Waves from axi-symmetric isolated systems. *Proc. R. Soc. Lond. A*, 269:21–52, 1962.
- [55] J. P. Boyd. *Chebyshev and Fourier Spectral Methods*. Springer-Verlag, Berlin, 1989.
- [56] M. Boyle, A. Buonanno, L. E. Kidder, A. H. Mroué, Y. Pan, H. P. Pfeiffer, and M. A. Scheel. High-accuracy numerical simulation of black-hole binaries: Computation of the gravitational-wave energy flux and comparisons with post-Newtonian approximants. *Phys. Rev. D*, 78:104020, 2008. doi: 10.1103/PhysRevD.78.104020.
- [57] Michael Boyle and Abdul H. Mroué. Extrapolating gravitational-wave data from numerical simulations. *Phys. Rev. D*, 80(12):124045–14, December 2009. doi: 10.1103/PhysRevD.80.124045. URL <http://link.aps.org/abstract/PRD/v80/e124045>.
- [58] Michael Boyle, Duncan A. Brown, Lawrence E. Kidder, Abdul H. Mroue, Harald P. Pfeiffer, Mark A. Scheel, Gregory B. Cook, and Saul A. Teukolsky. High-accuracy comparison of numerical relativity simulations with post-Newtonian expansions. *Phys. Rev.*, D76:124038, 2007. doi: 10.1103/PhysRevD.76.124038.
- [59] Alessandra Buonanno, Bala Iyer, Evan Ochsner, Yi Pan, and B. S. Sathyaprakash. Comparison of post-Newtonian templates for compact binary inspiral signals in gravitational-wave detectors. *Phys. Rev.*, D80:084043, 2009. doi: 10.1103/PhysRevD.80.084043.
- [60] M. Campanelli, C. O. Lousto, P. Marronetti, and Y. Zlochower. Accurate evolutions of orbiting black-hole binaries without excision. *Phys. Rev. Lett.*, 96:111101, 2006. doi: 10.1103/PhysRevLett.96.111101.
- [61] K. Chakravarti, A. Gupta, S. Bose, M. D. Duez, J. Caro, W. Brege, F. Foucart, S. Ghosh, K. Kyutoku, B. D. Lackey, M. Shibata, D. A. Hemberger, L. E. Kidder, H. P. Pfeiffer, and M. A. Scheel. Systematic effects from black hole-neutron star waveform model uncertainties on the neutron star equation of state. *ArXiv e-prints*, September 2018.
- [62] T. K. Chan, Y.-H. Sham, P. T. Leung, and L.-M. Lin. Multipolar universal relations between f -mode frequency and tidal deformability of compact stars. *Phys. Rev. D*, 90:124023, Dec 2014. doi: 10.1103/PhysRevD.90.124023. URL <https://link.aps.org/doi/10.1103/PhysRevD.90.124023>.
- [63] J. Clark, L. Cadonati, J. Healy, I.S. Heng, J. Logue, N. Mangini, L. London, L. Pekowsky, and D. Shoemaker. Investigating binary black hole mergers with principal component analysis. In Carlos F. Sopuerta, editor, *Gravitational Wave Astrophysics*, volume 40 of *Astrophysics and Space Science Proceedings*, pages 281–287. Springer International Publishing, Cham,

- Switzerland, 2015. ISBN 978-3-319-10487-4. doi: 10.1007/978-3-319-10488-1_24. URL http://dx.doi.org/10.1007/978-3-319-10488-1_24.
- [64] T. Damour, P. Jaranowski, and G. Schäfer. Dimensional regularization of the gravitational interaction of point masses. *Physics Letters B*, 513:147–155, July 2001. doi: 10.1016/S0370-2693(01)00642-6.
- [65] T. Damour, A. Nagar, and L. Villain. Measurability of the tidal polarizability of neutron stars in late-inspiral gravitational-wave signals. *Phys. Rev. D*, 85(12):123007, June 2012. doi: 10.1103/PhysRevD.85.123007.
- [66] Thibault Damour and Alessandro Nagar. Effective One Body description of tidal effects in inspiralling compact binaries. *Phys. Rev. D*, 81:084016, 2010. doi: 10.1103/PhysRevD.81.084016.
- [67] Thibault Damour, Bala R. Iyer, and B. S. Sathyaprakash. Frequency-domain P-approximant filters for time-truncated inspiral gravitational wave signals from compact binaries. *Phys. Rev. D*, 62(8):084036, Sep 2000. doi: 10.1103/PhysRevD.62.084036. URL <http://link.aps.org/abstract/PRD/v62/e084036>.
- [68] Thibault Damour, Bala R. Iyer, and B.S. Sathyaprakash. A Comparison of search templates for gravitational waves from binary inspiral. *Phys. Rev. D*, 63:044023, 2001.
- [69] Thibault Damour, Bala R. Iyer, and B. S. Sathyaprakash. Comparison of search templates for gravitational waves from binary inspiral: 3.5PN update. *Phys. Rev. D*, 66(2):027502, Jul 2002. doi: 10.1103/PhysRevD.66.027502. URL <http://link.aps.org/abstract/PRD/v66/e027502>. Erratum: [70].
- [70] Thibault Damour, Bala R. Iyer, and B. S. Sathyaprakash. Erratum: Comparison of search templates for gravitational waves from binary inspiral: 3.5PN update. *Phys. Rev. D*, 72(2):029901, 2005. doi: 10.1103/PhysRevD.72.029901. URL <http://link.aps.org/abstract/PRD/v72/e029901>.
- [71] Vanessa C. de Andrade, Luc Blanchet, and Guillaume Faye. Third post-Newtonian dynamics of compact binaries: Noetherian conserved quantities and equivalence between the harmonic-coordinate and ADM-Hamiltonian formalisms. *Class. Quantum Grav.*, 18(5):753–778, 2001. URL <http://stacks.iop.org/0264-9381/18/753>.
- [72] W. Del Pozzo, T. G. F. Li, M. Agathos, C. Van Den Broeck, and S. Vitale. Demonstrating the Feasibility of Probing the Neutron-Star Equation of State with Second-Generation Gravitational-Wave Detectors. *Phys. Rev. Lett.*, 111(7):071101, August 2013. doi: 10.1103/PhysRevLett.111.071101.
- [73] Tim Dietrich and Tanja Hinderer. Comprehensive comparison of numerical relativity and effective-one-body results to inform improvements in waveform models for binary neutron star systems. *Phys. Rev. D*, 95:124006, Jun 2017. doi: 10.1103/PhysRevD.95.124006. URL <https://link.aps.org/doi/10.1103/PhysRevD.95.124006>.
- [74] Tim Dietrich, Sebastian Khan, Reetika Dudi, Shasvath J. Kapadia, Prayush Kumar, Alessandro Nagar, Frank Ohme, Francesco Pannarale, Anuradha Samajdar, Sebastiano Bernuzzi, Gregorio Carullo, Walter Del Pozzo, Maria Haney, Charalampos Markakis, Michael Puerrer,

- Gunnar Riemenschneider, Yoshinta Eka Setyawati, Ka Wa Tsang, and Chris Van Den Broeck. Matter imprints in waveform models for neutron star binaries: tidal and self-spin effects.
- [75] Tim Dietrich, Sebastiano Bernuzzi, and Wolfgang Tichy. Closed-form tidal approximants for binary neutron star gravitational waveforms constructed from high-resolution numerical relativity simulations. *Phys. Rev.*, D96(12):121501, 2017. doi: 10.1103/PhysRevD.96.121501.
- [76] Matthew D. Duez, Francois Foucart, Lawrence E. Kidder, Harald P. Pfeiffer, Mark A. Scheel, and Saul A. Teukolsky. Evolving black hole-neutron star binaries in general relativity using pseudospectral and finite difference methods. *Phys. Rev. D*, 78(10):104015, November 2008. doi: 10.1103/PhysRevD.78.104015.
- [77] Marc Favata. Systematic parameter errors in inspiraling neutron star binaries. *Phys. Rev. Lett.*, 112:101101, 2014. doi: 10.1103/PhysRevLett.112.101101.
- [78] S. E. Field, C. R. Galley, J. S. Hesthaven, J. Kaye, and M. Tiglio. Fast Prediction and Evaluation of Gravitational Waveforms Using Surrogate Models. *Phys. Rev. X*, 4(3):031006, July 2014. doi: 10.1103/PhysRevX.4.031006.
- [79] David R. Fiske, John G. Baker, James R. van Meter, Dae-II Choi, and Joan M. Centrella. Wave zone extraction of gravitational radiation in three-dimensional numerical relativity. *Phys. Rev. D*, 71(10):104036, 2005. doi: 10.1103/PhysRevD.71.104036. URL <http://link.aps.org/abstract/PRD/v71/e104036>.
- [80] É. É. Flanagan and T. Hinderer. Constraining neutron-star tidal Love numbers with gravitational-wave detectors. *Phys. Rev. D*, 77(2):021502, January 2008. doi: 10.1103/PhysRevD.77.021502.
- [81] F. Foucart, L. Buchman, M. D. Duez, M. Grudich, L. E. Kidder, I. MacDonald, A. Mroue, H. P. Pfeiffer, M. A. Scheel, and B. Szilágyi. First direct comparison of nondisrupting neutron star-black hole and binary black hole merger simulations. *Phys. Rev. D*, 88(6):064017, September 2013.
- [82] F. Foucart, M. B. Deaton, M. D. Duez, L. E. Kidder, I. MacDonald, C. D. Ott, H. P. Pfeiffer, M. A. Scheel, B. Szilágyi, and S. A. Teukolsky. Black hole-neutron star mergers at realistic mass ratios: Equation of state and spin orientation effects. *Phys. Rev. D*, 87:084006, March 2013.
- [83] F. Foucart, M. D. Duez, T. Hinderer, J. Caro, A. R. Williamson, M. Boyle, A. Buonanno, R. Haas, D. A. Hemberger, L. E. Kidder, H. P. Pfeiffer, and M. A. Scheel. Gravitational waveforms from SpEC simulations : neutron star-neutron star and low-mass black hole-neutron star binaries. 2018.
- [84] J. N. Goldberg, A. J. Macfarlane, E. T. Newman, F. Rohrlich, and E. C. G. Sudarshan. Spin- s spherical harmonics and δ . *Journal of Mathematical Physics*, 8(11):2155–2161, 1967. doi: 10.1063/1.1705135. URL <http://link.aip.org/link/?JMP/8/2155/1>.
- [85] R. Gómez, L. Lehner, P. Papadopoulos, and J. Winicour. The eth formalism in numerical relativity. *Class. Quantum Grav.*, 01 1997.

- [86] R. Haas, C. D. Ott, B. Szilágyi, J. D. Kaplan, J. Lippuner, M. A. Scheel, K. Barkett, C. D. Muhlberger, T. Dietrich, M. D. Duez, F. Foucart, H. P. Pfeiffer, L. E. Kidder, and S. A. Teukolsky. Simulations of inspiraling and merging double neutron stars using the Spectral Einstein Code. *Phys. Rev. D*, D93(12):124062, April 2016. doi: 10.1103/PhysRevD.93.124062.
- [87] C. J. Handmer and B. Szilágyi. Spectral characteristic evolution: A new algorithm for gravitational wave propagation. *Class. Quantum Grav.*, 32:025008, 2015.
- [88] C. J. Handmer, B. Szilágyi, and J. Winicour. Gauge invariant spectral Cauchy characteristic extraction. *Class. Quantum Grav.*, 32(23):235018, December 2015. doi: 10.1088/0264-9381/32/23/235018.
- [89] Casey J. Handmer, Béla Szilágyi, and Jeffrey Winicour. Spectral Cauchy Characteristic Extraction of strain, news and gravitational radiation flux. *Class. Quant. Grav.*, 33(22):225007, 2016. doi: 10.1088/0264-9381/33/22/225007.
- [90] Mark Hannam, Sascha Husa, Bernd Brügmann, and Achamveedu Gopakumar. Comparison between numerical-relativity and post-Newtonian waveforms from spinning binaries: the orbital hang-up case. *Phys. Rev. D*, 78:104007, 2008.
- [91] Mark Hannam, Sascha Husa, Frank Ohme, Doreen Muller, and Bernd Brügmann. Simulations of black-hole binaries with unequal masses or nonprecessing spins: Accuracy, physical properties, and comparison with post-Newtonian results. *Phys. Rev. D*, 82:124008, 2010. doi: 10.1103/PhysRevD.82.124008.
- [92] James Healy, Pablo Laguna, and Deirdre Shoemaker. Decoding the final state in binary black hole mergers. *Class. Quantum Grav.*, 31(21):212001, 2014. doi: 10.1088/0264-9381/31/21/212001.
- [93] Ian Hinder et al. Error-analysis and comparison to analytical models of numerical waveforms produced by the NRAR Collaboration. *Class. Quantum Grav.*, 31(2):025012, 2014.
- [94] T. Hinderer, B. D. Lackey, R. N. Lang, and J. S. Read. Tidal deformability of neutron stars with realistic equations of state and their gravitational wave signatures in binary inspiral. *Phys. Rev. D*, 81(12):123016, June 2010. doi: 10.1103/PhysRevD.81.123016.
- [95] T. Hinderer, A. Taracchini, F. Foucart, A. Buonanno, J. Steinhoff, M. Duez, L. E. Kidder, H. P. Pfeiffer, M. A. Scheel, B. Szilágyi, K. Hotokezaka, K. Kyutoku, M. Shibata, and C. W. Carpenter. Effects of neutron-star dynamic tides on gravitational waveforms within the effective-one-body approach. *Phys. Rev. Lett.*, 116(18):181101, 2016. doi: 10.1103/PhysRevLett.116.181101.
- [96] Tanja Hinderer et al. Effects of neutron-star dynamic tides on gravitational waveforms within the effective-one-body approach. *Phys. Rev. Lett.*, 116(18):181101, 2016. doi: 10.1103/PhysRevLett.116.181101.
- [97] Tanja Hinderer et al. Discerning the binary neutron star or neutron star-black hole nature of GW170817 with Gravitational Wave and Electromagnetic Measurements. 2018.
- [98] Kenta Hotokezaka, Koutarou Kyutoku, and Masaru Shibata. Exploring tidal effects of coalescing binary neutron stars in numerical relativity. *Phys. Rev. D*, 87(4):044001, 2013. doi: 10.1103/PhysRevD.87.044001.

- [99] Kenta Hotokezaka, Koutarou Kyutoku, Hirotada Okawa, and Masaru Shibata. Exploring tidal effects of coalescing binary neutron stars in numerical relativity II: Longterm simulations. *Phys. Rev. D*, 91(6):064060, 2015. doi: 10.1103/PhysRevD.91.064060.
- [100] Huffenberger, Kevin M and Wandelt, Benjamin D. Fast and exact spin-s spherical harmonic transforms. *Astro. J. Sup. Ser.*, 189:255–260, 2010.
- [101] Sascha Husa, Sebastian Khan, Mark Hannam, Michael Pürrer, Frank Ohme, Xisco Jiménez Forteza, and Alejandro Bohé. Frequency-domain gravitational waves from non-precessing black-hole binaries. I. New numerical waveforms and anatomy of the signal. *Phys. Rev.*, D93(4):044006, 2016. doi: 10.1103/PhysRevD.93.044006.
- [102] Piotr Jaranowski and Gerhard Schäfer. Binary black-hole problem at the third post-Newtonian approximation in the orbital motion: Static part. *Phys. Rev. D*, 60(12):124003, Nov 1999. doi: 10.1103/PhysRevD.60.124003. URL <http://link.aps.org/abstract/PRD/v60/e124003>.
- [103] Kyohei Kawaguchi, Koutarou Kyutoku, Hiroyuki Nakano, Hirotada Okawa, Masaru Shibata, and Keisuke Taniguchi. Black hole-neutron star binary merger: Dependence on black hole spin orientation and equation of state. *Phys. Rev. D*, 92(2):024014, July 2015. doi: 10.1103/PhysRevD.92.024014.
- [104] Sebastian Khan, Sascha Husa, Mark Hannam, Frank Ohme, Michael Pürrer, Xisco Jiménez Forteza, and Alejandro Bohé. Frequency-domain gravitational waves from non-precessing black-hole binaries. II. A phenomenological model for the advanced detector era. *Phys. Rev.*, D93(4):044007, 2016. doi: 10.1103/PhysRevD.93.044007.
- [105] Lawrence E. Kidder. Coalescing binary systems of compact objects to postNewtonian 5/2 order. 5. Spin effects. *Phys. Rev.*, D52:821–847, 1995. doi: 10.1103/PhysRevD.52.821.
- [106] Lawrence E. Kidder. Using full information when computing modes of post-Newtonian waveforms from inspiralling compact binaries in circular orbit. *Phys. Rev. D*, 77:044016, 2008. doi: 10.1103/PhysRevD.77.044016.
- [107] Prayush Kumar, Michael Pürrer, and Harald P. Pfeiffer. Measuring neutron star tidal deformability with Advanced LIGO: a Bayesian analysis of neutron star - black hole binary observations. *Phys. Rev.*, D95(4):044039, 2017. doi: 10.1103/PhysRevD.95.044039.
- [108] B. D. Lackey and L. Wade. Reconstructing the neutron-star equation of state with gravitational-wave detectors from a realistic population of inspiralling binary neutron stars. *Phys. Rev. D*, 91:043002, October 2015. doi: 10.1103/PhysRevD.91.043002.
- [109] Benjamin D. Lackey, Koutarou Kyutoku, Masaru Shibata, Patrick R. Brady, and John L. Friedman. Extracting equation of state parameters from black hole-neutron star mergers: aligned-spin black holes and a preliminary waveform model. *Phys. Rev. D*, 89(4):043009, 2014. doi: 10.1103/PhysRevD.89.043009.
- [110] Philippe Landry. Rotational-tidal phasing of the binary neutron star waveform. 2018.
- [111] Chao Li and Geoffrey Lovelace. A Generalization of Ryan’s theorem: Probing tidal coupling with gravitational waves from nearly circular, nearly equatorial, extreme-mass-ratio inspirals. *Phys. Rev. D*, 77:064022, 2008. doi: 10.1103/PhysRevD.77.064022.

- [112] L. Lindblom, M. A. Scheel, L. E. Kidder, R. Owen, and O. Rinne. A new generalized harmonic evolution system. *Class. Quantum Grav.*, 23:S447, August 2006. doi: 10.1088/0264-9381/23/16/S09.
- [113] Chris Loken, Daniel Gruner, Leslie Groer, Richard Peltier, Neil Bunn, Michael Craig, Teresa Henriques, Jillian Dempsey, Ching-Hsing Yu, Joseph Chen, L. Jonathan Dursi, Jason Chong, Scott Northrup, Jaime Pinto, Neil Knecht, and Ramses Van Zon. SciNet: Lessons Learned from Building a Power-efficient Top-20 System and Data Centre. *J. Phys.: Conf. Ser.*, 256: 012026, 2010. doi: 10.1088/1742-6596/256/1/012026.
- [114] G. Lovelace, M. D. Duez, F. Foucart, L. E. Kidder, H. P. Pfeiffer, M. A. Scheel, and B. Szilágyi. Massive disc formation in the tidal disruption of a neutron star by a nearly extremal black hole. *Class. Quantum Grav.*, 30(13):135004, July 2013. doi: 10.1088/0264-9381/30/13/135004.
- [115] Ilana MacDonald, Samaya Nisanke, and Harald P. Pfeiffer. Suitability of post-Newtonian/numerical-relativity hybrid waveforms for gravitational wave detectors. *Class. Quantum Grav.*, 28(13):134002, July 2011. ISSN 0264-9381. doi: 10.1088/0264-9381/28/13/134002. URL <http://iopscience.iop.org/0264-9381/28/13/134002/>.
- [116] Andrea Maselli, Leonardo Gualtieri, and Valeria Ferrari. Constraining the equation of state of nuclear matter with gravitational wave observations: Tidal deformability and tidal disruption. *Phys. Rev. D*, 88(10):104040, 2013. doi: 10.1103/PhysRevD.88.104040.
- [117] D.J.A. McKechnan, C. Robinson, and B.S. Sathyaprakash. A tapering window for time-domain templates and simulated signals in the detection of gravitational waves from coalescing compact binaries. *Class. Quantum Grav.*, 27:084020, 2010. doi: 10.1088/0264-9381/27/8/084020.
- [118] E. T. Newman and R. Penrose. Note on the Bondi–Metzner–Sachs group. *J. Math. Phys.*, 7:863–870, 1966. doi: 10.1063/1.1931221. URL <http://link.aip.org/link/?JMP/7/863/1>.
- [119] Ezra Newman and Roger Penrose. An approach to gravitational radiation by a method of spin coefficients. *J. Math. Phys.*, 3(3):566–578, 1962. doi: 10.1063/1.1724257. URL <http://link.aip.org/link/?JMP/3/566/1>.
- [120] Francesco Pannarale, Emanuele Berti, Koutarou Kyutoku, and Masaru Shibata. Nonspinning black hole-neutron star mergers: a model for the amplitude of gravitational waveforms. *Phys. Rev. D*, 88:084011, 2013. doi: 10.1103/PhysRevD.88.084011.
- [121] Larne Pekowsky, Richard O’Shaughnessy, Jim Healy, and Deirdre Shoemaker. Comparing gravitational waves from nonprecessing and precessing black hole binaries in the corotating frame. *Phys. Rev. D*, 88:024040, 2013.
- [122] Roger Penrose. Asymptotic properties of fields and space-times. *Phys. Rev. Lett.*, 10(2): 66–68, 1963.
- [123] Eric Poisson. Gravitational waves from inspiraling compact binaries: The quadrupole-moment term. *Phys. Rev.*, D57:5287–5290, 1998. doi: 10.1103/PhysRevD.57.5287.

- [124] Eric Poisson and Misao Sasaki. Gravitational radiation from a particle in circular orbit around a black hole. v. black-hole absorption and tail corrections. *Phys. Rev. D*, 51:5753–5767, May 1995. doi: 10.1103/PhysRevD.51.5753. URL <https://link.aps.org/doi/10.1103/PhysRevD.51.5753>.
- [125] Denis Pollney and Christian Reisswig. Gravitational memory in binary black hole mergers. *Astrophys. J. Lett.*, 732:L13, 2011. doi: 10.1088/2041-8205/732/1/L13.
- [126] W. H. Press, S. A. Teukolsky, W. T. Vetterling, and B. P. Flannery. *Numerical Recipes: The Art of Scientific Computing (3rd Ed.)*. Cambridge University Press, New York, 2007.
- [127] William H. Press, Saul A. Teukolsky, William T. Vetterling, and Brian P. Flannery. *Numerical Recipes: The Art of Scientific Computing*. Cambridge University Press, third edition, 2007.
- [128] Frans Pretorius. Evolution of binary black hole spacetimes. *Phys. Rev. Lett.*, 95:121101, 2005. doi: 10.1103/PhysRevLett.95.121101.
- [129] M. Pürrer. Frequency domain reduced order models for gravitational waves from aligned-spin compact binaries. *Class. Quantum Grav.*, 31(19):195010, 2014. doi: 10.1088/0264-9381/31/19/195010.
- [130] Michael Pürrer. Frequency-domain reduced order models for gravitational waves from aligned-spin compact binaries. *Class. Quantum Grav.*, 31(19):195010, September 2014. URL <http://stacks.iop.org/0264-9381/31/i=19/a=195010>.
- [131] David Radice, Luciano Rezzolla, and Filippo Galeazzi. Beyond second-order convergence in simulations of binary neutron stars in full general-relativity. *Mon. Not. Roy. Astr. Soc.*, 437: L46–L50, 2014. doi: 10.1093/mnras/slt137.
- [132] David Radice, Albino Perego, Francesco Zappa, and Sebastiano Bernuzzi. Gw170817: Joint constraint on the neutron star equation of state from multimessenger observations. *The Astrophysical Journal Letters*, 852(2):L29, 2018. URL <http://stacks.iop.org/2041-8205/852/i=2/a=L29>.
- [133] J. S. Read, L. Baiotti, J. D. E. Creighton, J. L. Friedman, B. Giacomazzo, K. Kyutoku, C. Markakis, L. Rezzolla, M. Shibata, and K. Taniguchi. Matter effects on binary neutron star waveforms. *Phys. Rev. D*, 88(4):044042, August 2013. doi: 10.1103/PhysRevD.88.044042.
- [134] C. Reisswig, N. T. Bishop, D. Pollney, and B. Szilágyi. Characteristic extraction in numerical relativity: binary black hole merger waveforms at null infinity. *Class. Quantum Grav.*, 27: 075014, 2010. doi: 10.1088/0264-9381/27/7/075014.
- [135] C. Reisswig, N. T. Bishop, and D. Pollney. General relativistic null-cone evolutions with a high-order scheme. *Gen. Rel. Grav.*, 45:1069, 2013.
- [136] Christian Reisswig, Nigel T. Bishop, Chi Wai Lai, Jonathan Thornburg, and Béla Szilágyi. Numerical relativity with characteristic evolution, using six angular patches. *Class. Quantum Grav.*, 24:S327–S340, 2007. doi: 10.1088/0264-9381/24/12/S21.
- [137] M. Ruiz, R. Takahashi, M. Alcubierre, and D. Núñez. Multipole expansions for energy and momenta carried by gravitational waves. *Gen. Relativ. Gravit.*, 40:1705–1729, 2008.

- [138] R. Sachs. Asymptotic symmetries in gravitational theory. *Phys. Rev.*, 128(6):2851–2864, December 1962. URL <http://link.aps.org/doi/10.1103/PhysRev.128.2851>.
- [139] R. K. Sachs. Gravitational waves in general relativity. VIII. waves in asymptotically flat space-time. *Proc. R. Soc. Lond. A*, 270(1340):103–126, October 1962. ISSN 00804630. URL <http://www.jstor.org/stable/2416200>.
- [140] Olivier Sarbach and Manuel Tiglio. Gauge-invariant perturbations of Schwarzschild black holes in horizon-penetrating coordinates. *Phys. Rev. D*, 64:084016, Sep 2001. doi: 10.1103/PhysRevD.64.084016. URL <http://link.aps.org/abstract/PRD/v64/e084016>.
- [141] Mark A. Scheel, Michael Boyle, Tony Chu, Lawrence E. Kidder, Keith D. Matthews, and Harald P. Pfeiffer. High-accuracy waveforms for binary black hole inspiral, merger, and ringdown. *Phys. Rev.*, D79:024003, 2009. doi: 10.1103/PhysRevD.79.024003.
- [142] P. Schmidt, F. Ohme, and M. Hannam. Towards models of gravitational waveforms from generic binaries II: Modelling precession effects with a single effective precession parameter. *Phys. Rev. D*, 91(2):024043, 2015. doi: 10.1103/PhysRevD.91.024043.
- [143] Patricia Schmidt, Mark Hannam, and Sascha Husa. Towards models of gravitational waveforms from generic binaries: A simple approximate mapping between precessing and non-precessing inspiral signals. *Phys. Rev. D*, 86:104063, 2012. doi: 10.1103/PhysRevD.86.104063.
- [144] Jan Steinhoff, Tanja Hinderer, Alessandra Buonanno, and Andrea Taracchini. Dynamical Tides in General Relativity: Effective Action and Effective-One-Body Hamiltonian. *Phys. Rev.*, D94(10):104028, 2016. doi: 10.1103/PhysRevD.94.104028.
- [145] SXS Collaboration. The SXS collaboration catalog of gravitational waveforms. <http://www.black-holes.org/waveforms>.
- [146] B. Szilágyi, R. Gomez, N. T. Bishop, and J. Winicour. Cauchy boundaries in linearized gravitational theory. *Phys. Rev. D*, 62, 2000.
- [147] B. Szilágyi, L. Lindblom, and M. A. Scheel. Simulations of binary black hole mergers using spectral methods. *Phys. Rev. D*, 80(12):124010, December 2009. doi: 10.1103/PhysRevD.80.124010.
- [148] B. Szilágyi, J. Blackman, A. Buonanno, A. Taracchini, H. P. Pfeiffer, M. A. Scheel, T. Chu, L. E. Kidder, and Y. Pan. Approaching the Post-Newtonian Regime with Numerical Relativity: A Compact-Object Binary Simulation Spanning 350 Gravitational-Wave Cycles. *Phys. Rev. Lett.*, 115:031102, 2015. doi: 10.1103/PhysRevLett.115.031102.
- [149] Louis A. Tamburino and Jeffrey H. Winicour. Gravitational fields in finite and conformal Bondi frames. *Phys. Rev.*, 150:1039–1053, 1966. URL <http://link.aps.org/doi/10.1103/PhysRev.150.1039>.
- [150] Andrea Taracchini et al. Effective-one-body model for black-hole binaries with generic mass ratios and spins. *Phys. Rev.*, D89(6):061502, 2014. doi: 10.1103/PhysRevD.89.061502.

- [151] N. W. Taylor, M. Boyle, C. Reisswig, M. A. Scheel, T. Chu, L. E. Kidder, and B. Szilágyi. Comparing gravitational waveform extrapolation to Cauchy-characteristic extraction in binary black hole simulations. *Phys. Rev. D*, 88(12):124010, December 2013. doi: 10.1103/PhysRevD.88.124010.
- [152] Saul A. Teukolsky. *Phys. Rev. D*, 26:745, 1982.
- [153] Leonardo Gualtieri Tiziano Abdelsalhin and Paolo Pani. Post-newtonian spin-tidal couplings for compact binaries. 2018.
- [154] Vijay Varma, Scott Field, Mark A. Scheel, Jonathan Blackman, Lawrence E. Kidder, and Harald P. Pfeiffer. Surrogate model of hybridized numerical relativity binary black hole waveforms.
- [155] J. Vines, É. É. Flanagan, and T. Hinderer. Post-1-Newtonian tidal effects in the gravitational waveform from binary inspirals. *Phys. Rev. D*, 83(8):084051, April 2011. doi: 10.1103/PhysRevD.83.084051.
- [156] Leslie Wade, Jolien D. E. Creighton, Evan Ochsner, Benjamin D. Lackey, Benjamin F. Farr, et al. Systematic and statistical errors in a bayesian approach to the estimation of the neutron-star equation of state using advanced gravitational wave detectors. *Phys. Rev. D*, 89:103012, 2014. doi: 10.1103/PhysRevD.89.103012.
- [157] Clifford M. Will and Alan G. Wiseman. Gravitational radiation from compact binary systems: Gravitational wave forms and energy loss to second postNewtonian order. *Phys. Rev.*, D54:4813–4848, 1996. doi: 10.1103/PhysRevD.54.4813.
- [158] Kent Yagi. Multipole love relations. *Phys. Rev. D*, 89:043011, Feb 2014. doi: 10.1103/PhysRevD.89.043011. URL <https://link.aps.org/doi/10.1103/PhysRevD.89.043011>. Errata: [159],[160].
- [159] Kent Yagi. Erratum: Multipole love relations [phys. rev. d 89, 043011 (2014)]. *Phys. Rev. D*, 96:129904, Dec 2017. doi: 10.1103/PhysRevD.96.129904. URL <https://link.aps.org/doi/10.1103/PhysRevD.96.129904>.
- [160] Kent Yagi. Erratum: Multipole love relations [phys. rev. d 89, 043011 (2014)]. *Phys. Rev. D*, 97:129901, Jun 2018. doi: 10.1103/PhysRevD.97.129901. URL <https://link.aps.org/doi/10.1103/PhysRevD.97.129901>.
- [161] Kent Yagi and Nicolas Yunes. I-Love-Q. *Science*, 341:365–368, 2013. doi: 10.1126/science.1236462.
- [162] Kent Yagi and Nicolás Yunes. I-love-q relations in neutron stars and their applications to astrophysics, gravitational waves, and fundamental physics. *Phys. Rev. D*, 88:023009, Jul 2013. doi: 10.1103/PhysRevD.88.023009. URL <https://link.aps.org/doi/10.1103/PhysRevD.88.023009>.
- [163] Kent Yagi and Nicolas Yunes. Love number can be hard to measure. *Phys. Rev. D*, 89:021303, 2014. doi: 10.1103/PhysRevD.89.021303.